Università degli Studi di Ferrara

Facoltà di Scienze Matematiche, Fisiche e Naturali

Dottorato di Ricerca in Fisica

Study of double charmonium production around $\sqrt{s} = 10.58$ GeV with the BaBar detector

Dr. Annalisa Cecchi

Advisor:

Prof. Diego Bettoni

Coordinator:

Prof. Filippo Frontera

Referees:

Prof. Antimo Palano

Prof. Dr. Klaus Peters

2006-2008

Contents

Introduction

The goal of high energy physics is to identify the elementary constituents of matter and to understand their fundamental interactions. Over the last twenty years, this endeavor has been extraordinarily successful. A gauge theory called *Standard Model* provides a satisfactory description of the strong, weak, and electromagnetic interactions of all the known elementary particles. There are very few discrepancies between theory and experiment, and most of them are at the level of a few standard deviations or less. However there are processes for which experimental results have differed from theoretical predictions by orders of magnitude: soe of these studies are related to the production of charmonium. This dramatic conflict between experiment and theory presents a unique opportunity to make a significant step forward in our understanding of heavy quarkonium physics.

Quarkonia play an important role in several high energy experiments. The diversity, quantity and accuracy of the data still under analysis and currently being collected in many high energy experiments around the world is impressive.

These data come from experiments of quarkonium formation (BES at the Beijing Electron Positron Collider, E835 at Fermilab, and CLEO at the Cornell Electron Storage Ring), clean samples of charmonia produced in B-decays, in photon-photon fusion and in initial state radiation, at the B-meson factories (BaBar at PEP-II and Belle at KEKB), including the unexpected observation of large amounts of associated $(c\bar{c})(c\bar{c})$ production and the observation of new and possibly exotics quarkonia states. The CDF and D0 experiments at Fermilab measuring heavy quarkonia prodution from gluon-gluon fusion in $p\bar{p}$ annihilations at 2 TeV; ZEUS and H1, at DESY, studying charmonia production in photon-gluon fusion; PHENIX and STAR, at RHIC, and NA60, at CERN, studying charmonia production, and suppression, in heavy-ion collisions [7].

This has led to the discovery of new states, new production mechanisms, new decays and transitions, and in general to the collection of high statistics and precision data sample. In the near future, even larger data samples are

expected from the BES-III upgraded experiment, while the B factories and the Fermilab Tevatron will continue to supply valuable data for few years. Later on, new experiments at new facilities will become operational (the LHC experiments at CERN, PANDA at GSI, hopefully a Super-B factory, a Linear Collider, etc.) offering fantastic challenges and opportunities in this field.

In this thesis the analysis on double charmonium production at the energy of the $\Upsilon(4S)$, with the *BABAR* data is documented. The aim of this analysis is to understand the mechanism of production of double charmonium states fro e^+e^- annihilation, in particular after the discrepancies which at the beginning of these studies appeared.

With successive studies, these discrepancies have been almost solved. This analysis was already performed by *BABAR* collaboration [28], and in this thesis we want to update that work, with a luminosity early four times higher ($468\ fb^{-1}$. In the mean time, also Belle collaboration published on this analysis [16], obtaining results compatible with *BABAR* and finding out a new charmonium state, named X(3940). We aim here also to confirm this state.

This thesis is composed by five chapters. Chapter I is an introduction to charmonium spectroscopy, with a description of the NRQCD, which the theorethical framework of this analysi, then the potential models that have been developed to describe the mass spectrum.

The theories related to the double charmonium production mechanisms are presented in Chapter II: in particular the calculation of the cross section and the dicrepancies between theory and experiment.

Then in Chapter III the *BABAR* detector is described.

In Chapter IV there is a description on how has been performed the analysis: the analysis strategy, selection and cut optimization, and validation of the fit are documented, before the unblind of the interested region.

In chapter V we give the final results, after unblind.

Chapter 1

Charmonium physics

Until 1974 all the known hadrons were composed by three quark flavours: the *up* (u), *down* (d) and *strange* (s). The masses of these states were rather small: a few MeV for u and d, and 100-200 MeV for s.

In November of 1974, a remarkably massive and narrow resonance, named "J", was discovered [1] with a mass of 3.1 GeV/c^2, decaying to e^+e^-, in the reaction $p + Be \rightarrow e^+e^- + X$. Simultaneously, the resonance was discovered [2] in the direct channel $e^+e^- \rightarrow hadrons$ (also to $e^+e^-, \mu^+\mu^-$), and was named the "ψ". The dual name J/ψ has afterwards persisted.

With the discovery of the J/ψ, the existence of a new quark flavour called *charm* (c), with a mass of the order of 1 GeV, as well as the existence of a family of states called *charmonia* was demonstrated.

The J/ψ is a member of this family, that is composed by the bound states of charm quark and antiquark ($c\bar{c}$). The charmonium is the most widely studied heavy quarkonium system, and the goal of this chapter is to give the theoretical tools necessary to face the quarkonium, and in particular charmonium, physics.

1.1 Potential models

When two particles form a bound state, the attractive potential can be studied measuring the energy spectrum of the system. In atomic physics, the binding energy of the electron-nucleus system depends on the orbital angular momentum (L), spin (S) and total angular momentum ($J = L + S$) state (neglecting the nucleus angular momentum I). To classify the energy levels of the system the spectroscopic notation $n^{2S+1}L_J$ is used. A similar pattern of energy levels is present in positronium (the e^+e^- bound state); this has been used to study the potential between the electron and the positron.

1.1 Potential models

The same concept can be applied also to the mesons, which are the quark-antiquark ($q\bar{q}$) bound states. Also in this case the spectroscopic notation $n^{2S+1}L_J$ for the classication of the mesons is used.

The intrinsic parity P and charge conjugation C of a charmonium state are related to the angular momentum by the relations:

$$P = (-1)^{L+1}, \qquad C = (-1)^{L+S}.$$

Also the J^{PC} notation can be used to classify the $c\bar{c}$ states.

Quantum Chromodynamics (QCD) is the modern theory of the strong interactions. The non perturbative features of QCD prevent the possibility of describing it on the basis of the fundamental theory of the interaction. For this reason the natural approach to charmonium spectroscopy is to build an effective potential model describing the observed mass spectrum. This approximation allows to integrate out many fundamental effects like gluon emission or light quark pairs and to deal with an effective potential which is the result of the $q\bar{q}$ direct interaction as well as the energy of the gluon field. This potential should nevertheless reproduce the two main features of the bound quark states in the two limits of small and large distance: asymptotic freedom and confinement.

The $c\bar{c}$ system can be described with a Schroedinger equation:

$$H\Psi(x) = E\Psi(x), \tag{1.1}$$

where the hamiltonian for the $c\bar{c}$ system can be written as:

$$H = H_0 + H'. \tag{1.2}$$

H_0 can be expressed as a free particle hamiltonian plus a non-relativistic potential $V(r)$:

$$H_0 = 2m_c + \frac{p^2}{m_c} + V(r), \tag{1.3}$$

where m_c is the charm quark mass and p its momentum.

$V(r)$ can be built taking into account the properties of strong interaction in the limit of small and large distances. At small distance the potential between the quarks for a quark-antiquark pair bound in a color singlet, is coulomb-like:

$$V(r) \sim \frac{4}{3}\frac{\alpha_s(r)}{r},$$

where r is the distance between the quarks, α_s is the strong coupling constant and the factor $4/3$ comes from the group theory of SU(3), related to the colour.
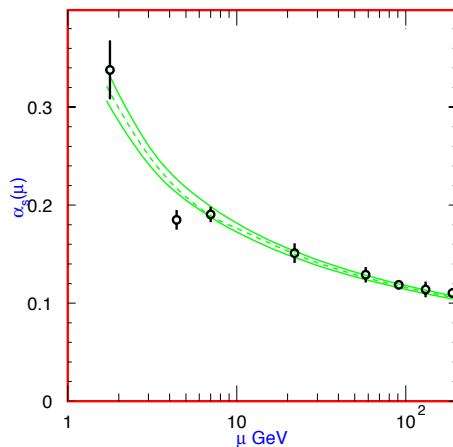
Figure 1.1: *Summary of the values of α_s at the values of μ where they are measured [5].*

The value of the running coupling constant α_s depends on the energy scale of the interaction in the way shown in Fig. 1.1, where is clear the decrease of α_s with increasing μ. At the leading order in the inverse power of $ln(\mu^2/\Lambda^2)$, α_s is described by:

$$\alpha_s(\mu) = \frac{4\pi}{\beta_0 ln(\mu^2/\Lambda^2)}, \qquad (1.4)$$
$$\beta_0 = 11 - \frac{2}{3}n_f$$

where $\Lambda \simeq 0.2 \; GeV$ is the non-perturbative scale of QCD (the energy where (1.4) diverges) and n_f is the number of quarks lighter than the energy scale . It is clear from equation 1.4 that, as the energy scale of a strong process decreases and becomes closer to Λ, α_s increases and the QCD can not be treated as a perturbative theory.

As a result of (1.4) the coupling $\alpha_s(\mu)$ varies logarithmically with μ, so that at very short distances, gluon exchange becomes weaker. This property, known as *asymptotic freedom*, is responsible for the quasi-free behavior exhibited by quarks in hadrons probed at very short distances by deeply inelastic scattering.

At large distance, that means at momentum scales smaller than $\Lambda \simeq 200 MeV$ the *confinement* term is dominating. It can be written in the form:

$$V(r) \sim kr,$$

where $k \simeq 1 \, GeV/fm$ is called string constant. The absence of free quarks
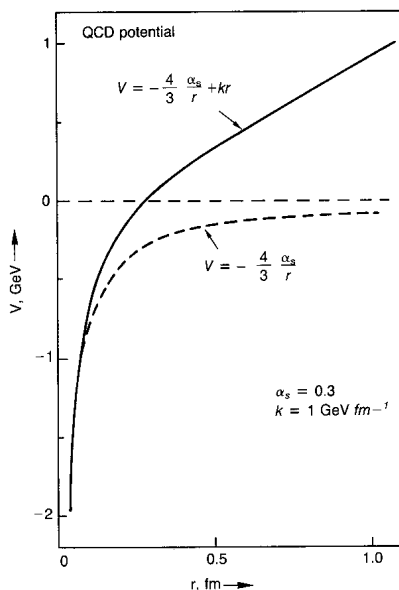
Figure 1.2: *Plot of the QCD potential (1.1), for quark-gluon coupling $\alpha_s = 0.20$ and $k = 1\ Gev/fm$*

in nature is explained exactly by the confinement term, because it implies that the energy of a $q\bar{q}$ system increases with the distance.

By putting together these two behaviors, one can write the Cornell potential, shown in Fig. 1.2 [3]:

$$V(r) \sim -\frac{4}{3}\frac{\alpha_s(r)}{r} + kr, \tag{1.5}$$

With this potential, the charmonium wave function can be expressed as:

$$\Psi(r, \theta, \phi) = R_{nl}(r)Y_l^m(\theta, \phi). \tag{1.6}$$

This description, however, is not enough to reproduce the mass difference for charmonium states in the same orbital angular momentum or spin multiplets.

H' in the equation (1.2) includes the spin (S) and orbital (L) dependent part of the strong interaction, explaining the charmonium fine and hyperfine structure [4]:

$$H' = V_{LS} + V_{SS} + V_{tens}. \tag{1.7}$$

The various terms of interaction are described in the following:

10

- **spin-orbit ($\mathbf{V_{LS}}$):** spin-orbit forces between quarks are present for both vector and scalar interactions, but in different form. We find for quarks of equal mass m_c:

$$V_{LS} = (\mathbf{L} \cdot \mathbf{S})(3\frac{dV_V}{dr} - \frac{dV_S}{dr})/(2m_c^2 r) \qquad (1.8)$$

where V_S and V_V are the scalar and vector components of the non-relativistic potential V(r). This term splits the states with the same orbital angular momentum depending on the $(\mathbf{L} \cdot \mathbf{S})$ expectation value (fine structure);

- **spin-spin ($\mathbf{V_{SS}}$):** the hyperfine electromagnetic interaction between a proton and an electron leads to a 1420 MHz level splitting between singlet and triplet states of atomic hydrogen. In light-quark systems, a similar spin-spin force due to single-gluon-exchange between quarks generates the splittings between the masses of the pion and the ρ resonance, the nucleon and the Δ resonance, the Σ and the Λ hyperons, and so on. The spin-spin interaction is of the form:

$$V_{SS} = \frac{2(\mathbf{S_1} \cdot \mathbf{S_2})}{3m_c^2}\nabla^2 V_V(r) \qquad (1.9)$$

and the expectation value for $\mathbf{S_1} \cdot \mathbf{S_2}$ is +1/4 for $S = 1$ and -3/4 for $S = 0$;

- **tensor ($\mathbf{V_T}$):** the tensor potential, in analogy with electrodynamics, contains the tensor effects of the vector potential:

$$V_T = \frac{S_{12}}{12m_c^2}(\frac{1}{3}\frac{dV_V}{dr} - \frac{d^2 V_V}{dr^2}),$$

$$S_{12} = 2 \; [3(\mathbf{S} \cdot \hat{\mathbf{r}})(\mathbf{S} \cdot \hat{\mathbf{r}}) - S^2].$$

where S_{12} has nonzero matrix elements only for $L \neq 0$.

Even if the QCD theory allows to describe on the basis the foundamental theory of the interactions, as explained in the next section, other suggestions for the functional form of the binding potential V(r) exist, but they are essentially coincident with the values from (1.1) in the region from 0.1 to 1.0 fm, the dimension scale of the $c\bar{c}$ system, and lead to similar results.

Another possibility to predict the charmonium mass spectrum is to compute it with the lattice QCD (LQCD) [6], which is essentially QCD applied

on a discrete Euclidean space-time grid. Indeed, QCD has been very successful in predicting phenomena involving large momentum transfer. In this regime the coupling constant is small and perturbation theory becomes a reliable tool.

On the other hand, at the scale of the hadronic world, $\mu \leq 1 GeV$, the coupling constant is of order unity and perturbative methods fail. In this domain lattice QCD provides a non-perturbative tool for calculating the hadronic spectrum and the matrix elements of any operator within these hadronic states from first principles. Since no new parameters or field variables are introduced in this discretization, LQCD retains the fundamental character of QCD.

The field theory fundamental principles and the path integral can be used to calculate on a computer the properties of the strong interaction, with Monte Carlo integration of the Euclidean path integral. The value of the lattice spacing, usually denoted with a, can be decided depending on the specific problem that has to be solved.

The only tunable input parameters in these simulations are the strong coupling constant and the bare masses of the quarks. Our belief is that these parameters are prescribed by some yet more fundamental underlying theory, however, within the context of the standard model they have to be fixed in terms of an equal number of experimental quantities.

1.2   Quantum Chromodynamics

Quantum Chromodynamics is a quantum field theory obtained from the full Standard Model (SM) by setting the weak and electromagnetic coupling constants to zero and freezing the scalar doublet to its vacuum expectation value. What remains is a Yang-Mills (YM) theory with local gauge group SU(3) (colour) vectorially coupled to six Dirac fields (quarks) of different masses (flavours). The vector fields in the YM Lagrangian (gluons) live in the adjoint representation and transform like connections under the local gauge group whereas the quark fields live in the fundamental representation and transform covariantly. The QCD Lagrangian is

$$\mathcal{L}_{QCD} = -\frac{1}{4} F^a_{\mu\nu} F^{a\ \mu\nu} + \sum_{\{q\}} \bar{q}(i\gamma^\mu D_\mu - m_q)q \tag{1.10}$$

where

$$\{q\} = u, d, s, c, b, t,$$
$$F_{\mu\nu}^a = \partial_\mu A_\nu^a - \partial_\nu A_\mu^a + g f^{abc} A_\mu^b A_\nu^c,$$
$$D_\mu = \partial_\mu - i T^a A_\mu^a$$

and f_{abc} are the SU(3) structure constants and T^a form a basis of the fundamental representation of the SU(3) algebra. When coupled to electromagnetism, gluons behave as neutral particles whereas u, c and t quarks have charges +2/3 and d, s and b quarks have charges -1/3.

The main properties of QCD, which have been partially illustrated in the previous sections, are the following:

- It is Poincaré, parity, time reversal and hence charge conjugation invariant. It is in addition invariant under $U(1)^6$ which implies individual flavour conservation.

- Being a non-Abelian gauge theory, the physical spectrum consists of colour singlet states only. The simplest of these states have the quantum numbers of quark-antiquark pairs (mesons) or of three quarks (baryons) although other possibilities are not excluded.

- The QCD effective coupling constant $\alpha_s(q)$ decreases as the momentum transfer scale q increases (asymptotic freedom) [8, 9], as also already explained in section 1.1. This allows to make perturbative calculations in α_s at high energies.

- At low energies it develops an intrinsic scale (mass gap), usually referred as Λ_{QCD}, which provides the main contribution to the masses of most light hadrons. At scales $q \sim \Lambda_{QCD}, \alpha_s(q) \sim 1$ and perturbation theory cannot be used. Investigations must be carried out using non-perturbative techniques, the best established of which is lattice QCD.

  Quarks are conventionally divided into light $m_q l^+ l^- \Lambda_{QCD}$ ($q = u, d, s$) and heavy $m_Q \gg \Lambda_{QCD}$ ($Q = c, b, t$):[1]

  $$m_u = 1.5 - 3.3 \ MeV, m_u = 3.5 - 6.0 \ MeV, m_s = 70 - 130 \ MeV,$$
  $$m_c = 1.27^{+0.07}_{-0.11} \ MeV, \ m_b = 4.20^{+0.17}_{-0.07} \ GeV, \ m_t = 171.2 \pm 2.1 \ GeV$$

- If light quark masses are neglected, the $U(1)^3$ flavour conservation symmetry of the QCD Lagrangian in this sector is enlarged to a $U(3)\bigotimes U(3)$

---

[1]All these values are taken from [5].

13

group. The axial U(1) subgroup is explicitly broken by quantum effects (axial anomaly). The vector U(1) subgroup provides light flavour conservation. The remaining SU(3)$\otimes$SU(3) subgroup, known as chiral symmetry group, turns out to be spontaneously broken down to the diagonal SU(3) (flavour symmetry). This produces eight Goldstone bosons, which, upon taking into account the explicit breaking of the symmetry due to the non-zero quark masses, acquire masses that are much smaller than Λ_{QCD}.

- Hadrons containing heavy quarks have masses of the order of m_Q rather than of the order Λ_{QCD}. They enjoy particular kinematical features that allow for specific theoretical treatments.

1.3 Effective Field Theories

From the point of view of QCD the description of hadrons containing two heavy quarks is a rather challenging problem, which adds to the complications of the bound state in field theory those coming from a nonperturbative low-energy dynamics. A proper relativistic treatment of the bound state based on the Bethe-Salpeter equation [10] has proved difficult. Perturbative calculations have turned out unpractical at higher order and the method has been abandoned in recent QCD calculations. Moreover, the entanglement of all energy modes in a fully relativistic treatment is more an obstacle than an advantage for the factorization of physical quantities into high-energy perturbative and low energy nonperturbative contributions. Partial semirelativistic reductions and models have been often adopted to overcome these difficulties at the price to introduce uncontrolled approximations and lose contact with QCD. The fully relativistic dynamics can, in principle, be treated without approximations in lattice gauge theories. This is in perspective the best founded and most promising approach, as already said in section 1.1.

A nonrelativistic treatment of the heavy quarkonium dynamics, which is suggested by the large mass of the heavy quarks, has clear advantages. The velocity of the quarks in the bound state provides a small parameter in which the dynamical scales may be hierarchically ordered and the QCD amplitudes systematically expanded. Factorization formulas become easier to achieve. A priori we do not know if a nonrelativistic description will work well enough for all heavy quarkonium systems in nature: for instance, the charm quark may not be heavy enough. The fact that most of the theoretical predictions are based on such a nonrelativistic assumption and the success of most of them may be seen as a support to the assumption.

14

We may, however, also take advantage of the existence of a hierarchy of scales by substituting QCD with simpler but equivalent *Effective Field Theories* (EFTs). EFTs have become increasingly popular in particle physics during the last decades.

They provide a realization of Wilson renormalization group ideas [11] and fully exploit the properties of local quantum field theories. An EFT is a quantum field theory with the following properties:

a) it contains the relevant degrees of freedom to describe phenomena that occur in certain limited range of energies and momenta;

b) it contains an intrinsic energy scale Λ that sets the limit of applicability of the EFT.

The Lagrangian of an EFT is organized in operators of increasing dimension, hence, an EFT is in general non-renormalizable in the usual sense. In spite of this, it can be made finite to any finite order in $1/\Lambda$ by renormalizing (matching) the constants (matching coefficients) in front of the operators in the Lagrangian until that order. This means that one needs more renormalization conditions when the order in $1/\Lambda$ is increased. However, even if the only way of fixing the constants would be by means of experimental data, this would reduce but not spoil the predictive power of the EFT. If the data are abundant, the constants can be fit once for ever and used later on to make predictions on new experiments.

The prototype of EFT for heavy quarks is the *Heavy Quark Effective Theory* (HQET), which is the EFT of QCD suitable to describe systems with only one heavy quark [12, 13]. These systems are characterized by two energy scales: m and Λ_{QCD}. HQET is obtained by integrating out the scale m and built as a systematic expansion in powers of Λ_{QCD}/m.

As discussed above, bound states made of two heavy quarks are characterized by more scales. Integrating out only the scale m, which for heavy quarks can be done perturbatively, leads to an EFT, *Nonrelativistic QCD* (NRQCD) [14, 15], that still contains the lower scales as dynamical degrees of freedom. Disentangling the remaining scales is relevant both technically, since it enables perturbative calculations otherwise quite complicate, and more fundamentally, since it allows to factorize nonperturbative contributions into the expectation values or matrix elements of few operators. These may be eventually evaluated on the lattice, extracted from the data or calculated in QCD vacuum models.

In the next section we will give a brief general introduction to NRQCD, since this is the framework for the analysis presented in this thesis.

1.4   Nonrelativistic QCD

A particularly elegant approach for separating relativistic from nonrelativistic scales is to recast the analysis in terms of nonrelativistic quantum chromodynamics (NRQCD) [15], an effective field theory designed precisely to separate the relativistic physics of annihilation (which involves momenta $p \sim M$) from the nonrelativistic physics of quarkonium structure (which involves $p \sim Mv$).

NRQCD consists of a nonrelativistic Schroedinger field theory for the heavy quark and antiquark that is coupled to the usual relativistic field theory for light quarks and gluons. The theory is made precisely equivalent to full QCD through the addition of local interactions that systematically incorporate relativistic corrections through any given order in the heavy-quark velocity v. It is an effective field theory, with a finite ultraviolet cutoff of order M that excludes relativistic states (states that are poorly described by nonrelativistic dynamics). A heavy quark in the meson can fluctuate into a relativistic state, but these fluctuations are necessarily short-lived. This means that the effects of the excluded relativistic states can be mimicked by local interactions and can, therefore, be incorporated into NRQCD through renormalizations of its infinitely many coupling constants. Thus, nonrelativistic physics is correctly described by the nonperturbative dynamics of NRQCD, while all relativistic effects are absorbed into coupling constants that can be computed as perturbation series in $\alpha_s(\mathrm{M})$.

The main advantage offered by NRQCD over ordinary QCD in this context is that it is easier to separate contributions of different orders in v in NRQCD. Thus, we are able not only to organize calculations to all orders in α_s, but also to elaborate systematically the relativistic corrections to the conventional formulas.

1.4.1   The NRQCD lagrangian

The most important energy scales for the structure and spectrum of a heavy quarkonium system are Mv and Mv^2, where M is the mass of the heavy quark Q and vl^+l^-1 is its average velocity in the meson rest frame. Momenta of order M play only a minor role in the complex binding dynamics of the system. We can take advantage of this fact in our analysis of heavyquark mesons by modifying QCD in two steps.

We start with full QCD, in which the heavy quarks are described by 4-component Dirac spinor fields. In the first step, we introduce an ultraviolet momentum cutoff that is of order M. This cutoff explicitly excludes relativistic heavy quarks from the theory, as well as gluons and light quarks with momenta of order M. It is appropriate to an analysis of heavy quarkonium,

16

since the important nonperturbative physics involves momenta of order Mv or less. Of course, the relativistic states we are discarding do have some effect on the low energy physics of the theory. However, any interaction involving relativistic intermediate states is approximately local, since the intermediate states are necessarily highly virtual and so cannot propagate over long distances. Thus, generalizing standard renormalization procedures, we systematically compensate for the removal of relativistic states by adding new local interactions to the lagrangian. To leading order in $1/\Lambda$ or, equivalently, $1/M$, these new interactions are identical in form to interactions already present in the theory, and so the net effect is simply to shift bare masses and charges. Beyond leading order in $1/M$, one must extend the lagrangian to include nonrenormalizable interactions that correct the low energy dynamics order-by-order in $1/M$. In this cutoff formulation of QCD, all effects that arise from relativistic states, and only these effects, are incorporated into renormalizations of the coupling constants of the extended lagrangian. Thus, in the cutoff theory, relativistic and nonrelativistic contributions are automatically separated. This separation is the basis for an analysis of the annihilation decays of heavy quarkonia.

The lagrangian for NRQCD is:

$$\mathcal{L}_{NRQCD} = \mathcal{L}_{light} + \mathcal{L}_{heavy} + \delta\mathcal{L} \qquad (1.11)$$

The gluons and the n_f flavors of light quarks are described by the fully relativistic lagrangian

$$\mathcal{L}_{light} = -\frac{1}{2}tr G_{\mu\nu}G^{\mu\nu} + \sum \bar{q}i\slashed{D}q \qquad (1.12)$$

where G_μ is the gluon field-strength tensor expressed in the form of an SU(3) matrix, and q is the Dirac spinor field for a light quark. The gauge-covariant derivative is $D^\mu + igA^\mu$, where $A^\mu = (\phi, \mathbf{A})$ is the SU(3) matrix-valued gauge field and g is the QCD coupling constant. The sum in (1.12) is over the n_f flavors of light quarks.

The heavy quarks and antiquarks are described by the term

$$\mathcal{L}_{heavy} = \psi^\dagger\left(iD_t + \frac{\mathbf{D}^2}{2M}\right)\psi + \chi^\dagger\left(iD_t - \frac{\mathbf{D}^2}{2M}\right)\chi, \qquad (1.13)$$

where ψ is the Pauli spinor field that annihilates a heavy quark, χ is the Pauli spinor field that creates a heavy antiquark, and D_t and $\mathbf{D}$ are the time and space components of the gauge-covariant derivative D^μ. Color and spin indices on the fields ψ and χ have been suppressed. The lagrangian

$\mathcal{L}_{light} + \mathcal{L}_{heavy}$ describes ordinary QCD coupled to a Schroedinger field theory for the heavy quarks and antiquarks.

The relativistic effects of full QCD are reproduced through the correction term $\delta\mathcal{L}$ in the lagrangian $\mathcal{L}_{NRQCD}$ [14].

In particular the correction terms most important for heavy quarkonium are bilinear in the quark field or antiquark field:

$$
\begin{aligned}
\mathcal{L}_{bilinear} = {} & \frac{c_1}{8M^3} \left(\psi^\dagger (\mathbf{D}^2)^2 \psi - \chi^\dagger (\mathbf{D}^2)^2 \chi \right) \\
& + \frac{c_2}{8M^2} \left(\psi^\dagger (\mathbf{D} \cdot g\mathbf{E} - g\mathbf{E} \cdot \mathbf{D})\psi - \chi^\dagger (\mathbf{D} \cdot g\mathbf{E} - g\mathbf{E} \cdot \mathbf{D})\chi \right) \\
& + \frac{c_3}{8M^2} \left(\psi^\dagger (i\mathbf{D} \times g\mathbf{E} - g\mathbf{E} \times i\mathbf{D})\psi - \chi^\dagger (i\mathbf{D} \times g\mathbf{E} - g\mathbf{E} \times i\mathbf{D})\chi \right) \\
& + \frac{c_4}{2M} \left(\psi^\dagger (g\mathbf{B} \cdot \sigma)\psi - \chi^\dagger (g\mathbf{B} \cdot \sigma)\chi \right),
\end{aligned}
\tag{1.14}
$$

where $E^i = G^{0i}$ and $B_i = \frac{1}{2}\epsilon^{ijk}G^{jk}$ are the electric and magnetic components of the gluon field strength tensor $G^{\mu\nu}$. By charge conjugation symmetry, for every term in (1.14) involving ψ, there is a corresponding term involving the antiquark field χ, with the same coefficient c_i, up to a sign. The operators in (1.14) must be regularized, and they therefore depend on the ultraviolet cutoff or renormalization scale Λ of NRQCD. The coefficients $c_i(\Lambda)$ also depend on Λ in such a way as to cancel the Λ-dependence of the operators.

Notice that $\mathcal{L}_{bilinear}$ doesn't contain mixed two-fermion operators involving $\chi^\dagger$ and ψ (or $\psi^\dagger$ and χ), corresponding to the annihilation (or the creation) of a $Q\bar{Q}$ pair. Indeed such terms are excluded from the lagrangian as part of the definition of NRQCD: if such an operator annihilates a $Q\bar{Q}$ pair, it would, by energy conservation, have to create gluons (or light quarks) with energies of order M. The amplitude for annihilation of a $Q\bar{Q}$ pair into such high energy gluons cannot be described accurately in a nonrelativistic theory such as NRQCD.

The coefficients c_i must be tuned as functions of the coupling constant α_s, the heavy-quark mass parameter in full QCD, and the ultraviolet cutoff Λ of NRQCD, so that physical observables are the same as in full QCD.

In principle, infinitely many terms are required in the NRQCD lagrangian in order to reproduce full QCD, but in practice only a finite number of these is needed for precision to any given order in the typical heavy-quark velocity v.

1.5 Experimental study of charmonium

1.5.1 Quarkonium production

Quarkonia can be produced in several ways, which reach different states within the spectrum. The first three listed here are mere reversals of $Q\bar{Q}$ decay processes and are sketched in Fig. 1.3 a), b), and c).

In electron-positron colliders, the reaction results in $e^+e^- \to \gamma^* \to Q\bar{Q}$ states that can couple to a virtual photon, namely n^3S_1 such as J/ψ and Υ with a tiny admixture of n^3D_1. Direct resonance formation offers the advantage of large production rates, giving access to branching fractions even as small as 10^{-5}, as well as higher accuracy in the measurements of masses and widths..

Two-photon collisions allow direct creation of $J = 0, 2$ states, e.g. $\eta_{[c,b]}$, $\chi_{[c,b][0,2]}$. While they are readily available at e^+e^- machines, they suffer from small production rates. Still they provide an important contribution in that they can be used for discovery purposes.

Hadron machines, being able to form any quarkonia state in principle by annihilation of the $p\bar{p}$ pair into gluons, continue to contribute mostly to the study of production of charmonia. This environment suffers from large background; thereby one has to focus on exclusive decays.

Two more scenarios: downward transitions within the system provide an important route to otherwise not reachable states. Any B-factory has access to $c\bar{c}$ states through weak decays of the b quark, with the two processes sketched in Fig. 1.3 d) and e).

An important background for the reaction $e^+e^- \to Q\bar{Q} \to X$, or more explicitly, $e^+e^- \to \gamma^* \to Q\bar{Q} \to X$, is the case in which no intermediate $Q\bar{Q}$ resonance is formed. The presence of this channel adds to the measured cross-section both directly and by interference, which can be a sizeable contribution. In most measurements, this contribution is not taken into account or subtracted. This background needs to be either measured, by running off the relevant resonance, or calculated. In measurements of the cross-section as function of energy (scans), the non-resonant production can be explicitly taken into account when fitting the line shape.

In addition to that, the production of double charmonium in e^+e^- annihilations has recently been observed at the B factories. The production of double charmonium in e^+e^- annihilation was discovered by the Belle collaboration from data collected at the $\Upsilon(4S)$ resonance at a center-of-mass energy $s = \sqrt{}(10.6)GeV$ by studying the recoil momentum spectrum of the J/ψ in $e^+e^- \to J/\psi + X$ [16]. The measured cross section for double charmonium production was about one order of magnitude larger than the theoretical

prediction of NRQCD in the non-relativistic limit. This large discrepancy was rather puzzling. This way to produce charmonium is the main topic of this thesis, and the next chapter will be dedicated to the double charmonium production physics.

1.5.2 Charmonium spectrum

The spectrum of charmonium states is shown in Fig. 1.4. The potential model, described in section 1.1, can explain with the spin-spin interaction term (V_{SS}) the splitting among spin singlet and triplet states like J/ψ and η_c, and with the spin-orbit interaction (V_{LS}) the splitting among states like $\chi_{c\ 0,1,2}$.

The charmonium spectrum consists of eight narrow states below the open charm threshold (3.73 GeV) and several tens of states above the threshold.

All eight states **below D$\bar{\text{D}}$ threshold** are well established, but whereas the triplet states are measured with very good accuracy, the same cannot be said for the singlet states.

The η_c was discovered almost thirty years ago and many measurements of its mass and total width exist. Despite the large variety of available data on it, the precise determination of its mass and width is still an open problem. The Particle Data Group (PDG) [5] value of the mass is $2980.3 \pm 1.2 \,\mathrm{MeV}/c^2$: the error on the η_c mass is still as large as $1.2 \,\mathrm{MeV}/c^2$, to be compared with few tens of KeV/c^2 for the J/ψ and ψ' and few hundreds of KeV/c^2 for the $\chi_{c\ 0,1,2}$. The situation is even worse for the total width: the PDG average
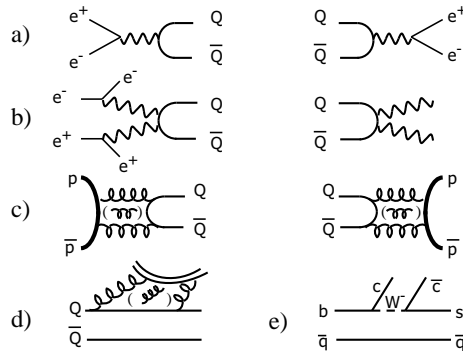
Figure 1.3: *Heavy quarkonia production diagrams. Production (left) and their corresponding decay (right) processes: a) $e^+e^- \to \gamma^* \to Q\bar{Q}$; b) $\gamma\gamma \to Q\bar{Q}$; c) $p\bar{p} \to$ gluons $\to Q\bar{Q}$; d) Quarkonium de-excitation by emission of two pions; e) creating charmonium from a B meson.*
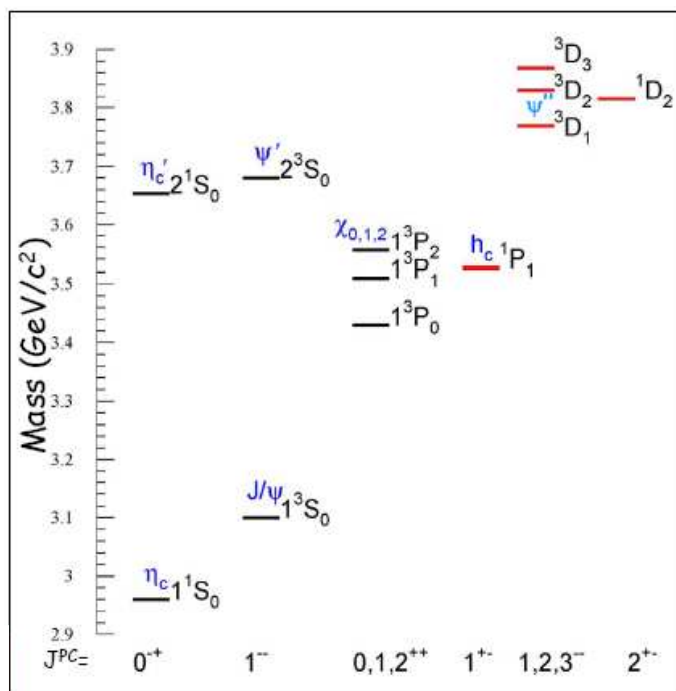
Figure 1.4: *The charmonium spectrum.*

is 26.7 ± 3.0 MeV. The most recent measurements have shown that the η_c width is larger than was previously believed, with values which are difficult to accomodate in quark models. This situation points to the need for new high-precision measurements of the η_c parameters.

The first experimental evidence of the $\eta_c(2S)$ was reported by the Crystal Ball Collaboration [17], but this finding was not confirmed in subsequent searches in $p\bar{p}$ or e^+e^- experiments. The η_c (2S) was finally discovered by the Belle collaboration [18] in the hadronic decay of the B meson $B \rightarrow K + \eta_c(2s) \rightarrow K + (K_s K^- \pi^+)$ with a mass which was incompatible with the Crystal Ball candidate. The Belle finding was then confirmed by CLEO and BaBar [19, 20], which observed this state in twophoton fusion. The PDG value of the mass is 3637 ± 4 MeV$/c^2$, and the width is only measured with an accuracy of 50%: 14 ± 7 MeV$/ c^2$.

The $^1P_1$ state of charmonium (h_c) is of particular importance in the determination of the spin-dependent component of the $q\bar{q}$ confinement potential. The h_c has been observed by CLEO [21] in the reaction $\psi(2S) \rightarrow \pi^0 h_c \rightarrow (\gamma\gamma)(\gamma\eta_c)$ with a mass of $3524.4 \pm 0.6 \pm 0.4$ MeV$/c^2$ at a significance greater

than 5σ.

Particle	$n^{2S+1}L_J$	J^{PC}	Mass (MeV)	Width (MeV)
η_c	1^1S_0	0^{-+}	2980.3 ± 1.2	26.7 ± 3.0
J/ψ	1^3S_1	1^{--}	3096.916 ± 0.011	$(93.2 \pm 2.1) \times 10^{-3}$
χ_{c0}	1^3P_0	0^{++}	3414.75 ± 0.31	10.2 ± 0.7
χ_{c1}	1^3P_1	1^{++}	3510.66 ± 0.07	0.89 ± 0.05
χ_{c2}	1^1P_2	2^{++}	3556.20 ± 0.09	2.03 ± 0.12
$\eta_c(2S)$	2^1S_0	0^{-+}	3637 ± 4	14 ± 7
$\psi(2S)$	2^3S_1	1^{--}	3686.09 ± 0.04	0.317 ± 0.009

Table 1.1: *Quantum numbers, masses and width of the charmonium states with mass below the open charm production threshold from PDG. [5].*

The region **above D$\bar{\text{D}}$ threshold** is rich in interesting new physics. In this region, close to the $D\bar{D}$ threshold, one expects to find the four 1D states. Of these only the 1^3D_1, identified with the $\psi(3770)$ resonance and discovered by the Mark I collaboration [22], has been established. It is a wide resonance ($\Gamma(\psi(3770) = 27.3 \pm 1.0 MeV/c^2)$, which decays predominantly to $D\bar{D}$. The $J = 2$ states (1^1D_2 and 1^3D_2) are predicted to be narrow, because parity conservation forbids their decay to $D\bar{D}$. In addition to the D states, the radial excitations of the S and P states are predicted to occur above the open charm threshold. None of these states have been positively identified.

Some of the features of charmonium states are summarized in table 1.1. In the next section, there will be more details on the experimental on the energy region above $D\bar{D}$ threshold, in particular for those new states recently, mainly discovered at the B-factories.

1.5.3 New charmonia

A lot of new states have recently been discovered (X, Y, Z mesons), mainly in the hadronic decays of the B meson: these new states are associated with charmonium because they decay predominantly into charmonium states such as the J/ψ or the ψ', but their interpretation is far from obvious. In this section, a brief summary of the experimental data and the possible interpretation is presented.

Curiously, three charmonium-like states were observed with similar masses near 3.94 GeV/c^2 , but in quite different processes, as summarized in table 1.2 [26].

The charmoniumlike state X(3940) has been observed by Belle in the double charmonium production in the process $e^+e^- \to J/\psi D\bar{D}^*$ in the mass spectrum recoiling against the J/ψ [16], to be confirmed by this analysis,

State	J^{PC}	Mass (MeV/c^2)	Γ (MeV/c^2)	Decay	Production	Collaboration
X(3940)	?$^{?+}$	$3942^{+7}_{-6}\pm 8$	$37^{+26}_{-28}\pm 8$	$D\bar{D}^*$	$e^+e^- \to J/\psi\, X(3940)$	Belle
X(4160)	?$^{?+}$	$4156^{+25}_{-20}\pm 15$	$139^{+11}_{-61}\pm 21$	$D^*\bar{D}^*$	$e^+e^- \to J/\psi\, X(4160)$	Belle
Y(3940)	?$^{?+}$	$3943\pm 11 \pm 13$	$87\pm 22 \pm 26$	$\omega J/\psi$	$B \to KY(3940)$	Belle
Y(3940)	?$^{?+}$	$3914.6^{+3.8}_{-3.4}\pm 2.0$	$34^{+12}_{-8}\pm 5$	$\omega J/\psi$	$B \to KY(3940)$	BaBar
Z(3930)	2^{++}	$3929\pm 5 \pm 2$	$29 \pm 10 \pm 2$		$\gamma\gamma \to Z(3940)$	Belle

Table 1.2: *Measured parameters of the XYZ(3940) states.*

for the *BABAR* collaboration. X(3940) state is tentatively identified with $\eta_c(3S)$. In addition Belle found a new charmoniumlike state, X(4160), in the processes $e^+e^- \to J/\psi\, X(4160)$ decaying into $D^*\bar{D}^*$ with a significance of 5.1σ [23]. Both the X(3940) and the X(4160) decay to open charm final states and therefore could be attributed to 3^1S_0 and 4^1S_0 conventional charmonium states. However, the problem with this assignment is that potential models predict masses for these levels to be significantly higher than those measured for the X(3940) and X(4160).

The Y(3940) state was observed by Belle as a near-threshold enhancement in the $\omega J/\psi$ invariant mass distribution for exclusive $B \to K\omega J/\psi$ decays with a statistical significance of 8.1σ [24]. Also *BABAR* found an $\omega J/\psi$ mass enhancement at ~ 3.915 GeV/c^2 in the decays $B \to K^{0,+} \to \omega J/\psi$ [25] and confirmed the Belle result. The Y(3940) mass is two standard deviations lower than the Z(3930) mass, and three standard deviations lower than for the X(3940); the width agrees with the Z(3930) and X(3940) values.

The Z(3930) state was found by Belle in two-photon collisions $\gamma\gamma \to D\bar{D}$ with a mass ~ 3.930 GeV/c2. The production rate and the angular distribution in the $\gamma\gamma$ center-of-mass frame favor the interpretation of Z(3930) as the $\chi_{c2}(2P)$ charmonium state.

For all other new states (X(3872), Y(4260), Y(4320) and so on) the interpretation is not at all clear, with speculations ranging from the missing $c\bar{c}$ states, to molecules, tetraquark states, and hybrids.

Chapter 2

Double charmonium production

2.1   Introduction

The exclusive production of a pair of double heavy mesons with c-quarks in e^+e^- annihilation has attracted considerable attention in the last years. In fact, at the beginning of these studies, the cross section of the process $e^+e^- \to J/\psi\ \eta_c$, which was measured in the experiments on *BABAR* and Belle detectors at the energy $\sqrt{s}=$ 10.6 GeV, resulted to be

$$\sigma(e^+e^- \to J/\psi + \eta_c) \times \mathcal{B}(\eta_c \to \geq 2\ charged) = \left\{ \begin{array}{c} 25.6 \pm 2.8 \pm 3.4 \ [27] \\ 17.6 \pm 2.8^{+1.5}_{-2.1} \ [28] \end{array} \right.$$

(2.1)

and led to a discrepancy with the theoretical calculation in the framework of nonrelativistic QCD (NRQCD) by an order of magnitude. This conclusion is based on calculations in which the relative momenta of heavy quarks and bound state effects in the production amplitude were not taken into account. A set of calculations was performed to improve the nonrelativistic approximation for the process.

In particular, relativistic corrections to the cross section $\sigma(e^+e^- \to J/\psi + \eta_c)$ were considered in a *color singlet model* in reference [29] using the methods of NRQCD [14]. A synthesis of this method will be done in section 2.2.1.

Another attempt to take into account the relativistic corrections was done in the framework of the *light-cone formalism* [30, 31], described here in section 2.2.4. With this formalism the discrepancy between experiment and theory can be eliminated completely by considering the intrinsic motion of heavy quarks forming the doubly heavy mesons.

In addition, *perturbative corrections* of order α_s to the production amplitude were calculated in reference [32], where Zhang, Gao and Chao could increase the cross section by a factor 1.8 (see section 2.3).

On account of different values of relativistic corrections obtained in references [29, 30, 31] and the importance of a relativistic consideration of the process $e^+e^- \rightarrow J/\psi + \eta_c$ in solving the doubly heavy meson production problem, Ebert and Martynenko [33] have performed a new investigation of relativistic and bound state effects. This investigation is based on the relativistic quark model which provides the solution in many tasks of heavy quark physics. In [34, 35] they have demonstrated how the original amplitude, describing the physical process, must be transformed in order to preserve the relativistic plus bound state corrections connected with the one-particle wave functions and the wave function of a two-particle bound state.

In particular, in paper [33] they extend the method to the case of the production of a pair $(\mathcal{P} + \mathcal{V})$ of double heavy mesons containing quarks of different flavours b and c. They consider the internal motion of heavy quarks in both produced pseudoscalar $\mathcal{P}$ and vector $\mathcal{V}$ mesons, and the results of the cross-section will be presented in section 2.2.3.

Two more sections are in this chapter: section 2.4 where a synthesis of the recent results on the analysis $e^+e^- \rightarrow \gamma^* \rightarrow J/\psi + X$ is done and the possible interpretations of the state X(3940), which is expected to be seen in the double charmonium production process via one virtual photon, are illustrated. This last section is particularly interesting for this analysis, which has in its aims also to confirm this state, also seen in Belle in the recoil spectrum. Finally in section 2.5 we will briefly describe the theory concerning the double charmonium production with two virtual photons involved in the process $(e^+e^- \rightarrow \gamma^*\gamma^* \rightarrow c\bar{c}c\bar{c})$.

2.2   Cross section

If charmonium is the only hadron in the initial or final state, the color-singlet model should be accurate up to corrections that are higher order in v. The simplest examples of such processes are electromagnetic annihilation decays, such as $J/\psi \rightarrow e^+e^-$ and $\eta_c \rightarrow \gamma\gamma$, and exclusive electromagnetic production processes, such as $\gamma\gamma \rightarrow \eta_c$.

Another process for which the color-singlet model should be accurate is e^+e^- annihilation into exactly two charmonia. There are no hadrons in the initial state, and the absence of additional hadrons in the final state can be guaranteed experimentally by the monoenergetic nature of a 2-body final state. For many charmonia, the NRQCD matrix element can be determined from the electromagnetic annihilation decay rate of either the charmonium state itself or of another state related to it by spin symmetry. Cross sections for double-charmonium can therefore be predicted up to corrections

suppressed by powers of v^2 without any unknown phenomenological factors.

One problem with e^+e^- annihilation into exclusive double charmonium is that the cross sections are very small at energies large enough to trust the predictions of perturbative QCD. A naive estimate of the cross section for $J/\psi + \eta_c$ in units of the cross section for $\mu^+\mu^-$ is:

$$R[J/\psi + \eta_c] \sim \alpha_s^2 \left(\frac{m_c v}{E_{beam}}\right)^6 . \qquad (2.2)$$

The 2 powers of α_s are the fewest required to produce a $c\bar{c}+c\bar{c}$ final state. There is a factor of $(m_c v^3)$ associated with the wavefunction at the origin for each charmonium. These factors in the numerator are compensated by factors of the beam energy E_{beam} in the denominator to get a dimensionless ratio.

As an example, consider e^+e^- annihilation with center-of-mass energy $2E_{beam} = 10.6$ GeV. If we set $v^2 \approx 0.3$, $\alpha_s \approx 0.2$, and $m_c \approx 1.4$ GeV, we get the naive estimate $R[J/\psi + \eta_c] \approx 4 \times 10^{-7}$. This should be compared to the total ratio $R[hadrons] \approx 3.6$ for all hadronic final states [36]. The decay of the J/ψ into the easily detectable e^+e^- or $\mu^+\mu^-$ modes suppresses the observable cross section by another order of magnitude.

Fortunately, the era of high-luminosity B factories has made the measurement of such small cross sections feasible. Braaten and Lee [29] calculated the cross sections for exclusive double-charmonium production via e^+e^- annihilation into a virtual photon. This process produces only charmonium states with opposite charge conjugation. The cross sections for charmonium states with the same charge conjugation, which proceed through e^+e^- annihilation into two virtual photons [37, 38] will be illustrated in section 2.5.

2.2.1 Color-singlet model calculation

In this section, the cross sections for e^+e^- annihilation through a virtual photon into a double-charmonium final state $H_1 + H_2$ are calculated by using the color-singlet model. The color-singlet model (CSM) can be obtained from the NRQCD factorization formula by dropping all of the colour-octet terms and all but one of the colour-singlet terms. The term that is retained is the one in which the quantum numbers of the $Q\bar{Q}$ pair are the same as those of the quarkonium.

Charge conjugation symmetry requires one of the charmonia to be a $C = -$ state and the other to be a $C = +$ state. The $C = -$ states with narrow widths are the $J^{PC} = 1^{--}$ states J/ψ and $\psi(2S)$, the 1^{+-} state h_c , and the yet-to-be-discovered 2^{--} state $\psi_2(1D)$.

27

The $C = +$ states with narrow widths are the 0^{-+} states η_c and $\eta_c(2S)$, the J^{++} states $\chi_{cJ}(1\mathrm{P})$, $J = 0, 1, 2$, and the yet-to-be-discovered 2^{-+} state $\eta_{c2}(1\mathrm{D})$. The results will be express in terms of the ratio $R[H_1 + H_2]$ defined by

$$R[H_1 + H_2] = \frac{\sigma[e^+e^- \to H_1 + H_2]}{\sigma[e^+e^- \to \mu^+\mu^-]} \qquad (2.3)$$

In the text, only the results for R summed over helicity states will be given. These results may facilitate the use of partial wave analysis to resolve the experimental double-charmonium signal into contributions from the various charmonium states.

When the e^+e^- beam energy E_{beam} is much larger than the charm quark mass m_c, the relative sizes of the various double-charmonium cross sections are governed largely by the number of kinematic suppression factors r^2, where the variable r is defined by

$$r^2 = \frac{4m_c^2}{E_{beam}^2}. \qquad (2.4)$$

If we set $m_c = 1.4$ GeV and $E_{beam} = 5.3$ GeV, the value of this small parameter is $r^2 = 0.28$. The asymptotic behavior of the ratio $R[H_1 + H_2]$ as $r \to 0$ can be determined from the helicity selection rules for exclusive processes in perturbative QCD. For each of the $c\bar{c}$ pairs in the final state, there is a suppression factor of r^2 due to the large momentum transfer required for the c and $\bar{c}$ to emerge with small relative momentum. Thus, at any order in α_s, the ratio $R[H_1 + H_2]$ must decrease at least as fast as r^4 as $r \to 0$. However it may decrease more rapidly depending on the helicity states of the two hadrons. There is of course a constraint on the possible helicities from angular momentum conservation: $|\lambda_1 - \lambda_2| = 0$ or 1.

The asymptotic behavior of the ratio $R[H_1(\lambda_1) + H_2(\lambda_2)]$ depends on the helicities λ_1 and λ_2. The helicity selection rules imply that the slowest asymptotic decrease $R \sim r^4$ can occur only if the sum of the helicities of the hadrons is conserved. Since there are no hadrons in the initial state, hadron helicity conservation requires $\lambda_1 + \lambda_2 = 0$. The only helicity state that satisfies both this constraint and the constraint of angular momentum conservation is $(\lambda_1, \lambda_2) = (0, 0)$. For every unit of helicity by which this rule is violated, there is a further suppression factor of r^2.

So, the resulting estimate for the ratio R at leading order in α_s is

$$R_{QCD}[H_1(\lambda_1) + H_2(\lambda_2)] \sim \alpha_s^2 (v^2)^{3+L_1+L_2} (r^2)^{2+|\lambda_1+\lambda_2|}. \qquad (2.5)$$

The factor of v^{3+2L} for a charmonium state with orbital angular momentum L comes from the NRQCD factors. At leading order of α_s, there may of

course be further suppression factors of r^2 that arise from the simple structure of the leading-order diagrams for $e^+e^- \to c\bar{c} + c\bar{c}$ in Fig. 2.1, but these suppression factors are unlikely to persist to higher orders in α_s.

The QED diagrams for $e^+e^- \to c\bar{c}(^3S_1) + c\bar{c}$ in Fig. 2.2 give contributions to $R[J/\psi + H_2]$ that scale in a different way with r. This case is actually interesting for the analysis documented in this thesis. As $r \to 0$, there is a contribution to the cross section from these diagrams into the cross section for $\gamma + H_2$ and the fragmentation function for $\gamma \to J/\psi$. This fragmentation process produces J/ψ in a $\lambda_{J/\psi} = \pm 1$ helicity state. The hard-scattering part of the process produces only one $c\bar{c}$ pair with small relative momentum, so there is one fewer factor of r^2 relative to equation 2.5. The cross section for $\gamma + H_1$ is still subject to the helicity selection rules of perturbative QCD, so the pure QED contribution to the ratio R has the behavior

$$R_{QED}[J/\psi\,(\pm 1) + H_2(\lambda_2)] \sim \alpha^2 (v^2)^{3+L_2} (r^2)^{1+|\lambda_2|}. \tag{2.6}$$

There may also be interference terms between the QCD and QED contributions whose scaling behavior is intermediate between equations 2.5 and 2.6.

2.2.2   Calculation of the cross sections

In this section, the cross sections for exclusive double-charmonium production in e^+e^- annihilation at the B factories is presented, and partially calculated.

The results in section 2.2.1 were expressed in terms of the ratio R defined in equation 2.3. The corresponding cross sections are:

$$\sigma[H_1 + H_2] = \frac{4\pi\alpha^2}{3s} R[H_1 + H_2] \tag{2.7}$$

The ratios R depend on a number of inputs: the coupling constants α_s and α, the charm quark mass m_c, and the NRQCD matrix elements $\langle O_1 \rangle$.

The value of the QCD coupling constant α_s depends on the choice of the scale μ. In the QCD diagrams of Fig. 2.1, the invariant mass of the gluon is $\sqrt{s/2}$. We therefore choose the scale to be $\mu = 5.3$ GeV. The resulting value of the QCD coupling constant is $\alpha_s(\mu) = 0.21$.

The numerical value for the pole mass m_c of the charm quark is unstable under perturbative corrections, so it must be treated with care. Since the expressions for the electromagnetic annihilation decay rates include the perturbative correction of order α_s the appropriate choice for the charm quark mass m_c in these expressions is the pole mass with corrections of order α_s included. It can be expressed as

29
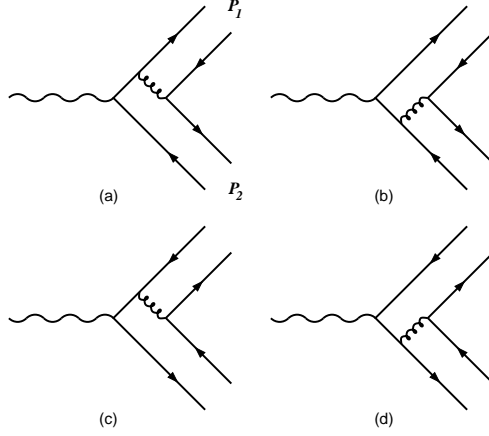
Figure 2.1: *QCD diagrams that can contribute to the color-singlet process* $\gamma^* \to c\bar{c} + c\bar{c}$
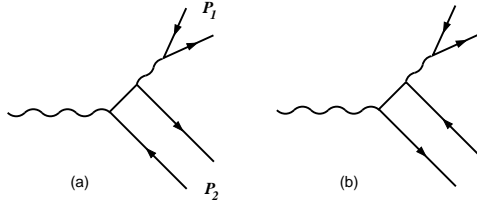
Figure 2.2: *QED diagrams that can contribute to the color-singlet process* $\gamma^* \to c\bar{c}(^3S_1) + c\bar{c}$

$$m_c = \bar{m}_c(\bar{m}_c)\left(1 + \frac{4}{3}\frac{\alpha_s}{\pi}\right). \qquad (2.8)$$

Taking the running mass of the charm quark to be $\bar{m}_c(\bar{m}_c) = 1.2 \pm 0.2$ GeV, the NLO pole mass is $m_c = 1.4 \pm 0.2$ GeV.

The Braaten-Lee predictions for the double charmonium cross sections without relativistic corrections are given in table 2.1.[1]

The Braaten-Lee predictions for the double charmonium cross sections for the S-wave states $(\eta_c, \eta_c(2S), J/\psi, \psi(2S))$ including the leading relativistic correction are obtained by multiplying the values in table 2.1 by the factor:

---

[1]Only values interesting for this analysis have been reported. For all calculations see [29]

$H_2 \setminus H_1$	J/ψ	$\psi(2S)$
η_c	3.78 ± 1.26	1.57 ± 0.52
$\eta_c(2S)$	1.57 ± 0.52	0.65 ± 0.22
χ_{c0}	2.40 ± 1.02	1.00 ± 0.42
χ_{c1}	0.38 ± 0.12	0.16 ± 0.05
χ_{c2}	0.69 ± 0.13	0.29 ± 0.06

Table 2.1: *Cross sections in fb for e^+e^- annihilation into double-charmonium states $H_1 + H_2$ without relativistic corrections. The errors are only those from variations in the NLO pole mass $m_c = 1.4 \pm 0.2$ GeV.*

$$\left(1 + \frac{8Y + 3(Y+4)r^2 - 5r^4}{12(r^2 - Y)} \left\langle v^2 \right\rangle_{J/\psi} + \frac{2Y + (Y+14)r^2 - 5r^4}{12(r^2 - Y)} \left\langle v^2 \right\rangle_{\eta_c} \right)^2$$

$$\times \left(1 - \frac{1}{6} \left\langle v^2 \right\rangle_{J/\psi} \right)^{-2} \left(1 - \frac{1}{6} \left\langle v^2 \right\rangle_{\eta_c} \right)^{-2} \times \frac{M_{J/\psi} M_{\eta_c}}{4m_c^2} \times \left(\frac{P_{CM}/E_{beam}}{(1 - r^2)^{1/2}} \right)^3 \quad (2.9)$$

where

$$Y = -\frac{\alpha}{\alpha_s} \left(1 + \frac{\alpha}{3\alpha_s} \right)^{-1}, \qquad \left\langle v^2 \right\rangle_H \approx \frac{M_H^2 - 4m_c^2}{4m_c^2} \quad (2.10)$$

and m_c is the pole mass of the charm quark. The first factor in 2.9, which appears squared, comes from the expansion of the amplitude in powers of the relative velocity of the $c\bar{c}$ pair. The values of $\left\langle v^2 \right\rangle_H$ follow from the Gremm-Kapustin relation [39]. The resulting cross sections are given in table 2.2. The error bars are those associated with the uncertainty in the NLO pole mass m_c only.

$H_2 \setminus H_1$	J/ψ	$\psi(2S)$
η_c	$7.4^{+10.9}_{-4.1}$	$6.1^{9.5}_{3.4}$
$\eta_c(2S)$	$7.6^{+11.8}_{-4.1}$	$5.3^{+9.1}_{-2.9}$

Table 2.2: *Cross sections in fb for e^+e^- annihilation into S-wave double-charmonium states $H_1 + H_2$ including relativistic corrections. The errors are only those from variations in the NLO pole mass $m_c = 1.4 \pm 0.2$ GeV.*

The correction factors indicate that the relativistic corrections to the cross sections involving $2S$ states are too large to be calculated reliably using the chosen method. Indeed these factors are $(1.80)^2$, $(1.64)^2$, $(2.16)^2$, respectively for $J/\psi + \eta_c(2S)$, $\psi(2S) + \eta_c$, $\psi(2S) + \eta_c(2S)$.

Note that the method for calculating the relativistic correction significantly increases the sensitivity to the charm quark mass. The errors from varying m_c in table 2.1 are about 50% for the S-wave states, while the errors in table 2.2 correspond to increasing or decreasing the cross section by about a factor of 3. The strong sensitivity to m_c is another indication that this method for calculating the relativistic corrections is unreliable. So we can therefore take the values in table 2.1 to be correct predictions for the cross sections and use table 2.2 as an indication of the possible size of the relativistic corrections.

2.2.3 Cross section for the production of pseudoscalar and vector double heavy mesons

An other approach to calculate the cross section for the double charmonium production from e^+e^- annihilation is that proposed by Ebert and Martynenko in [33]. In their calculations, they take into account the internal motion of heavy quarks in both produced pseudoscalar $\mathcal{P}$ and vector $\mathcal{V}$ mesons. They obtain the cross sections for the production of a pair of S-wave double heavy mesons with opposite charge parity, in general, containing b and c quarks from e^+e^- annihilation. This work was done for generic pseudoscalar and vector heavy mesons. Then they have taken into account all possible sources of relativistic corrections including the transformation factors for the two quark bound state wave function, and they have investigated the role of relativistic and bound state effects in the total production cross sections using predictions of the relativistic quark model for a number of parameters entering in the obtained analytical expressions.

The total cross section for the exclusive production of $\mathcal{P}$ and $\mathcal{V}$ doubly heavy mesons in e^+e^- annihilation is then given by the following expression:

$$\sigma(s) = \frac{32\pi^3\alpha^2 M_0^2 |\Psi_0^{\mathcal{V}}|^2 \ |\Psi_0^{\mathcal{P}}|^2}{2187 M_{\mathcal{V}} M_{\mathcal{P}} s^8 k^{10}(1-k)^{10}} \left[k^3 Q_1 \alpha_{s2} T_1 + (1-k)^3 Q_2 \alpha_{s1} T_2 \right]^2 \times$$

$$\times \left\{ \left[1 - \frac{(M_{\mathcal{V}} + M_{\mathcal{P}})^2}{s^2} \right] \left[1 - \frac{(M_{\mathcal{V}} - M_{\mathcal{P}})^2}{s^2} \right] \right\}^{3/2}. \qquad (2.11)$$

In this formula, if m_1 and m_2 are the quark masses, $M_0, M_{\mathcal{V}}, M_{\mathcal{P}}$ are the masses of vector and pseudoscalar mesons consisting of heavy quarks,

expressed respectively as:

$$
\begin{aligned}
M_0 &= m_1 + m_2, \\
M_{\mathcal{V}} &= m_1 + m_2 + W_{\mathcal{V}}, \\
M_{\mathcal{P}} &= m_1 + m_2 + W_{\mathcal{P}},
\end{aligned}
\qquad (2.12)
$$

where $W_{\mathcal{V}}$ and $W_{\mathcal{P}}$ are the binding energies between the two quarks, the constants $\alpha_{s1} = \alpha_s(4m_1^2)$, $\alpha_{s2} = \alpha_s(4m_2^2)$, Q_1 and Q_2 are the electric charges of heavy quarks, $\Psi_0^{\mathcal{V},\mathcal{P}}$ are the wave function for the relative motion of heavy quarks in the vector and pseudoscalar meson at the origin in the rest frame, T_1 and T_2 are factors depending on quantities determining the numerical values of relativistic effects connected with the internal motion of the heavy quarks in vector and pseudoscalar double heavy mesons[2].

The results of this calculation of the cross section, expressed in 2.11 and presented in Fig. 2.3 in the case of the double charmonium, evidently show that only the relativistic analysis of the production processes can give reliable theoretical predictions for the comparison with the experimental data. It follows from Fig. 2.3 that with the growth of the quantum number n the nonrelativistic approximation doesn't work near the production threshold because the omitted terms in this case have the same order of the magnitude as the basic terms.

2.2.4   Light cone formalism

Another systematic approach to the study of hard exclusive processes is light cone formalism (LC). Within this approach the amplitude of hard exclusive process can be separated into two parts. The first part is *partons production at very small distances*, which can be treated within perturbative QCD. The second part is the hadronization of the *partons at larger distances*. This part contains information about nonperturbative dynamics of the strong interactions. For hard exclusive processes it can be parameterized by process independent distribution amplitudes (DA), which can be considered as hadrons' wave functions at light-like separation between the partons in the hadron. It should be noted that within LC one does not assume that the mesons are nonrelativistic. This approach can equally well be applied to the production of light and heavy mesons, if the DAs of the produced meson are known. For this reason, one can hope that within this approach one can study the production of excited charmonia states.

The first attempts to describe the experimental results obtained at Belle and BaBar collaborations within LC were done in papers [30, 40]. If the

---

[2]For the total espression of T_1 and T_2 see the reference [33].

$$e^+ + e^- \rightarrow J/\Psi + \eta'_c$$

$$e^+ + e^- \rightarrow \Psi' + \eta_c$$

$$e^+ + e^- \rightarrow \Psi' + \eta'_c$$
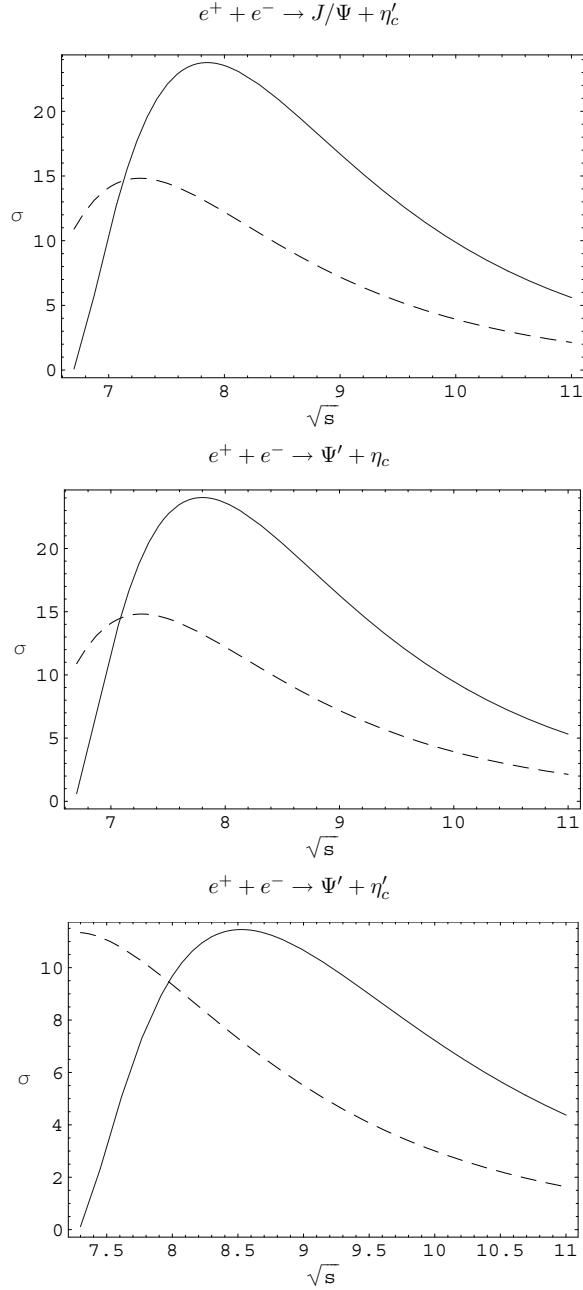
Figure 2.3: *The cross section in fb of e^+e^- annihilation into a pair of S-wave double charm heavy mesons with opposite charge parity as a function of the center-of-mass energy s (solid line). The dashed line shows the nonrelativistic result without bound state and relativistic corrections.*

34

center-mass energy $\sqrt{s}$ is very large, i.e., $\sqrt{s} \gg m_c$, one can take c-quark as a light quark. Then one can use light-cone wave-functions to describe nonperturbative effects of charmonia and a factorized form of the production amplitude in terms of these wave-functions and a perturbative part can be obtained. Such an approach for exclusive processes was proposed long time ago [41].

In comparison with the approach based on NRQCD for the process $e^+e^- \rightarrow J/\psi \ \eta_c$, where the expansion parameter is the velocity, the approach with light-cone wave-function is with the expansion parameters $\Lambda/\sqrt{s}$, where Λ is a soft scale and can be Λ_{QCD} , m_c and masses of charmonia.

In references [30, 31], the authors studied processes of double charmonium production from a e^+e^- annihilation with this approach.

Within the error of the calculation the results of this study are in agreement with Belle and *BABAR* experiments. In addition,in order to answer the question - why LC predictions are much greater than the leading order NRQCD predictions - numerical results of the calculation show that large disagreement between LC and the leading NRQCD predictions can be attributed to large contribution of relativistic and radiative corrections. From these results one can draw the conclusion that in hard exclusive processes relativistic and radiative corrections play a very important role and the consideration of such processes at the leading NRQCD approximation is unreliable.

The results of that paper are in agreement with recent NRQCD study of the process $e^+e^- \rightarrow J/\psi \ \eta_c$ [42, 43] where the authors took into account relativistic and one loop radiative corrections. However, Braguta in [31] showed also that the results of [42, 43] are overestimated by a factor 1.5.

On the other hand, Ma and Si in [30], have studied the exclusive production of $e^+e^- \rightarrow J/\psi \ \eta_c$, in which they have taken charm quarks as light quarks and used light-cone wave-functions to parameterize nonperturbative effects related to charmonia. In comparison with NRQCD factorization, the factorization of their approach may be achieved in a cleaner way and the perturbative coefficients will not have corrections with large logarithms like $ln(\sqrt{s}/m_c)$ from higher orders, while in the approach of NRQCD factorization, these large logarithms exist and call for resummation. The forms of these light-cone wave-functions are known if the energy scale is close to m_c or is very large. Unfortunately, these wave-functions at the considered energy scale, which is not close to m_c and far from being very large, are unknown. So, with a simple model of light-cone wave-functions, their are able to predict the cross-section which is at the same order of that measured by Belle. But this model may not represent completely the physics of charmonia.

State H_1H_2	$\sigma_{BABAR} \times \mathcal{B}(\eta_c \to \geq 2\ ch)$ (fb) [28]	$\sigma_{Belle} \times \mathcal{B}(\eta_c \to \geq 2\ ch)$ (fb) [27]	σ_{LC} (fb) [40]	σ_{NRQCD} (fb) [29]	σ (fb) [29]	σ (fb) [33]
$\Psi(1S)\eta_c$	$17.6 \pm 2.8^{+1.5}_{-2.1}$	$25.6 \pm 2.8 \pm 3.4$	26.7	3.78	7.4	7.8
$\Psi(1S)\eta_c(2S)$	$16.4 \pm 3.7^{+2.4}_{-3.0}$	$16.5 \pm 3.0 \pm 2.4$	26.6	1.57	7.6	7.0

Table 2.3: *Comparison of theoretical predictions (light-cone predictions [40], Braaten-Lee calculations with and without relativistic corrections[29] and Ebert-Martynenko predictions [33]) with experimental data (BABAR[28] and Belle [27]).*

2.3   Discrepancy between theory and experiment

As already mentioned above, the experimental results for the production of $J/\psi + \eta_c$ mesons measured at the Belle and *BABAR* experiments differ from theoretical calculations in the framework of NRQCD.

The experimental data on the production cross sections of a pair of S-wave charm mesons are presented in table 2.3. The numerical value for the cross section of $J/\psi + \eta_c$ production at $\sqrt{s} = 10.6$ GeV, obtained on the basis of equation 2.11 amounts to the value 7.8 fb without the inclusion of QED effects. In this case relativistic and bound state corrections increase our nonrelativistic result by a factor 2.2 (see dashed lines in Fig. 2.3).

Accounting slightly different values of several parameters used in the Ebert-Martynenko model in the comparison with the Braaten-Lee model [29], that is the mass of c quark, the binding energies $W_{\mathcal{P},\mathcal{V}}$, one can find a good agreement between the two results for the production of the charmonium states, if relativistic corrections are taken into account (see the sixth column of table 2.3).

Keeping in mind also the calculation of Zhang-Gao-Chao, which includes additional perturbative corrections of order α_s, one can observe the convergence between the experimental data and theoretical results obtained on the basis of approaches combining nonrelativistic QCD and the relativistic quark model[3].

2.4   Previous results on e$^+$e$^-$ $\to$ J/ψ + X

The two main experimental results on this analysis come from the *BABAR* [28] and Belle [16] experiments.

In Figs. 2.4 are shown the mass distribution of the system recoiling against a reconstructed J/ψ in e^+e^- annihilations: *BABAR* made the analysis

---

[3]This model is not documented here. For any detail see [32]
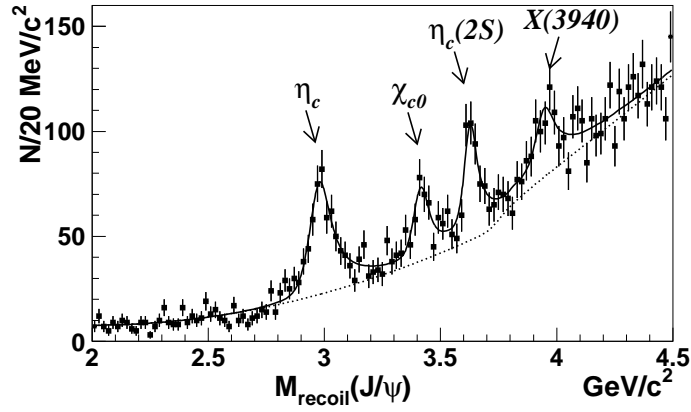
(a)
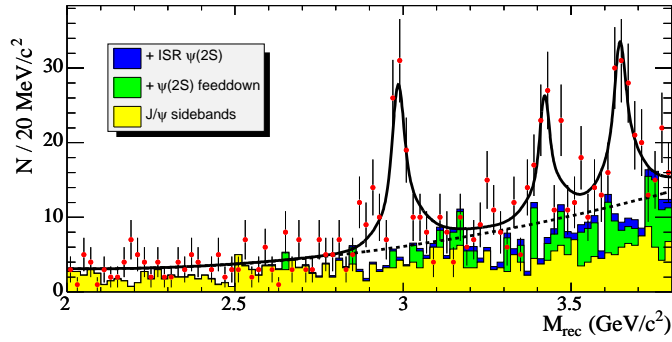
(b)

Figure 2.4: *The distributions of the mass recoiling against the reconstructed J/ψ in inclusive $e^+e^- \rightarrow J/\psi X$ for Belle (a) and BABAR (b).*

in the range 2.0 to 3.8 GeV/c^2, while Belle's authors saw the distribution up to 4.5 GeV/c^2,

It's possible to note that Belle's analysts reported also an evidence of a state around 3.943 Gev/c^2, named X(3940), candidate to be the η_c (3S) state. In the section 2.4.1 we will presente a discussion about the interpretation of this state.
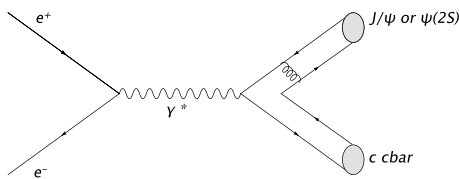
Figure 2.5: *Feynman diagram for the double charmonium production from e^+e^- annihilation, with a reconstructed $c\bar{c}$ state.*

2.4.1   X(3940) interpretation

The state X(3940) has been seen only by Belle experiment recoiling against J/ψ. One of the aims of the analysis described in this thesis is also to confirm this state with BABAR data. The state has a Breit-Wigner mass of 3943 ±6±6 MeV and a width of less than 52 MeV at 90% C.L. [16]. The X is seen to decay to $D\bar{D}^*$ and not to $\omega J/\psi$ or $D\bar{D}$.

It is natural to attempt a 2P $c\bar{c}$ assignment for this state since the expected mass of the 2^3P_J multiplet is 3850-3980 MeV and the expected widths are 20-130 MeV [44]. Indeed, if the $D\bar{D}^*$ mode is dominant it suggests that the X(3940) is the χ_{c1}. There is, however, a problem with this assignment. Indeed if X(3940) is χ'_{c1}, one may expect a stronger signal of its ground state χ_{c1}. But in the same reaction, Belle collaboration didn't observe χ_{c1}. This has led to speculation that the X(3940) is the radially excited η_c (3S) . Unfortunately this interpretation also has its problems as the expected mass of the η_c (3S) is 4040-4060 MeV, approximately 100 MeV too high.

2.5   Double c$\bar{\text{c}}$ production via $\gamma^*\gamma^*$

The predictions and calculations until now were performed for final double charmonium states with even charge-conjugation parity (C-parity), where the e^+e^- pair decays in the final state via one virtual photon ($J^{PC} = 1^{--}$).
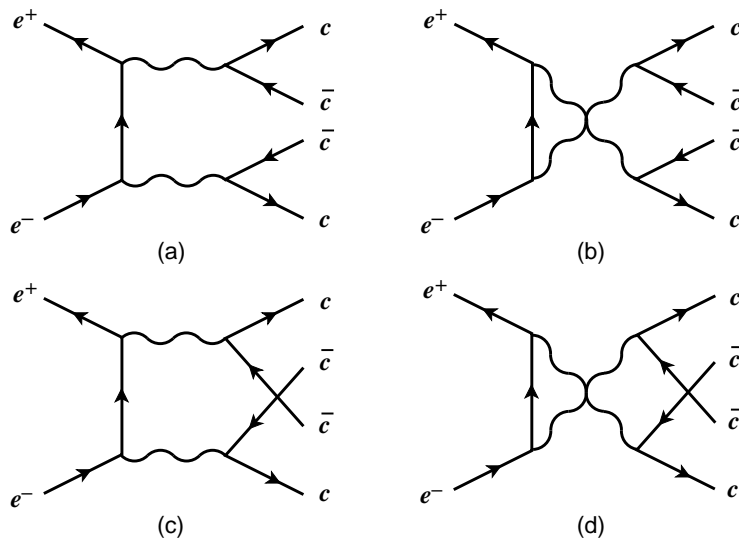
Figure 2.6: *QED diagrams for the process $e^+e^- \to \gamma^*\gamma^* \to c\bar{c}_1 c\bar{c}_1$.*

But one can calculate the cross sections for e^+e^- annihilation into two charmonium states that have the same C-parity, such as $J/\psi + J/\psi$. These processes proceed, at leading order in the QCD coupling α_s, through QED diagrams that contain two virtual photons (see Fig. 2.6). One might expect these cross sections to be much smaller than those for charmonia with opposite C-parity because they are suppressed by a factor of α^2/α_s^2. However, if both charmonia have quantum numbers $J^{PC} = 1^{--}$, then there is a contribution to the cross section in which each photon fragments into a charmonium [37]. The fragmentation contribution is enhanced by powers of E_{beam}/m_c, where E_{beam} is the beam energy and m_c is the charm-quark mass [37]. This enhancement can compensate for the suppression factor that is associated with the coupling constants. In particular, the predicted cross section for $J/\psi + J/\psi$ at the B factories is larger than that for $J/\psi + \eta_c$.

Bodwin, Braaten and Lee in [38] have calculated the cross sections for e^+e^- annihilation through two virtual photons into exclusive double charmonium states. The cross sections result to be particularly large if the two charmonia are both 1^{--} states. In the absence of radiative and relativistic corrections, the predicted cross section for the production of $J/\psi + J/\psi$ at the B factories is larger than that for $J/\psi + \eta_c$ by a factor of about 3.7. The perturbative and relativistic corrections for these two processes may be rather different and could significantly change the prediction for the ratio of the cross sections. Nevertheless, the inclusion of contributions from processes involving two virtual photons in the theoretical prediction for the cross

section for $J/\psi + \eta_c$ production is likely to decrease the large discrepancy between that prediction and the Belle measurement.

However, as was pointed out in [37, 38], the two-photon process contains photon-fragmentation contributions that are enhanced by factors $(E_{beam}/2m_c)^4$ from photon propagators and $log[8(E_{beam}/2m_c)^4]$ from a would-be collinear divergence. As a result, the predicted cross-section

$\sigma(e^+e^- \to J/\psi\,J/\psi) = 8.70 \pm 2.94$ fb is larger than the predicted cross-section $\sigma(e^+e^- \to J/\psi\,\eta_c) = 2.31 \pm 1.09$ fb. Corrections of higher order in α_s and v are likely to reduce the prediction for the J/ψ J/ψ cross-section by about a factor of three. Anyway, as visible in Fig. 2.4, no significant J/ψ J/ψ signal was observed in the invariant mass distribution.

Chapter 3

The *BABAR* experiment

The B factory PEP-II, located at the Stanford Linear Accelerator Center in Menlo Park, CA, and the *BABAR* detector, along with their performance for the years relevant for this thesis, will be described in this chapter.

The primary goal of the *BABAR* experiment is the systematic study of CP asymmetries in the decays of neutral B mesons. In addition to this, a sensitive measurement of the CKM matrix elements can be made, and a number of rare B meson decays may be measured, together enabling good constraints to be put on fundamental parameters of the Standard Model. A range of other physics may also be studied at BABAR, including other B physics, the physics of charm and tau leptons, and two-photon physics.

The cross section of $e^+e^- \rightarrow c\bar{c}$ events is of the same order of magnitude as the one of $e^+e^- \rightarrow b\bar{b}$ events. Therefore, high statistics charmed mesons and baryons are expected. In order to produced the hundreds of millions of B mesons necessary to study CP-sensitive rare decays, the B mesons must be produced at high luminosity in a relatively clean environment. To this end, the SLAC B factory studies electron-positron collisions at a center-of-mass (CM) energy of 10.58 GeV. This energy corresponds to the mass of the $\Upsilon(4S)$ resonance, which is a spin-1 bound state of a b quark and a b antiquark (a member of the "bottomonium" family of mesons).

The $\Upsilon(4S)$ mass is just above the $B\bar{B}$ production threshold, and this resonance decays almost exclusively through the strong interaction to approximately equal numbers of $B^0\bar{B}^0$ and B^+B^- pairs, for which the two branching fractions are measured to be equal to high precision [45] The *BABAR* experiment was designed and optimized to achieve the goals specified above. The PEP-II B Factory was designed to deliver the B mesons to the experiment.

Table 3.1 summarizes the cross sections for the various processes accessible by colliding two e^+e^- beams at the energy corresponding to the mass of the $\Upsilon(4S)$ in the center of mass reference frame [46].

$e^+e^- \rightarrow$	Cross-section (nb)
$b\bar{b}$	1.10
$c\bar{c}$	1.30
$s\bar{s}$	0.35
$u\bar{u}$	1.39
$d\bar{d}$	0.35
$\tau^+\tau^-$	0.94
$\mu^+\mu^-$	1.16
e^+e^-	≈ 40

Table 3.1: *Production cross-sections at $\sqrt{s} = 10.58$ GeV*

3.1   The PEP-II asymmetric collider

The PEP-II B factory [47] is part of the accelerator complex at SLAC, shown in Fig. 3.1. The electron beam is produced by the electron gun near the beginning of the two-mile long linear accelerator (the "LINAC"). The gun consists of a thermally heated cathode filament held under high voltage. Large numbers of electrons are "boiled off" the cathode, accelerated by the electric field, collected into bunches, and ejected out of the gun into the LINAC. The electron bunches are accelerated in the LINAC with synchronized radio-frequency (RF) electromagnetic pulses generated in RF cavities through which the beam passes by a series of 50 Megawatt klystron tubes[1]. The steering, bending, and focusing of the beam is carried out with magnets throughout the acceleration cycle.

After acceleration to an energy of approximately 1 GeV, the electron beam is directed to a damping ring, where the beam is stored for some time. As it circulates in the ring, it loses energy through synchrotron radiation and is continuously re-accelerated by RF cavities. The radiation and careful re-acceleration has the effect of reducing the emittance, or spatial and momentum spread of the beam, a necessary step in high-luminosity collisions. The "damped" beam is then re-directed to the LINAC and accelerated to 8.9 GeV. Half of the generated electron bunches are used for the generation of the positron beam. They are accelerated to approximately 30 GeV, extracted from the LINAC, and directed onto a tungsten target, producing electromagnetic showers that contain a large numbers of electron-positron pairs. The positrons are separated electromagnetically from the electrons, collected into

---

[1]Klystrons generate the pulses with their lower energy electron beams' passing through resonanant cavities
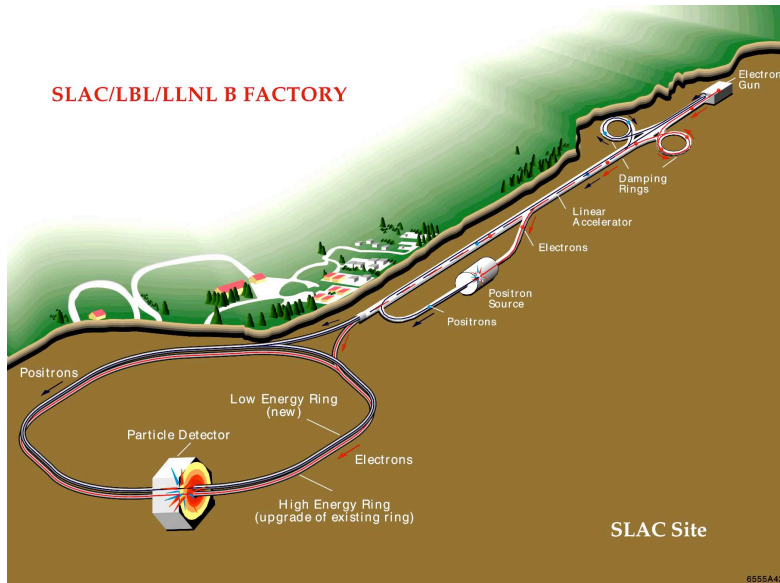
Figure 3.1: *A schematic depiction of the B factory accelerator complex at SLAC*

bunches, accelerated, and sent through the return line to the source end of the LINAC. The positron beam is then accelerated and shaped like the electron beam through the LINAC and its own damping ring, culminating in an energy of 3.1 GeV.

After reaching their respective collision energies, the electron and positron beams are extracted from the LINAC and directed to the PEP-II storage rings, the High Energy Ring (HER) for electrons and the Low Energy Ring (LER) for the positrons, both housed in the same tunnel of 2.2 km circumference. As they circulate, they are focused further by a complex of magnets and accelereted by RF cavities to compensate the synchrotron-radiation losses. In the interaction region IR-2 (one of the twelve such regions), where the *BABAR* detector is located, they are brought to a collision after a final-focus system squeeze the beams to the smallest possible emittance. During data taking, each ring contains about 1600 circulating bunches colliding every 5ns.

The collisions are then analyzed by the *BABAR* detector. About 10% of the time the beams are collided at an energy 40 MeV below the $\Upsilon(4S)$ resonance for calibration of the backgrounds, as no B mesons are produced then since this energy is below the $B\overline{B}$ threshold. As data is collected, the collisions and other losses reduce the currents in the rings, necessitating re-injection of electron and positron bunches. Initially in the life of the B factory from 1999-2002, data was taken for about an hour or two while
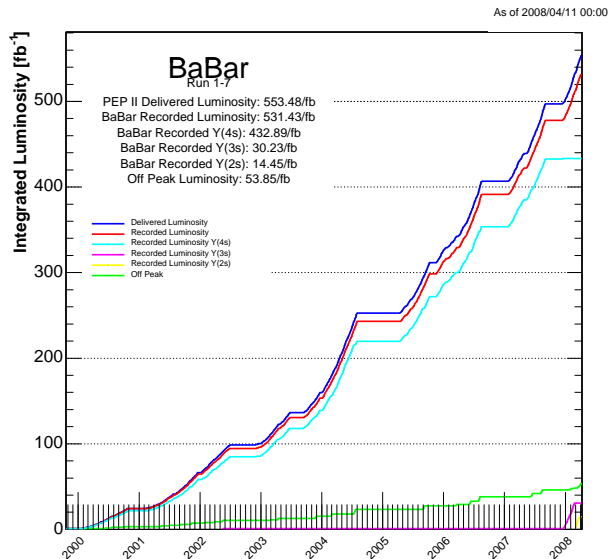
Figure 3.2: *Total integrated luminosity delivered by PEP-II and recorded by the BABAR detector.*

the currents diminished, and then additional current was injected into the rings for a few minutes. Data could not be taken during the injection due to the large backgrounds in the detector and the resulting danger to instrumentation. Notice that the detector would have to be put into a "safe" but non-operational state during injection, with, for instance, all high-voltage components ramped down to a lower, safer potential. Starting in 2003 a new scheme for injection, called *trickle* injection [49], was developed, where new bunches are continuously injected at a rate large enough to replenish beam losses but low enough to not damage the detector. This has allowed more efficient operation of the B-factory with 30% more integrated luminosity for a given highest instantaneous luminosity.

3.1.1 Luminosity

The luminosity $\mathcal{L}$ of the machine depends on the careful tuning of several parameters. This dependence is expressed as:

$$\mathcal{L} = \frac{nfN_1N_2}{A} \tag{3.1}$$

where n is the number of bunches in a ring, f is the bunch crossing

frequency, N_1 and N_2 are the number of particles in each bunch, and A is their overlap section.

The PEP-II collider was designed for an instantaneous luminosity of 3×10^{33} cm^{-2}s^{-1}, but has reached values of 1.2×10^{34} cm^{-2}s^{-1} due to improvements in the RF cavities, beam-shaping cavities, and magnet systems. The increased luminosity comes from larger beam currents (up to 3 A in the LER and 2 A in the HER) and a reduced emittance. With these specifications and trickle injection , the machine generated hundreds of pb^{-1} of integrated luminosity daily during normal operations, and has integrated hundreds of fb^{-1} throughout its operating lifetime. Fig. 3.2 shows the integrated luminosity provided by PEP-II collider in the period October 1999 - April 2008, along with the integrated luminosity recorded by the *BABAR* detector, that is 432.89 fb^{-1} collected at the $\Upsilon(4S)$ resonance, plus 53.85 fb^{-1} *off-peak*, This analysis uses both $\Upsilon(4S)$ data sample and the *off-resonance* data sample. In addition, in 2008 *BABAR* undertook a data taking at different Υ excited states energy, nominally 30.23 fb^{-1} at the $\Upsilon(3S)$ resonance and 14.45 fb^{-1} at the $\Upsilon(2S)$ resonance and an energy scan between $\Upsilon(4S)$ and the $\Upsilon(6S)$ mass, but these datasets are not considered in the present analysis.

3.1.2   Machine background

Beam-generated background causes high single-counting rates, data acquisition dead times, high currents and radiation damage of both detector components and electronics. This resulted in lower data quality and may have limited the lifetime of the apparatus. For this reason the background generated by PEP-II was studied in detail and the interaction region was carefully designed. Furthermore, background rates were continuously monitored during data acquisition to prevent critical operation conditions for the detector.

The primary sources of machine-generated background are:

- **synchrotron radiation** in the proximity of the interaction region. A strong source of background (many kW of power) is due to beam deflections in the interaction region. This component is limited by channeling the radiation out of *BABAR* acceptance with a proper design of the interaction region and the beam orbits, and placing absorbing masks before the detector components;

- **interaction between beam particles and residual gas** in either ring. This can have two different origins: beam gas bremsstrahlung and Coulomb scattering. Both types of interaction cause an escape of beam particles from their orbit. This background represents the

primary source of radiation damage for the inner vertex detector and the principal background for the other detector components;

- **electromagnetic showers generated by beam-beam collisions**. These showers are due to energy degraded e^+e^- produced by radiative Bhabha scattering and hitting the beam pipe within a few meters of the IP. This background is proportional to the luminosity of the machine and whereas it is under control, it is expected to increase in case of higher operation values of luminosity.

3.2   Detector overview

The *BABAR* detector was designed and constructed in such a way to fulfill all the above requirements. A cutaway picture of the detector is shown in Fig. 3.3. The main subsystems are:

1. the *Silicon Vertex Tracker (SVT)*, which provides precise position information on charged tracks, and also is the sole tracking device for very low-energy charged particles;

2. the *Drift Chamber (DCH)*, surrounding the vertex detector, filled with a helium-based gas, in order to try to minimize multiple scattering. In addition, it provides the main momentum measurement for charged particles and helps in particle identification through energy loss measurements;

3. the *Detector of Internally Reflected Cherenkov light (DIRC)*, which is designed and optimized for charged hadron particle identification;

4. the *Electromagnetic Calorimeter (EMC)*, composed by Cesium Iodide crystals: it is designed to detect electromagnetic showers from photons and electrons with excellent energy and angular resolution. The calorimeter provides good electron identification down to about 0.5 GeV, and information for neutral hadron identification;

5. a *superconducting solenoid*, surrounding the detector and producing a 1.5 T axial magnetic field;

6. the *Instrumented Flux Return (IFR)* which provides muon and neutral hadron identification.

The next few sections will describe the individual detector components.
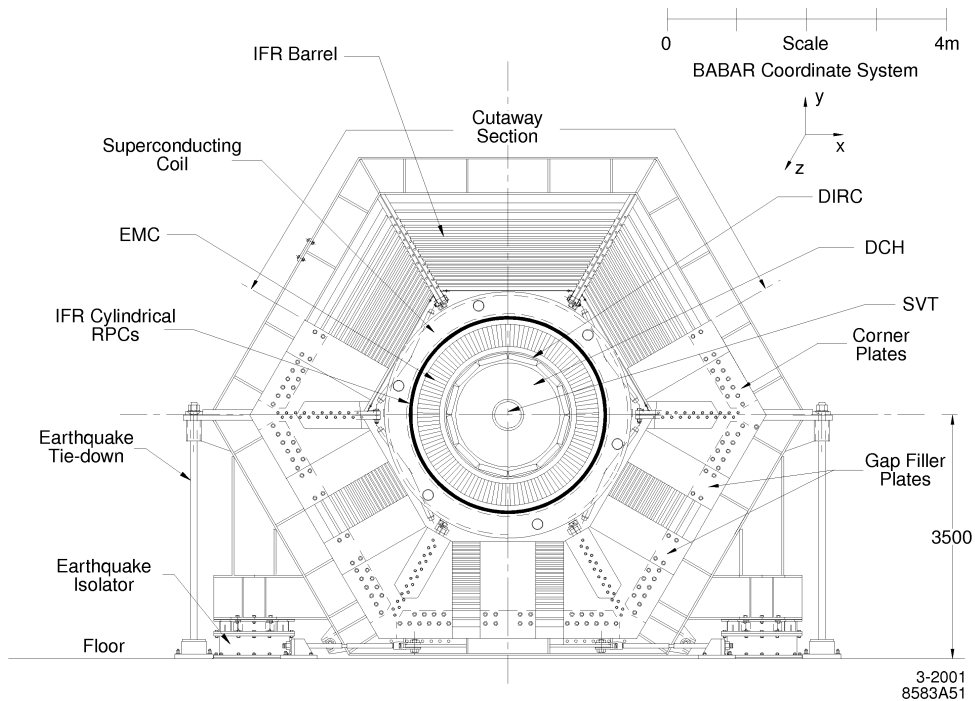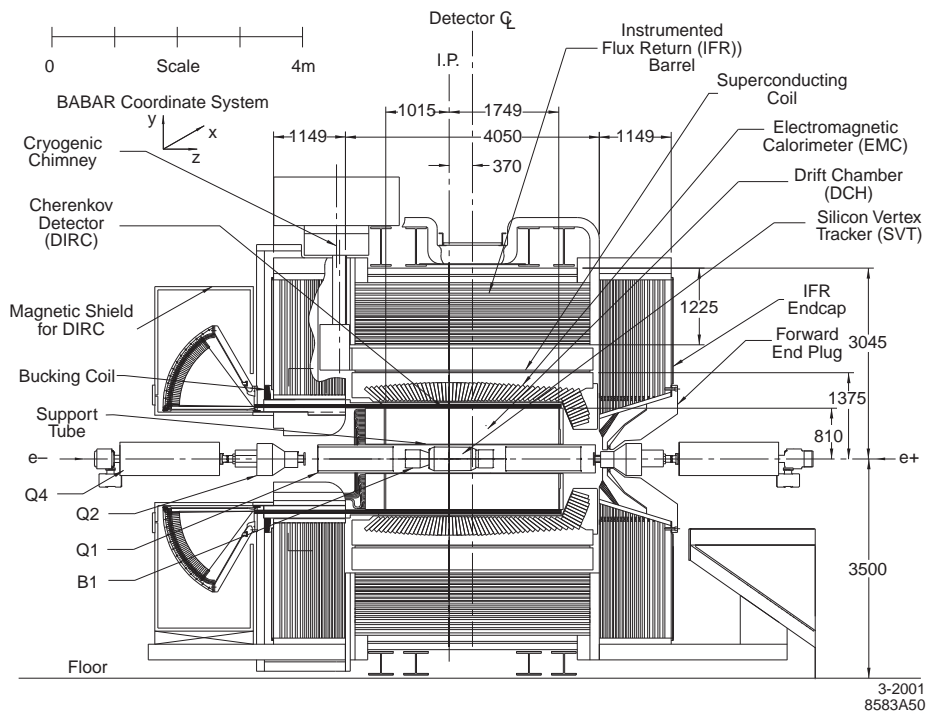
Figure 3.3: *Longitudinal (top) and front (bottom) view of the BABAR detector. All dimensions are given in millimeters.*

47

3.3 Tracking System

3.3.1 Silicon Vertex Detector

The SVT consists of five layers of double-sided silicon sensors segmented in both the z and ϕ directions (see Fig. 3.4), designed to measure accurately the positions and decay vertices of B mesons and other particle. This measurement is most accurate at small distances from the interaction, as the trajectory of the particles farther away is affected by multiple scattering within the detector. Thus, the first three layers are located as close to the beam pipe as possible. The outer two layers are closer to the drift chamber to facilitate matching SVT tracks with DCH tracks. They also provide pattern recognition in track reconstruction, and the only tracking information for charged particles with transverse momenta below 120MeV/c, as these may not reach the drift chamber. The SVT covers 90% of the solid angle in the CM frame, as visible in Fig. 3.5.

The silicon sensors are 300 μm-thick-high-resistivity n-type silicon wafers, with n^+ and p^+ strips running orthogonally on opposite sides. As high-energy particles pass through the sensors they displace orbital electrons, producing conducting electrons and positive holes that then migrate under the influence of an applied depletion voltage. The resulting electrical signal is read- off from the strips, amplified, and discriminated with respect to a signal threshold by front-end electronics. The time over threshold of the signal is related to the charge of the signal and is read out by the data acquisition system for triggered events. The position resolution is in the 10 μm - 50 μm range, depending on the orientation of the strip (ϕ or z) and the layer number.

The SVT is water-cooled and monitored for temperature, humidity, and position variations. Local and global position alignment is performed frequently in the online reconstruction software. As the SVT has to withstand a lifetime integrated radiation dose of 2 Mrad, the sensors have a high threshold for radiation damage. Nevertheless, they are easily damaged by high instantaneous or integrated doses, and an extensive system of radiation monitoring with PIN and diamond diodes can abort the beams if dangerous background levels develop. Up to 2007 the monitoring systems have prevented any significant damage from occurring and the SVT has performed extremely well, with an average track reconstruction efficiency of 97%, as shown in Fig. 3.6.

3.3.2 Drift Chamber

The Drift Chamber (DCH), a gaseous wire detector, is the main tracking device of the *BABAR*. It is used for the measurement of the momenta of charged
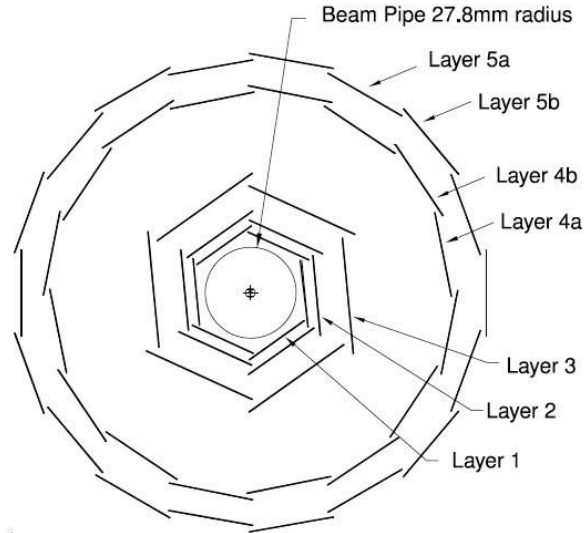
Figure 3.4: *Transverse cross section of the SVT.*
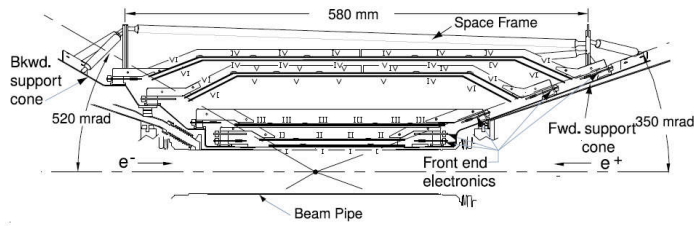
Figure 3.5: *Side view of the SVT.*
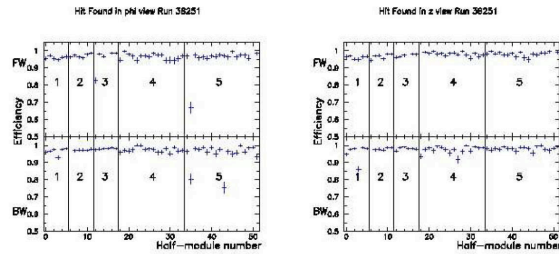
Figure 3.6: *SVT reconstruction efficiency in the ϕ view (left) and the z view (right) as measured in $e^+e^- \to \mu^+\mu^-$.*

49

particles, and it is the only tracker for the subset of long-lived particles such as K^0, that decay outside of the SVT. In addition, the DCH provides particle-identification capability by measuring track ionization losses as a function of position (dE/dx), particularly for tracks with momenta less than 700 MeV/c. The inner wall of the drift chamber is placed close to the SVT outer wall to facilitate track-matching between the two devices.

The specific requirements for the drift chamber, which operates in a 1.5T magnetic field, are to provide a spatial resolution better then 140 μm averaged over the cell and to supply identification for low momentum tracks through dE/dx with a resolution of 7% (40 measurements). In addition the drift chamber provides one of the principal triggers for the experiment. These requirements are met through the use of a small-cell design, low density gas and light materials. The choice of the gas mixture (mixture of 80% helium and 20% isobutane) is motivated by considerations of aging and avalanche size as well as minimizing multiple scattering in the chamber, which is accomplished by choosing helium as the primary gas component and aluminum as the lightweight material for the multiple field wires. A schematic side view of the *BABAR* drift chamber is shown in Fig. 3.7.

The *BABAR* drift chamber is a 280 cm long cylinder, with an inner radius of 23.6 cm and an outer radius of 81 cm. Since the *BABAR* events will be boosted in the forward direction, the design of the detector is optimized to reduce the material in the forward end. The forward end-plate is therefore made thinner in the acceptance region of the detector (12 mm thick) compared to the rear end-plate (24 mm thick), and all the electronics is mounted on the rear end-plate.

The cells are arranged in 10 super-layers of 4 layers each, for a total of 40
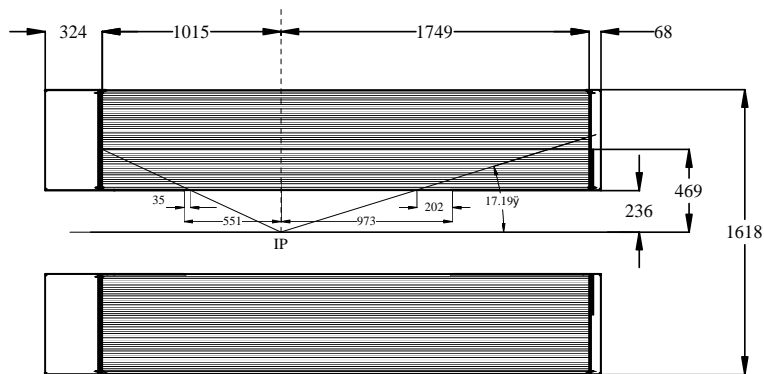
Figure 3.7: *Side view of the BaBar drift chamber. The dimensions are expressed in mm.*
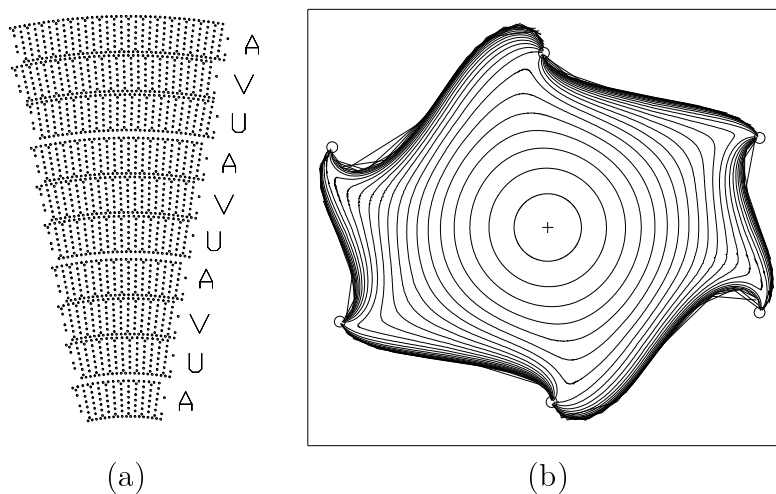
Figure 3.8: *(a) Cell layout in the BaBar Drift Chamber; (b) 50 ns isochrones in a typical BaBar drift chamber cell.*

layers. Axial (A) and stereo (U, V) super-layers are alternated following the pattern AUVAUVAUVA as shown in Fig. 3.8. The stereo angle varies from a minimum of 40 mrad in the innermost stereo super-layer, to a maximum of 70 mrad in the outermost stereo super-layer.

The field wires are grounded, while the sense wire is held at high voltage, typically around 1900 V. The space around the wires is filled with the gas mixture. High-energy particles ionize the gas as they traverse it, and the liberated electrons are then accelerated toward the sense wires, ionizing additional electrons, which are in turn accelerated themselves and result in the formation of a gas avalanche of electric charge. The avalanche collects on the sense wire with drift times of 10-500 ns and the charge and timing information of the signal is read-off through electronic circuits AC-coupled to the wire. The gain relative to the charge of the primary ionization is about 5×10^4. The grounded field wires produce a uniform electric field in the cell with evenly distributed isochrones, or contours of equal drift time.

The 7104 cells are hexagonal with typical dimension 1.2×1.8 cm^2. Fig. 3.8 shows the 50 ns isochrones in a typical cell in a 1.5 T magnetic field.

The DCH has demonstrated excellent performance throughout the life of BABAR with track-reconstruction efficiencies at the 95% level. This includes the effect of disconnecting a fraction of the wires in superlayers 5 and 6 that were damaged during the commissioning phase. The dE/dx response, with a resolution of about 7%, is shown in Fig. 3.9, and a new calibration in 2006 has improved the PID potential of this capability for high-energy tracks. The

achieved resolution on transverse momentum is $\sigma_{p_t}/p_t = (0.13 \pm 0.01)\%\dot{p}_t + (0:45 \pm 0:03)\%$, where p_t is given in units of GeV/c.
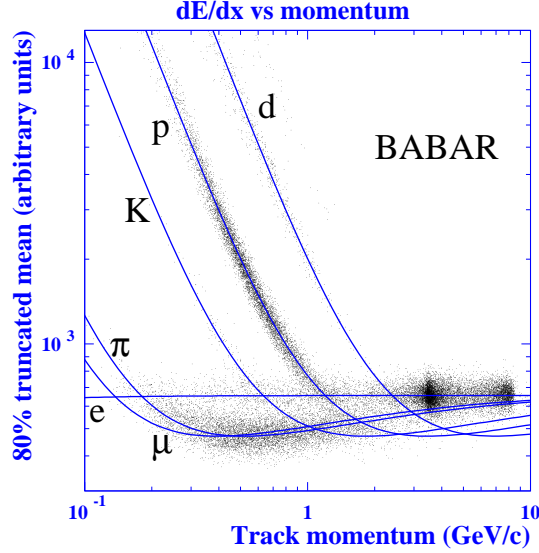
Figure 3.9: *DCH dE/dx as a function of track momentum.*

3.4 Cherenkov detector

Since the inner drift chamber tracker can provide sufficient $\pi - K$ separation up to only about 700 MeV/c, the dedicated Particle Identification (PID) system must perform well over a range from about 0.7 to 4.2 GeV/c, where the challenging upper end of this range must be achieved in the forward region of *BABAR*. *BABAR* has therefore a dedicated PID subdetector: the *DIRC* (Detector of Internally Reflection Cherenkov light) [50].

The phenomenon of the Cherenkov light emission is widely used in particle detectors technology. A charged particle traversing a medium with a velocity of β greater than the speed of light in that medium - that is $\beta > 1/n$, where n is the medium refraction index - emits directional electromagnetic radiation, called *Cherenkov light*. The angle of emission θ_C of the photons with respect to the track direction is called *Cherenkov angle* and is determined by the velocity of the particle with the relation

$$cos\theta_C = \frac{1}{n\beta} \qquad (3.2)$$

where $\beta = \frac{v}{c}$ is the particle velocity, and c the light velocity.

Thus, the measurement of θ_C determines β and, given the momentum of the particle, already measured in the DCH, the mass of the particle can be obtained. In fact, the DIRC is placed between the charged particle tracking detectors (Drift Chamber) and the electromagnetic calorimeter. In order to minimize the worsening of the energy resolution and volume, and hence cost, of the electromagnetic calorimeter, the DIRC has been designed to be thin and uniform in terms of radiation lengths. Moreover, for operation at high luminosity, it needs fast signal response, and should be able to tolerate high background.

In Fig. 3.10 a schematic view of DIRC geometry and basic principles of Cheerenkov light production, transport and image reconstruction.

The DIRC inverts the traditional concept of ring-imaging Cherenkov counters (RICH) in that it relies on the detection of Cherenkov photons trapped in the radiator due to total internal reflection. The DIRC radiator consists of 144 long, straight bars of synthetic quartz with rectangular section, arranged in a 12-sided polygonal barrel. The bars have transverse dimensions of 1.7 cm thickness by 3.5 cm width, and are 4.9 m long (see Fig. 3.11). The DIRC radiator extends through the steel of the solenoid flux return in the backward direction, to bring the Cherenkov light, through successive total internal reflections, outside the tracking and magnetic volumes. Only this end of the bars is instrumented. A mirror placed at the other end on each bar reflects forward-going photons to the instrumented end. The Cherenkov angle at which a photon was produced is preserved in the propagation, modulo a certain number of discrete ambiguities, some of which can be resolved by the photon arrival-time measurement. Remaining ambiguities are dealt with by the pattern recognition during Cherenkov angle
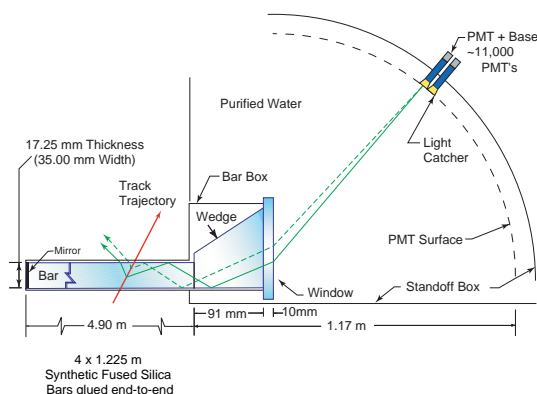
Figure 3.10: *Schema of the DIRC working principle.*
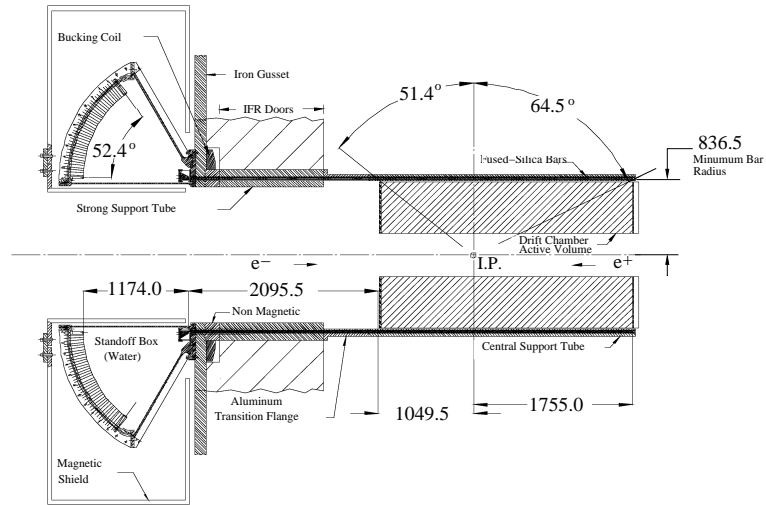
Figure 3.11: *Elevation view of the nominal DIRC system geometry. All dimensions are given in millimeters.*

reconstruction.

The radiator material used for the bars is synthetic fused silica (n = 1.474): the bars serve both as radiators and as light pipes for the portion of the light trapped in the radiator by total internal reflection. Synthetic silica has been chosen because of its resistance to ionizing radiation, its long attenuation length, its large index of refraction, its low chromatic dispersion within its wavelength acceptance.

At the instrumented end, the Cherenkov image is allowed to expand. The expansion medium is purified water, whose refractive index matches reasonably well that of the bars, thus minimizing the total internal reflection at the quartz-water interface. The region containing water is called the Stand-off Box. Cherenkov photons are detected in the visible and near-UV range by a close-packed array of linear focused 2.82 cm diameter photomultiplier tubes (PMTs), lying on an approximately toroidal surface. A small piece of quartz with a trapezoidal profile glued at the back end of each bar allows for significant reduction in the area requiring instrumentation because it folds one half of the image onto the other half, while also reflecting photons with large angles in the radial direction back into the detection array. The dimensions of the Stand-off Box are such that geometrical errors on angle measurements due to the finite size of bars and PMTs are of the order of the irreducible error due to quartz achromaticity. Six m^3 of water are needed to fill the Stand-off Box, and about 11000 PMTs to cover the detection area. The
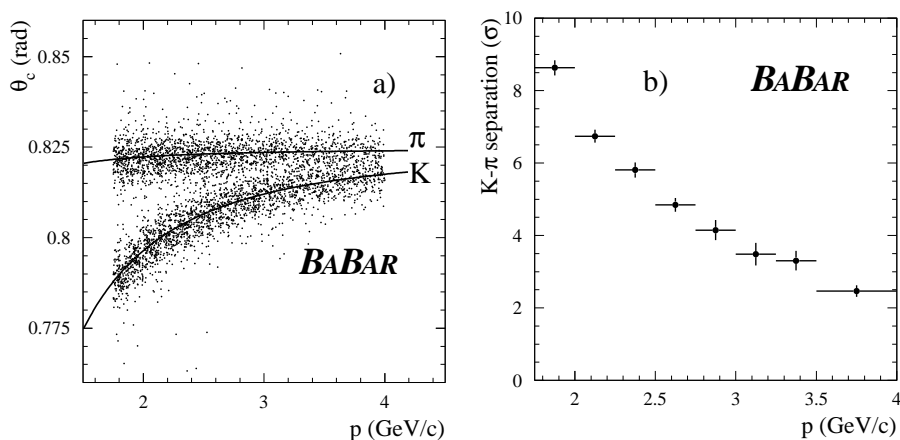
Figure 3.12: *(a) Cherenkov angle and (b) K - π discrimination power as a function of the momentum for single tracks. Discrimination quoted is computed performing the mean over all the polar angles.*

PMTs are operated directly in water, and are equipped with light concentrators. The PMTs are about 1.2 m away from the end of the quartz bar. Magnetic shielding around the Stand-off Box is further needed to maintain the magnetic fringe field at an acceptable level for PMT operation.

The DIRC is intrinsically a three-dimensional imaging device, giving the position and arrival time of the PMT signals. The three-dimensional vector pointing from the center of the bar end to the center of the PMT is computed, and then is extrapolated (using Snell's law) into the radiator bar in order to extract, given the direction of the charged particle, the Cherenkov angle. Timing information is used to suppress background hits and to correctly identify the track emitting the photons.

The discrimination between π and K due to the separation between the corresponding Cherenkov angles is greater then 3 standard deviations at about 3 GeV, as shown in Fig. 3.12, and higher for lower momenta. Due to the fact that the photons inside the quartz are totally reflected, the association between phototube hits and single track can have more than one solution. These possible ambiguities are solved by measuring the time difference between the hits in phototubes and the expected arrival time of each track with a precision of 1.7 ns, which allows to estimate the propagation time for a given Cherenkov angle, and therefore to reduce the background from uncorrelated photons.

3.5 Electromagnetic calorimeter

The electromagnetic calorimeter (EMC) [51] is designed to measure electromagnetic showers with excellent efficiency, energy and angular resolution over the energy range from 20 MeV to 9 GeV.

This functionality is necessary to reconstruct π^0 and η^0 mesons that decay to two photons, as well as for identification of high-energy photons from rare radiative B decays. The electron ID is necessary for J/ψ reconstruction, for tagging the flavor of the non-signal B in the event through semileptonic decays, as well as for reconstruction of semileptonic and rare B decays. The detector must be hermetic and operate within the 1.5 Tesla magnetic field. The amount of material in front of the EMC has been kept to a minimum in the design of the *BABAR* detector in order to allow for the detection of photons and electrons down to energies of 20 MeV.

The EMC is composed of 6580 Thallium-doped Cesium iodide (CsI(Tl)) scintillating crystals (Fig. 3.13), separated into a cylindrical barrel of 48 rings and a forward endcap of eight rings (Fig. 3.14). The EMC covers 90% of the CM acceptance and does not contain a backward endcap as the CM acceptance is low at backward polar angles. CsI(Tl) was chosen for its high light yield of 50,000 γ/MeV, allowing for excellent energy resolution, and its small Molière radius of 3.8 cm[2], which allows for excellent angular resolution. The transverse segmentation is at the scale of the Molière radius in order to optimize the angular resolution while limiting the number of crystals and readout channels.

The crystals serve as radiators for the traversing electrons and photons, with a short radiation length of 1.85 cm. The crystals scintillate under the influence of the showers, and the light is then passed through total internal reflection to the outer face of the crystal, where it is read out by silicon PIN diodes. As these diodes are well suited for operation in the high magnetic
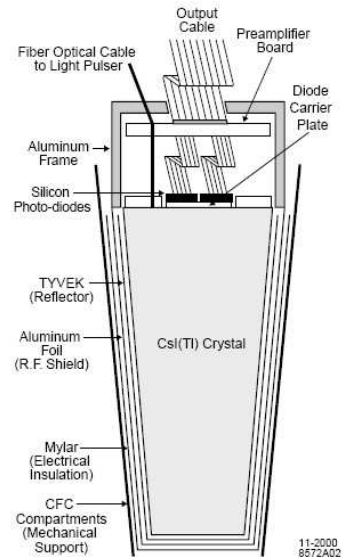
Figure 3.13: *Schematic view of the CsI(Tl) crystal with the front-end readout package mounted on the rear face.*

---

[2]The Molière radius is the intrinsic limit of the position resolution of electromagnetic showers in a crystal.
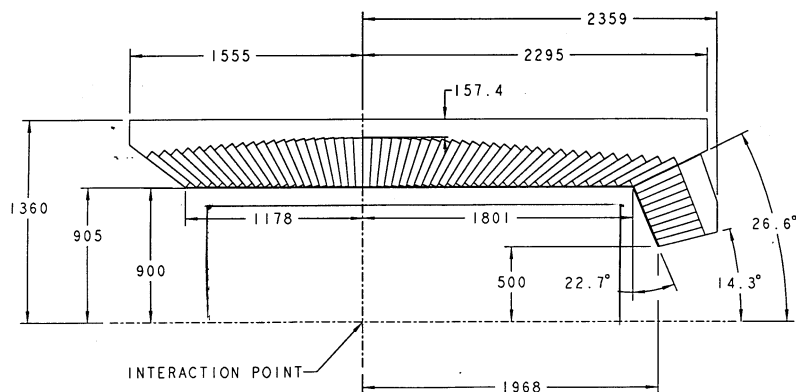
Figure 3.14: *Side view showing dimensions (in mm) of the calorimeter barrel and forward endcap.*

fields in the EMC, part of the motivation for the crystal choice was that the frequency spectrum of CsI(Tl) is detected by silicon PIN sensors with the high quantum efficiency of 85%. The EMC is cooled by water and Fluorinert coolant and monitored for changes in the environmental and radiation conditions and for changes in the light response of individual crystals.

The energy response of the EMC is calibrated using low-energy photons from a radioactive source and high-energy photons from radiative e^+e^- Bhabha events. As electromagnetic showers spread throughout several crystals, a reconstruction algorithm is used to associate activated crystals into clusters and either to identify them as photon candidates or to match individual maxima of deposited energy to extrapolated tracks from the DCH-SVT tracker. Additional PID is obtained from the spatial shape of the shower.

The designed energy resolution for EMC is given by:

$$\frac{\sigma(E)}{E(GeV)} = \frac{\sigma_1}{(E(GeV))^{1/4}} + \sigma_2 \tag{3.3}$$

where the expected $\sigma_1 \sim 1\%$ and $\sigma_2 \sim 1.2\%$ result to be higher when fitting the results from different methods of calibration, in fact they result to be: $\sigma_1 = (2.32 \pm 0.03)\%$ and $\sigma_2 = (1.85 \pm 0.07)\%$. These differences come from cross-talk effects on the electronic readout. As it is possible to see from the Fig. 3.15(a), the energy resolution ranges between 2% and 6%. The designed angular resolution is:

$$\frac{\sigma_{\theta,\phi}}{E(GeV)} = \frac{\sigma_1}{\sqrt{E(GeV)}} + \sigma_2 \qquad (3.4)$$

ranging between 3 and 10 mrad (Fig. 3.15(b)).
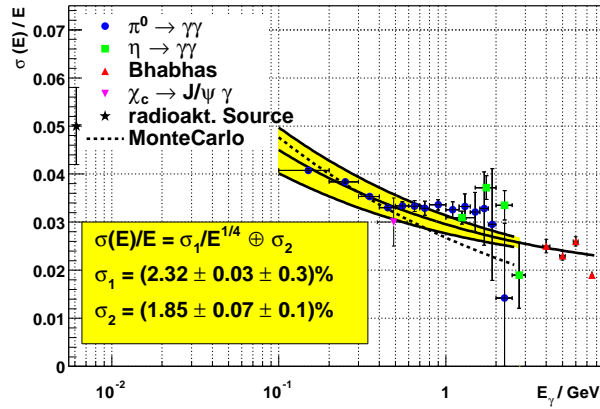
(a)
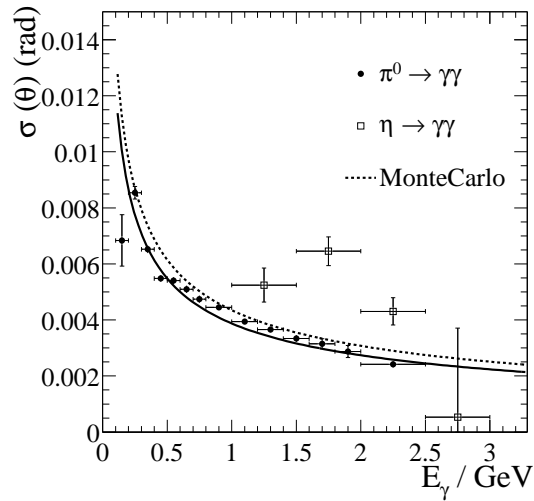
(b)

Figure 3.15: *(a) Energy resolution versus energy photon for different calibrations. (b) Angular resolution versus energy photon.*
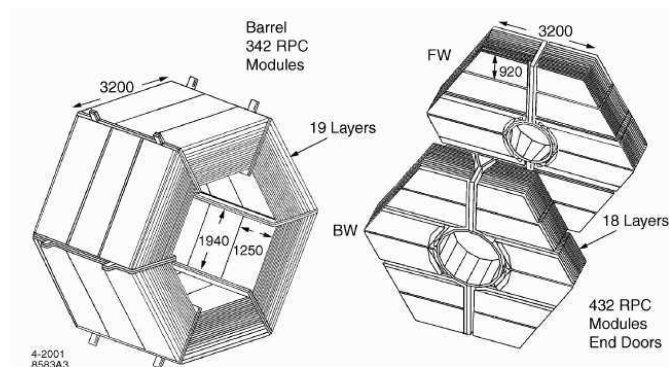
Figure 3.16: *Drawing of the IFR barrel and endcaps*

3.6 Instrumented flux return

The IFR is the primary muon detector at *BABAR* and is also used for the identification of long-lived neutral hadrons (primarily K_L^0's). The IFR is divided into a hexagonal barrel, which covers 50% of the solid-angle in the CM frame, and two endcaps (Fig. 3.16). Originally, it consisted of layers of steel of varying thickness interspersed with Resistive Plate Chambers (RPCs), 19 layers in the barrel and 18 in each endcap. The steel serves as a flux return for the soledail magnet as well as an hadron absorber, limiting pion contamination in muon ID. RPC's were chosen as they were believed to be a reliable, inexpensive option to cover the 2000 m^2 of instrumented area in this outermost region of *BABAR* with the desired acceptance, efficiency, and background rejection for muons down to momenta of 1 GeV/c.

The RPC's detect high-energy particles through gas-avalanche formation in a high electric field. The chambers consist of 2mm-thin bakelite sheet kept 2 mm apart by an array of spacers located every 10 cm (Fig 3.17). The space in between is filled with a non-flammable gas mixture of 56.7% argon, 38.8% freon 134a, and 4.5% isobutane, while the sheets are held at a potential of 8000 V. The inside surface of the bakelite is smoothed with a linseed-oil coating so that the electric field is uniform, thus preventing discharges in the gas and large dark currents. The RPC's operate in streamer mode, wherein the avalanche grows into a streamer, a mild, controlled form of electrical discharge in the gas. The streamer change is read out in both the ϕ and z directions by aluminum strips located outside and capacitively coupled to the chamber. The streamer is kept from producing electrical breakdown of the gas by the quenching action of the freon and isobutane molecules. Isobutane has large molecules with rotational degrees of freedom that can

absorb electrical energy.

In streamer mode, the gas gain is at the 10^8 level. The factor of 10-1000 increase in gain over avalanche mode greatly simplifies the readout electronics. Moreover, the charge of the streamer is independent of the primary-ionization charge, resulting in an effectively digital signal with high efficiency . Initially, the RPCs performed at over 90% efficiency as expected geometrically from inactive space in the detector, resulting in a muon detection efficiency of 90% for a pion misidentification rate of 6-8% in the momentum range of $1.5 < p < 3.0$ GeV/c.

Shortly after the start of data-taking with BABAR in 1999, the performance of the RPCs started to deteriorate rapidly. Numerous chambers began drawing dark currents and develop large areas of low efficiency. The overall efficiency of the RPC's started to drop and the number of non-functional chambers (with efficiency less than 10%) rose dramatically (Fig. 3.18), deteriorating muon ID. The problem was traced to insufficient curing on R&D of the linseed-oil-coating and to the high temperature at which the RPC's were operated initially. Uncured oil droplets would form columns under the action of the strong electric field and the high temperature (up to 37 °C), bridging the bakelite gap and resulting in large currents and dead space (Fig. 3.19)

Various remediation measures were attempted, including flowing oxygen through the chambers to cure the oil and introducing water cooling on IFR, but they did not solve the problem. Extrapolating the efficiency trend showed a clear path towards muon ID capability at BABAR within a couple of years
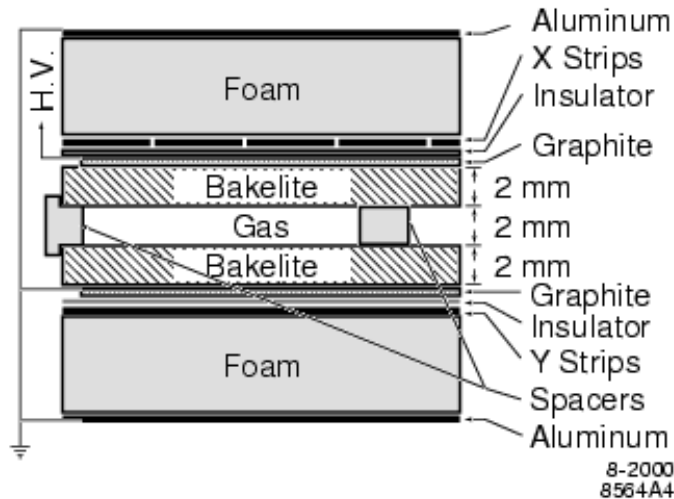
Figure 3.17: *Front section of BABAR RPC*

60
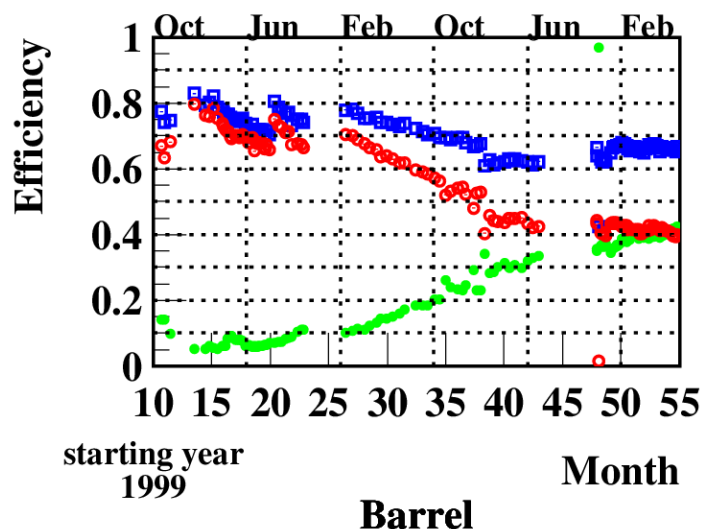
Figure 3.18: *Deterioration with time of the average RPC efficiency (red). The green dots show the fraction of RPC's with efficiency lower than 10 %, and the blue dots show the fraction of RPC's with efficiency greater than 10%.*

of operations, so an upgrade of the IFR detector was deemed necessary by the collaboration.

Figure 3.19: *Photographs of defects on the linseed oil coating of a malfunctioning RPC.*

The forward endcap was retrofitted with new improved RPCs in 2002. The new chambers were screened much more stringently with QC test and had a much thinner linseed-oil coating that was properly cured and tested. They have performed well since then. The backward endcap wasn't retrofitted, as its acceptance in the CM frame is small. In the barrel, the collaboration decided to upgrade the detector with *Limited Streamer Tube* (LST) technology. The RPCs were removed and replaced by 12 layers of LSTs and 6 layers of brass to improve hadron absorption. Notice that the last layer of RPCs

61

is inaccessible, so the old chamber there were disconnected from all utilities but kept in place. As the author was involved in this upgrade and as the project was a laborious and careful but time-sensitive project undertaken at a mature age of the experiment, it will be described in more detail than the other components of the detector. The LST consist of a PVC comb of eight 15 mm by 17 mm cells about 3.5 m in length, encase in a PVC sleeve, with a 100 μm gold-plated beryllium-copper wire running down the center of each cell (Fig. 3.20). The cells in the comb are covered with graphite, which is grounded, while the wires are held at 5500 V and held in place by wire holders located every 50 cm.

Figure 3.20: *The mechanical structure of a BABAR LST.*

The gas mixture consist of 3.5 % argon, 8% isobutane, and 88.5 % carbon dioxide. Like the RPCs and as their name implies, the LSTs are operated in streamer mode. The signal is read off directly from the wires through AC-coupled electronics (granularity of two wires per channel in the ϕ direction) and from strips running perpendicular to the tubes and capacitively coupled to the wires (35mm pith in the z direction).
Experience with the RPCs underscored the crucial role of R&D and QC at every level of development of the new technology. Thus, during R&D a stringent QC methodology was developed after the final design of the tubes was chosen. During construction, the mechanical quality of the graphite surface was inspected and the resistivity tested. The chambers were strung with wires tested for thickness and tested for gas leaks after sealing. The tubes were then conditioned under progressively higher applied voltage to burn off any dirt accumulated during construction. Only tubes that could hold the operational voltage without drawing excessive currents were accepted. One of the crucial performance characteristics was the "singles' rate", or counting-rate, plateau. As the streamer signals are effectively digital, given a constant incident flux of particles, the chamber should show a counting-rate plateau

over a range of applied voltage where the charge of every streamer is above the read-out threshold (Fig. 3.21).

The plateau provides operational tolerance of the applied HV, allowing operations of the LSTs at the middle of the plateau to safeguard against fluctuations in efficiency due to changes in the gas gain from pressure or voltage fluctuations. Defects in the surface of the graphite or dirt accumulated on the wire can result in large discharges in the tube that raise the singles' rate and spoil the plateau, as visible in Fig. 3.21. In addition, a short plateau is an indication of poor aging behavior. Thus, the quality of the plateau is a powerful QC test. [3]
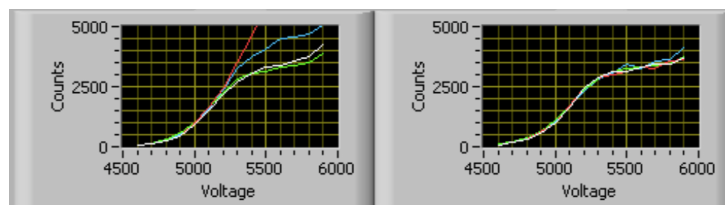
Figure 3.21: *A singles' rate plateau seen versus applied voltage for several LST channels (right). Defects in the chamber can spoil the plateau (left)*

Another powerful QC procedure is scanning the tube with a localized, focused radioactive source, subjecting small regions of the tube to intense radiation rates. Although the incident flux is then much higher than what the tube would experience in the experiment, the stress reveal weak points in the tube, where the source initiates a self-substaining discharge of high current that continues even when the source is removed while the high voltage is applied (Fig 3.22) [4]. Only tubes that do not exhibit this behavior are accepted for installation.

The LSTs were constructed at Pol.Hi.Tech., an Italian company that was located in Carsoli, outside of Rome. The construction and QC procedures outlined above were conducted under the supervision of *BABAR* personnel. After all QC tests, the tubes were held under high voltage for a month to verify that no premature aging behavior occurred. Thereafter, they were

---

[3]The plateau eventually fails at 5900V or higher due to multiple streamers formed from electrons photoelectrically ejected from the graphite by UV photons radiated by the original streamer. At high voltages, enough UV photons are produced to overwhelm any signal dead-time imposed by the electronics, thus raising the singles' rate.

[4]This happens when a conductive channel is formed in the gas around a mechanical defect.
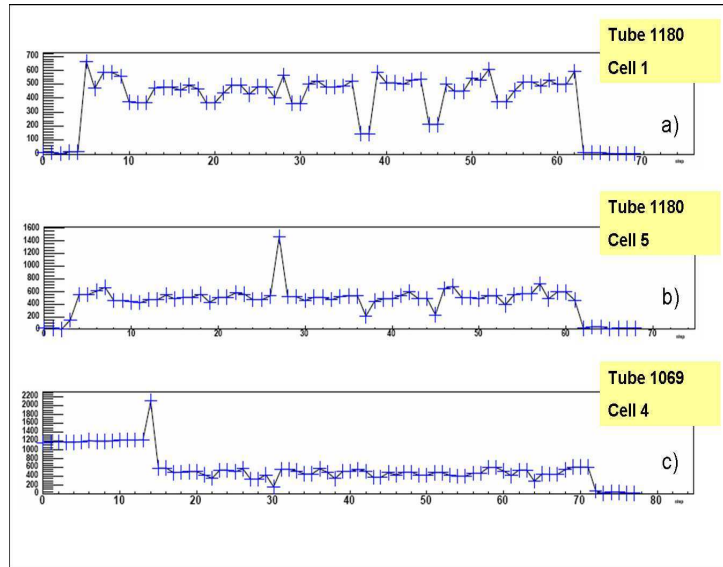
Figure 3.22: *Plots of the current drawn by an LST versus position of the source as it scan along the length of the chamber. Channel without any problem (top). Channel with a spike (center). Channel with a self-substaining discharge (bottom).*

assembled into modules of two to three tubes at Princeton University and at Ohio State University and then shipped to SLAC for installation, which occurred in two stages: two sextants of hexagonal barrel in the Summer 2004 and the remaining in the Fall of 2006 [5]. QC procedures were performed at every step to make sure that only the best tubes were installed in the detector.

The project involved the manufacture of 1500 LSTs including contingency, with more than 1200 installed in the detector. It also necessitated the design and fabrication of custom read-out electronics, HV power supplies and gas system. The project was completed successfully, safely, and ahead of schedule. After installation, the tubes have been performed extremely well since 2005 in two sextants and since the beginning of 2007 in all sextants, with failures rates below 0.5% for both the tubes and z-strip. The efficiencies of all layers are at the geometrically expected level of 90%. Regular testing of singles' rates with cosmic rays has verified continuing excellent behavior with long singles'-rate plateau.

Fig. 3.23 shows muon tracks in the LST part of the IFR.

---

[5]The delay of the second phase was due to an electrical accident at SLAC in the Fall of 2004 that shut down the lab for a half of a year.
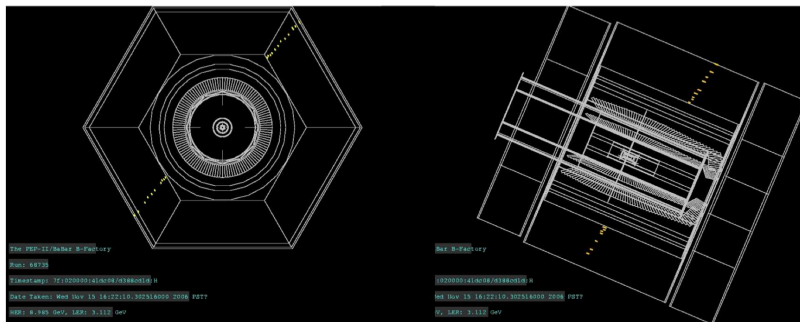
Figure 3.23: *Cosmic -ray muon ϕ view (left) and z view (right)*

3.7 Trigger, Data Acquisition and Reconstruction

Data relevant for B physics is selected for storage from the flow of collision information collected by the detector by a two-level trigger system. The Level 1 (L1) trigger is hardware-based, consisting of several dedicated microprocessor systems that analyze data from the front-end electronics (FEEs) of the DCH, EMC, and IFR to form primitive physics object used to make the trigger decision. These include tracks of minimum transverse momentum that penetrate to a particular depth into the DCH and energy clusters in the EMC above the thresholds. The selection are optimized to maintain nearly $B\overline{B}$ efficiency while removing most of the beam-induced backgrounds in the process of reducing the data collection rate from about 20kHz to a few kHz, which can be processed by the next trigger level. Some "prescaled" events of random bem-beam crossing and special events types are also collected for efficiency, diagnostic, and background studies. The trigger decision is made and communicated within the 12.8 μs buffer limit of the FEEs. The L1 trigger has greater than 99.5% efficiency for $B\overline{B}$ processes.

After an L1 accept decision, the L1 output is passed on to the Level 3 (L3) trigger, which consists of software-based algorithms run on a farm of commercial PCs.[6] The L3 trigger also has access to the complete event data and refines the L1 decision with more sophisticated selections, such as requirements on a track's distance of closest approach to the interaction point or the total invariant mass of an event. It maintains the $B\overline{B}$ selection efficiency at more than 99% while reducing the data rate to about 200Hz. Each event corresponds to about 30kB of detector information.

An event that results in an L3 accept decision is processed by the data-acquisition electronics and event-building software. In this process, charged tracks are reconstructed from DCH and SVT information and extrapolated to the outer part of the detector incorporating knowledge of the distribution of material in the detector and magnetic field. The momenta of tracks is measured from the sagitta in the curves of the tracks [7]. PID is refined with DIRC, EMC, and IFR information as well as with attempts to match

---

[6]The numbering scheme is historical and based on trigger systems with two-hardaware based levels and a third, software-base level, as commonly implemented in hadron colliders. BABAR requires only one hardware-based level, but the first software-based level maintains the tertiary designation.

[7]Charged particles are deflected by the magnetic field of the solenoidal and propagate in helices around the magnetic field lines with the radius of curvature $R \sim p/B$, where p is the momentum of the particle and B is the magnetic field. The orientation of bending depends on the charge of the particle

objects in those sub-detectors with tracks in the DCH. Fundamental physical objects reconstructed in the detectors are also used to assemble candidates for composite particles, such as π^0's from two photon candidates and K_S^0's from two charged tracks candidates (from the $K_S^0 \to \pi^+\pi^-$ process.) List of particle candidates as well as the original digitized data is stored on tape in collections that are retrieved later for high-level analysis by individual groups of users.

Throughout event reconstruction various calibration such as alignment constants and energy-scale adjustments in the EMC are applied to detector information to refine reconstruction performance. Calibration information were updated frequently during data taking to keep it consistent with running conditions. Data-quality scripts monitor detector behavior and various physics processes to verify that the collected data was not compromised by deviations from expected behavior of the detector or accelerator. A parallel system based on the EPICS slow-control environment was used to monitor and control the detector elements for all subsystems. Detector, accelerator, and environmental conditions were recorded in another ambient database. The entire data-taking process was supervised at all times by at least two BABAR shifters on the detector side and several accelerator operators on the PEP-II side.

Chapter 4

Analysis

4.1 Analysis strategy

In the search for $e^+e^- \to c\bar{c}c\bar{c}$ events, a J/ψ is fully reconstructed. For the quantum numbers available one can reconstruct also a $\psi(2S)$, but this channel is not studied here. The charmonium formed by the other $c\bar{c}$ pair in the event is indirectly detected by way of the recoil mass against the fully reconstructed J/ψ. Explicitly, the recoil mass, M_{rec}, is determined via

$$M_{rec} = \sqrt{(\sqrt{s} - E_\psi^*)^2 - p_\psi^{*2}} \tag{4.1}$$

where $\sqrt{s}$ is the Center of Mass (CM) energy of the e^+e^-, and E_ψ^* and p_ψ^* are the energy and momentum of the J/ψ or $\psi(2S)$ in the CM system, respectively.

In order to improve the resolution of the recoil mass, a kinematic fit with a 'geometric' constraint and a mass constraint to the mass of J/ψ is applied.

After performing the selection and obtaining the M_{rec} distribution, enhancements in this distribution are studied in this analysis.

The analysis is performed blind, that is by determining the event selection without looking at the data in the interested window $(2.5 - 4.0\,\mathrm{GeV}/c^2$ in the recoil mass).

4.2 Data samples and preselection

4.2.1 Data processing in *BABAR*

The quality of data collected by the *BABAR* detector is checked online by the shifter on duty who discards the samples affected by sub-detectors bad performance or unacceptably high backgrounds.

The raw data undergo then the *prompt calibration* and *event reconstruction* stages. At the beginning all calibration parameters and alignments, which can vary over the time, are updated; this phase is done by SLAC's computing resources within a few hours from the data taking. In the latter, charged tracks and neutral particles are reconstructed from the single hits and energy deposits in each subdetector: this is performed at the dedicated processing farm in Padova (Italy), within the following 48 hours.

After the final validation, the data are subdivided into smaller samples (skims) which satisfy the needs of the main branches of physical analysis and are distributed over the computing facilities dedicated to data analysis.

4.2.2 Data and Montecarlo samples

Data samples

This current analysis is based on an amount of 467.8 fb^{-1} *BABAR* data, collected from February 2000 to August 2007, during the data-taking periods Run1-Run6. This sample includes about $423.7fb^{-1}$ taken at the Y(4S) resonance (on-peak) and $44.1fb^{-1}$ taken off-peak, at 40 MeV below.

The data used in this analysis come from a skim, named *JpsitollTight*, where the events contains a J/ψ, reconstructed by its decay in e^+e^- or $\mu^+\mu^-$, with the following remarks.

In the case of $\mathbf{J}/\psi \rightarrow \mathbf{e^+e^-}$, the requests are:

- the two electrons are selected by a PID selector, named `eLHBremLH` in the *BABAR* PID framework, which is a merged list containing combination of a Bremsstrahlung-recovered electron and an other electron that did not undergo Bremsstrahlung. The algorithm checks to make sure that candidates are counted only once. The bremsstrahlung-recovered electron is moreover an electron $e \rightarrow e\gamma(\gamma\gamma)$, selected during the ordinary PID selection, associated to a photon of an energy 0.030 to 10.58 GeV, a lateral energy distribution 0.0001 to 0.8 GeV, and a Zernike moment higher than 0.25. In addition electron and γ('s) point in the same direction, based on polar and azimuthal angles cuts;

- the invariant mass reconstructed by the electron must be 2.5 GeV $<$ m(e^+e^-) $<$ 3.3 GeV.

Instead for the candidates $\mathbf{J}/\psi \rightarrow \mu^+\mu^-$, it's requested that:

- the two muons come from the PID list `muNNVeryLoose`, which is based on the use of the Neural Network (NN) technique;

Data set	On-Peak data $\mathcal{L}$ (fb^{-1})	On-Peak data Number of Events	Off-Peak data $\mathcal{L}$ (fb^{-1})	Off-Peak data Number of Events
Run1	20.0	2563924	2.6	317464
Run2	61.1	7420029	6.9	800599
Run3	32.3	4038450	2.5	298291
Run4	100.3	14611850	10.2	1372083
Run5	133.3	18874250	14.6	1900141
Run6	76.7	10485685	7.3	925277
Total	423.7	57994188	44.1	5613855

Table 4.1: *On-peak and off-peak data collections used in the analysis: in total 467.8 fb^{-1}.*

- the invariant mass is in the range 2.8 GeV $<$ m($\mu^+\mu^-$) $<$ 3.3 GeV.

Details on data samples are summarized in table 4.1

Reconstruction of the J/ψ

During the n-tuples production phase, further requests have been done for the reconstruction of the J/ψ. A *geometric* fitter fits both position and momentum information, whereas a *kinematic* fitter extracts only momenta: in particular, in this analysis the so-called *Cascade* geometric fitter has been used, which implements a χ^2-minimization process to perform vertex-position and momentum fits: it is leaf-by-leaf fitter that uses Newton-Raphson method [52].

Montecarlo samples

This analysis has been set up using Montecarlo samples of the signal $e^+e^- \rightarrow J/\psi\,c\bar{c}$, where $e^+e^- \rightarrow J/\psi\,\eta_c$, $J/\psi\,\chi_{c0}$, $J/\psi\,\eta_c(2S)$ and J/ψ X(3940) channels are defined. For the first three modes, 35k events are generated, while for the last 175k events, due to technical reasons of Montecarlo production. In table 4.2, the number of events fro each channel is summarized.

Also in the Montecarlo generation, the J/ψ decays into either e^+e^- or $\mu^+\mu^-$.

4.2.3   Background

As the aim of this analysis consists to study the spectrum recoiling against a reconstructed J/ψ, the Montecarlo is composed mainly by not good J/ψ.

Decay	Number of Events
$e^+e^- \to J/\psi\,\eta_c$	35000
$e^+e^- \to J/\psi\,\chi_{c1}$	35000
$e^+e^- \to J/\psi\,\eta_c(2S)$	35000
$e^+e^- \to J/\psi\,X(3940)$	175000
$e^+e^- \to J/\psi\,c\bar{c}$	280000

Table 4.2: *Summary of Montecarlo channels used in this analysis, and the corresponding number of events generated.*

In particular, to study the background in the recoil system, sidebands in the J/ψ mass distribution have been taken, i.e. data events which are in the following ranges:

- for muons $|m(\mu^+\mu^-) - 3.097\,\mathrm{GeV}/c^2| > 0.060\,\mathrm{GeV}/c^2$;

- for electrons $(m(e^+e^-) - 3.097\,\mathrm{GeV}/c^2) > 0.060\,\mathrm{GeV}/c^2$ and $(m(e^+e^-) - 3.097\,\mathrm{GeV}/c^2) < -0.080\,\mathrm{GeV}/c^2$.

The choice of these sidebands is due to the asymmetric distribution of the mass of the J/ψ in the signal MC (see figure 4.1). In spite of the Bremsstrahlung effect recovery required for one of the two electrons, notice that the distribution of the J/ψ mass in the electronic case has a !!!!coda!!!!! for low values, due actually to this effect.

4.3   Selection strategy

The general procedure of selection is composed by two main steps: preselection and selection. In the preselection phase, cuts are based on physics remarks on the involved process. So this first step is simple cut-based (see section 4.4). In the second part, in addition to rectangular cuts (on the momentum and the number of charged tracks), also a multi-variate analysis will be used, to take into account of other four variables (section 4.6). This approach is aimed to maximize the figure of merite $S/\sqrt{S+B}$, called S and B the signal and background samples.

4.4   Preselection

During the production of the n-tuples a primary selection has been carried out, doing the following requests:
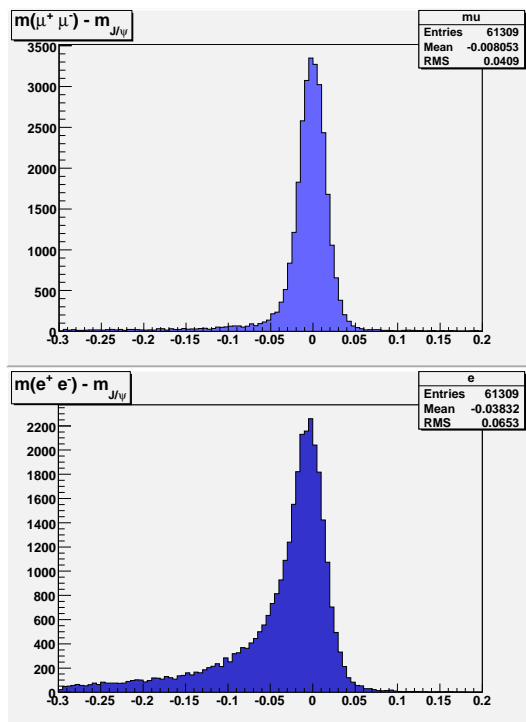
Figure 4.1: *Distribution of the J/ψ mass in the signal MC, for J/ψ → e⁺e⁻ and J/ψ → μ⁺μ⁻ respectively.*

- post fit selection for the J/ψ mass (2.8 GeV $< mass_{J/\psi} <$ 3.3 GeV);

- post fit selection for chi-squared probability (0.001 $< prob_{\chi^2} <$ 1.000) for the J/ψ vertex reconstruction;

In table 4.3 see the effect of the preselection procedure: for each run the number of events before and after the preselection, and the survival rate. Almost half of the skimmed events are removed after this point.

Figure 4.4 shows the distributions of the di-lepton mass minus the nominal J/ψ mass (3.097 GeV/c^2), noted as $\Delta M_{J/\psi}$, for e^+e^- and $\mu^+\mu^-$. In these distributions we made the cuts described above. In order to perform the fit of these distributions, we used a Crystal Ball function plus a 2nd order polynomial.

73

Run	#events before	#events after	survival rate ϵ
Run1 on-peak	2563924	1367101	53%
Run2 on-peak	7420029	4095185	55%
Run3 on-peak	4038450	2170905	54%
Run4 on-peak	14611850	8531505	58%
Run5 on-peak	18874250	10928793	58%
Run6 on-peak	10485685	5956077	57%
Total off-peak	5613855	3125136	56%

Table 4.3: *Surviving events number in the preselection. "Before" means the number of events from the skim JpsiTollTight collections, before the n-tuple production. "After" means the number of events after the preselection cuts and the n-tuple production.*

4.5   Selection cuts

4.5.1   Number of charged tracks

A remarkable variable is the number of charged tracks in the event, called $NTRK$. The plot in figure 4.2 shows the distribution of $NTRK$ in the signal MC (blue), and the sidebands background in the data (red): these two distributions are overlapped and normalised. It's possible to remove background by selecting events with at least 4 charged tracks. A part of signal events have $NTRK = 3$ and $NTRK = 4$, and a dedicated study was performed for each of these sample. Signal and background are calculated as the number of events under the respectively the Crystal Ball function (fitting the J/ψ mass) and the linear function (fitting the total background) in the window of $\pm 50 MeV$ centered in the nominal mass of the J/ψ.

The J/ψ mass peak for $NTRK = 3$ and $NTRK = 4$ have a signal-to-background ratio respectively $S/B \simeq 0.08$ and $S/B \simeq 0.13$, which are too poor to be included in the final signal sample (see figure 4.3)..

Sample	S	B	$\frac{S}{B}$
NTRK = 3	30301	363272	0.08
NTRK = 4	31939.9	236601	0.13
NTRK > 4	12760	47634	0.27

Table 4.4: *Signal and background events for the samples of events with $NTRK = 3$, $NTRK = 4$ and $NTRK > 4$.*

Figure 4.4 shows the distributions of the di-lepton mass minus the nominal J/ψ mass ($3.097 \, \text{GeV}/c^2$), noted as $\Delta M_{J/\psi}$, for e^+e^- and $\mu^+\mu^-$. In these distributions we made the preselection cuts plus the cut on the charged tracks.
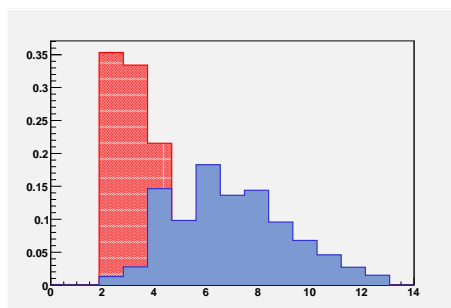
Figure 4.2: *Distributions of the number of charged tracks.*
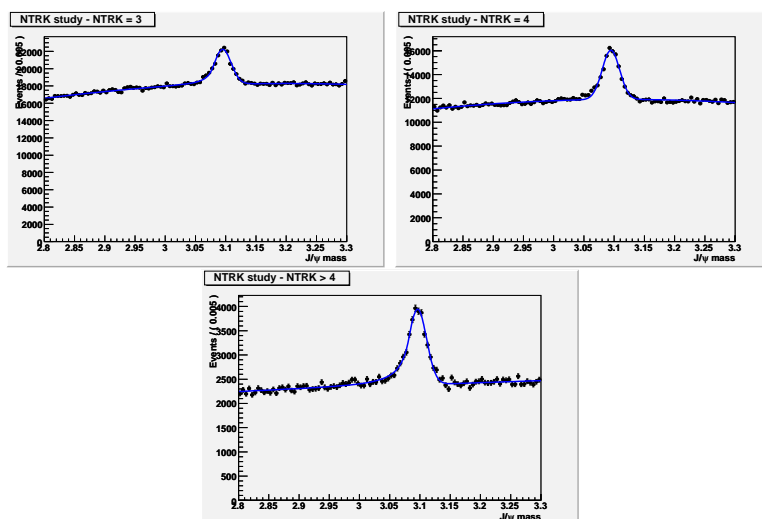
Figure 4.3: *J/ψ mass distributions respectively in the case NTRK = 3, NTRK = 4 and NTRK > 4, in the full data.*

In order to perform the fit of these distributions, we used a Crystal Ball function plus a 2nd order polynomial. This cut substantially suppresses QED processes.

4.5.2 Momentum of the J/ψ in the CM frame

An other important variable to take into account is the J/ψ momentum in the CM frame $p^*_{J/\psi}$. We will cut events with $p^*_{J/\psi}$ lower than 2.0 GeV/c, in order to remove those J/ψ from B meson decays, corresponding to a recoil mass above 6.6 GeV/c^2; figure 4.5 shows the $p^*_{J/\psi}$ distribution for signal,
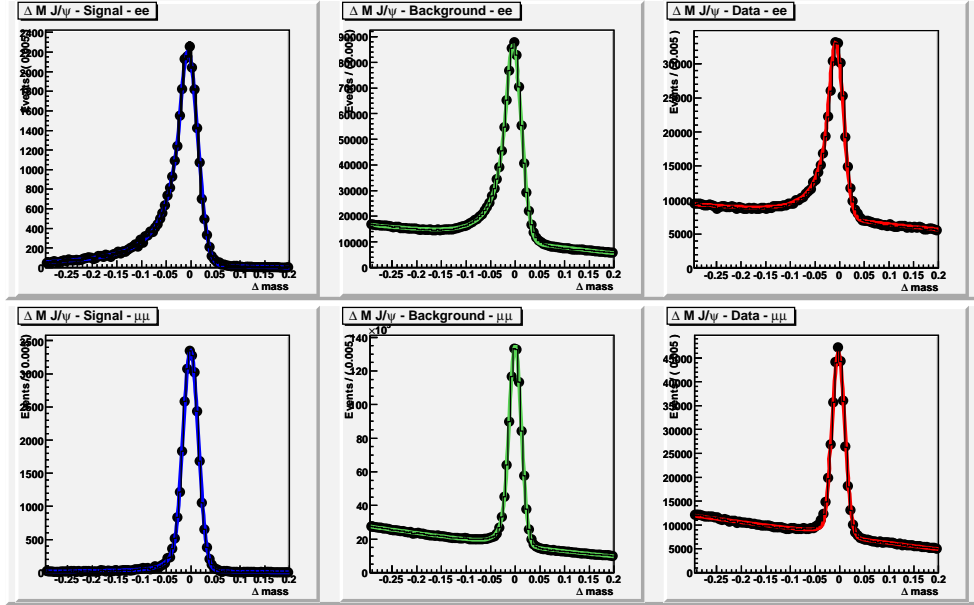
Figure 4.4: *Distributions of the $m(e^+e^-) - m_{J/\psi}$ (above) and $m(\mu^+\mu^-) - m_{J/\psi}$ (below), respectively for the signal MC, the background MC (udsc, $B\bar{B}$, $B_0\bar{B}_0$ together) and the full data.*

background and full data. Cutting $p^*_{J/\psi}$ at 2.0 GeV/c, it's possible to remove a large number of background events.
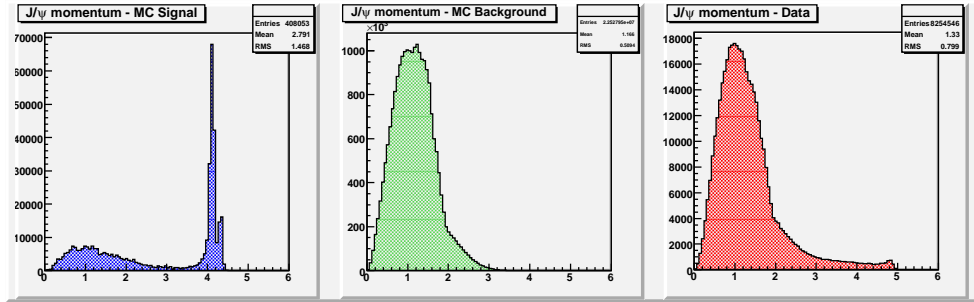
Figure 4.5: *Distributions of the $p^*_{J/\psi}$ respectively for the signal MC, the background MC (udsc, $B\bar{B}$, $B_0\bar{B}_0$ together) and the full data*

It's interesting to see the effect of this cut in the $m_{J/\psi}$ distributions (see figure 4.6), to compare with figure 4.4.
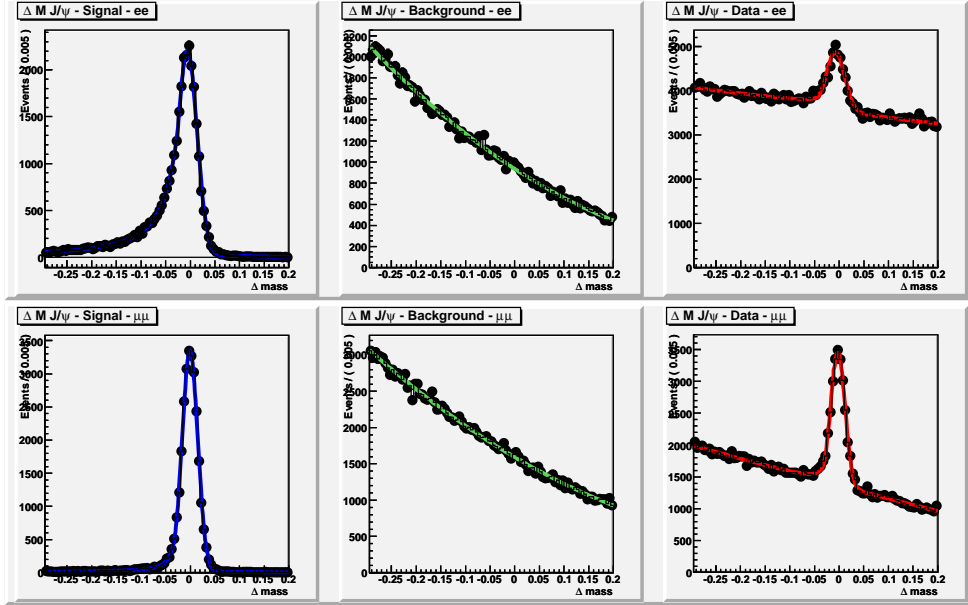
Figure 4.6: *Distributions of the $m(e^+e^-)-m_{J/\psi}$ (above) and $m(\mu^+\mu^-)-m_{J/\psi}$ (below), respectively for the signal MC, the background MC (udsc, $B\bar{B}$, B_0B_0 together) and the full data, after the cut $p^*_{J/\psi} < 2.0 GeV/c$.*

4.6 Multivariate Analysis (MVA)

4.6.1 Principle of the MVA

Multivariate analysis refers to any statistical technique used to analyse data, which involves observation and analysis of more than one statistical variable at a time. This essentially models reality where each situation, product, or decision involves more than a single variable. The information age has resulted in masses of data in every field. Despite the quantum of data available, the ability to obtain a clear picture of what is going on and make intelligent decisions is a challenge. When available information is stored in database tables containing rows and columns, Multivariate Analysis can be used to process the information in a meaningful fashion. Multivariate classification methods based on machine learning techniques are fundamental ingredient to most analyses.In this way, several multivariate classification algorithms exist and range from rectangular cut optimization using a genetic algorithm and from one and multidimensional likelihood estimators, over linear and nonlinear discriminants and neural networks, to sophisticated more recent classifiers such as a support vector machine, boosted decision trees and rule

77

ensemble fitting.

In this analysis the MVA classifier is a Neural-Network based algorithm, named multi-layer perceptron, that will be described in detail in the next section.

4.6.2 Application

After the application of the cuts on the number of the tracks ($NTRK > 4$), on the momentum of J/ψ ($p^*_{J/\psi} > 2\,\text{GeV}/c$) and on the recoil mass distribution ($2.0 < M_{rec} < 4.3\,\text{GeV}/c^2$), we used the Toolkit for Multi-Variate Analysis (TMVA) [53] in order to manage the following further discriminating variables:

Fox-Wolfram moment R_2
   This variable gives information on the shape of the decay [54]. The Fox-Wolfram moments H_ℓ are defined as:

$$H_\ell = \sum_{i,j} \frac{|p_i||p_j|}{E_{vis}^2} P_\ell(cos\theta_{ij}) \qquad (4.2)$$

   where θ_{ij} is the angle between the particle momenta $\mathbf{p_i}$ and $\mathbf{p_j}$ and E_{vis} is the total visible energy of the event. The $P_\ell(x)$ are the Legendre polynomials, i.e. $P_0(x) = 1, P_1(x) = x$,. Energy-momentum conservation requires that $H_0 \simeq 1$ and $H_1 = 0$ if we assume negligible contributions from particle masses. It is therefore customary to normalize the results to H_0 and we define the second Fox-Wolfram moment as:

$$R_2 = \frac{H_2}{H_0}. \qquad (4.3)$$

   The highly directional continuum events tend to have high R_2-values whereas the more spherical events have lower values of R_2.

Probability of the reconstruction of the J/ψ vertex χ^2
   The probability of the J/ψ vertex reconstruction expressed as χ^2 of the vertex fit.

$\cos\theta(\mathbf{J/\psi})$
   It is the cosine of the angle between the J/ψ momentum and the z direction in the center of mass (CM) frame.

J/ψ **helicity**

It is the cosine of the helicity angle of the J/ψ decay, which is the angle between the J/ψ momentum direction in the J/ψ rest frame and the J/ψ momentum direction in the CM frame.

In figures 4.7 and 4.8 there are the distributions of these variables.

1000 MC signal events inside the ranges defined for the sidebands and 5000 events of the sidebands (for muons $|m(\mu^+\mu^-)-3.097\,\text{GeV}/c^2| > 0.060\,\text{GeV}/c^2$, for electrons $(m(e^+e^-) - 3.097\,\text{GeV}/c^2) > 0.060\,\text{GeV}/c^2$ and $(m(e^+e^-) - 3.097\,\text{GeV}/c^2) < -0.080\,\text{GeV}/c^2)$ of the J/ψ mass distribution are used as signal and background training samples, respectively, in TMVA.

In blue you see the signal dataset, which consists in the produced signal MC, as described in section 4.2.2, with the following cuts:

- only events inside the range of the sidebands (for muons $|m(\mu^+\mu^-) - 3.097\,\text{GeV}/c^2| > 0.060\,\text{GeV}/c^2$, for electrons $(m(e^+e^-)-3.097\,\text{GeV}/c^2) > 0.060\,\text{GeV}/c^2$ and $(m(e^+e^-) - 3.097\,\text{GeV}/c^2) < -0.080\,\text{GeV}/c^2)$;

- at least 5 charged tracks in the events, as discussed in 4.5;

- the mass recoiling against the J/ψ, not calculated with the J/ψ mass constraint, is included between 2.0 and 4.3 GeV/c^2.

- $p^*_{J/\psi}$ greater than 2.0 GeV/c, as discussed in 4.5.2.

In red there's the background sample: it is taken from the data and it is correspondent to the sidebands of $m_{J/\psi}$. So the cuts performed in the background sample are the same as above except for the first point, where the cuts are opposite. Notice that, as in this analysis the signal in a specific region of the recoil side is investigated, we will take into account from now also the following rectangular cut: $2.0\,\text{GeV}/c^2 < M_{rec} < 4.3\,\text{GeV}/c^2$, where M_{rec} is the mass recoilng against the J/ψ, reconstructed without J/ψ mass constraint. Taking a look at the distributions in figures 4.7 and 4.8 one could make rectangular cuts on R_2, $cos\theta(J/\psi)$ and J/ψ helicity. Anyway, with the Multi-Variate analysis we can take under consideration every variable and directly cut on the best classifier on the point that maximizes the significance. This Multi-Variate analysis has been performed with the TMVA package [53], which provides training, testing and performance evaluation algorithms and visualization scripts.

The training has been done with six kinds of classifier, in order to verify the best one: finally MLP (multi-layer perceptron) was chosen, based on the best background rejection versus signal efficiency (Fig. 4.9).
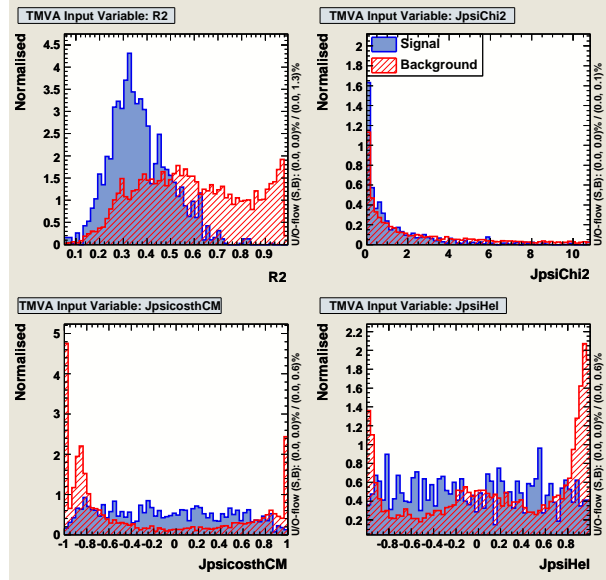
Figure 4.7: *Distributions of the variables taken into account to perform cutsfor the events with J/ψ decays to e^+e^-.*
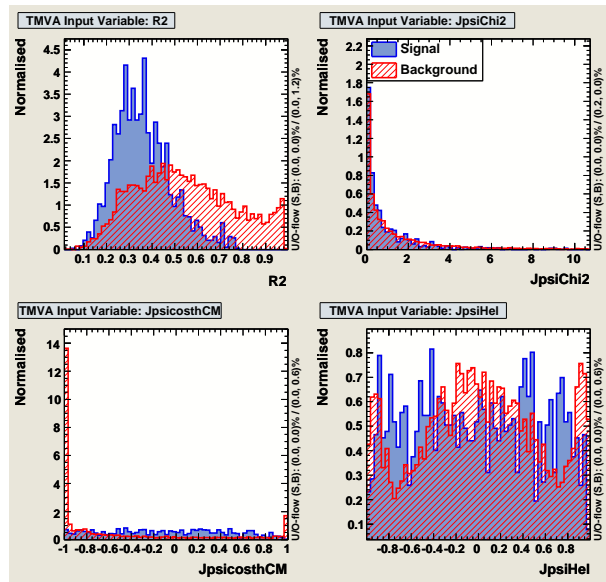
Figure 4.8: *Distributions of the variables taken into account to perform cuts for the events with J/ψ decays to $\mu^+\mu^-$.*

80
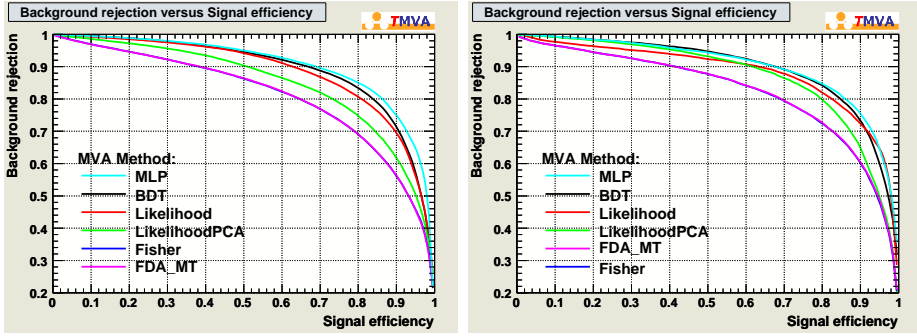
Figure 4.9: *Background rejection versus signal efficiency for all classifiers: it is clear from this plot the reason why MLP was chosen.*
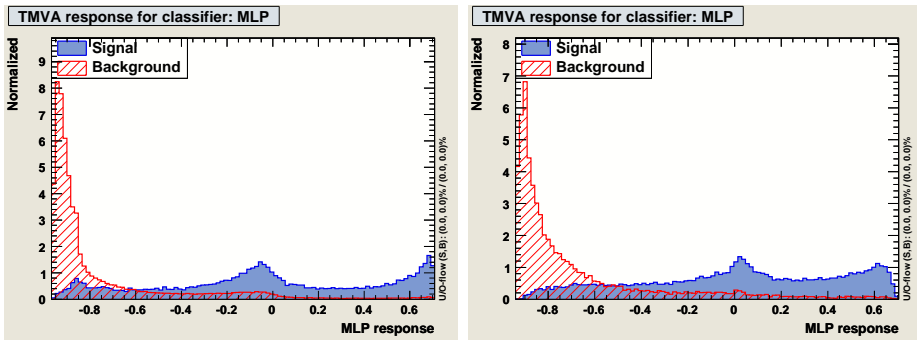
Figure 4.10: *The MLP distribution for signal and background, respectively for e^+e^- and $\mu^+\mu^-$ samples.*

Multi-layer perceptron

The multi-layer perceptron neural network model consists of a network of processing elements or nodes arranged in layers. While in principle a neural network with n neurons can have n^2 directional connections, the complexity can be reduced by organizing the neurons in layers and only allowing directional connections from one layer to the immediate next one.

The first layer of a MLP is the input layer, the last one the output layer, and all others are hidden layers. For a classification problem with n_{var} input variables and 2 output classes the input layer consists of n_{var} neurons that hold the input values, $x_1, ..., x_{nvar}$, and one neuron in the output layer that holds the output variable, the neural net estimator y_{ANN}. Each directional connection between the output of one neuron and the input of another has an associated weight. The value of the output neuron is multiplied with the weight to be used as input value for the next neuron.

Results of the MVA application

As visible in figures 4.11 and 4.12, the variables under consideration are not correlated, so that a multi variate analysis can be performed with good results.
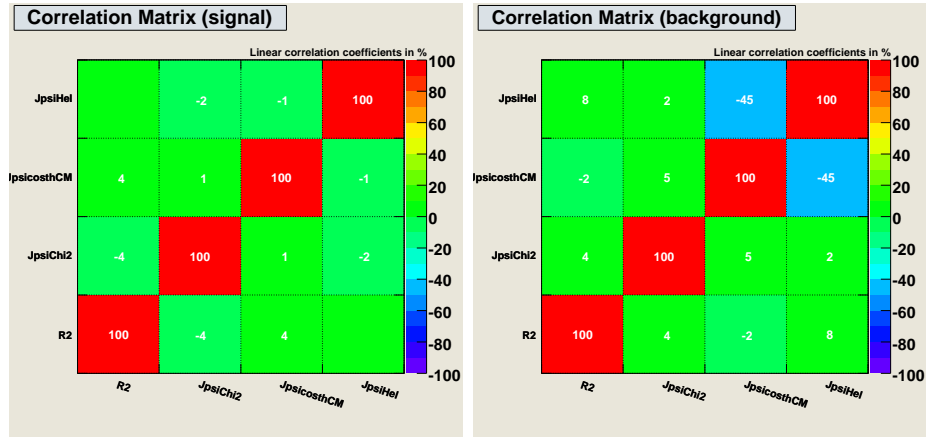
Figure 4.11: *Correlation matrix for signal and background for the sample with $J/\psi \to e^+ e^-$.*

So a big amount of background is removed by applying the cut on the MLP classifier, which combines the discriminating variables already mentioned. As said at the beginning of the section, the choice of the cut on MLP variable was aimed at maximizing the figure of merit $S/\sqrt{S + B}$, where S
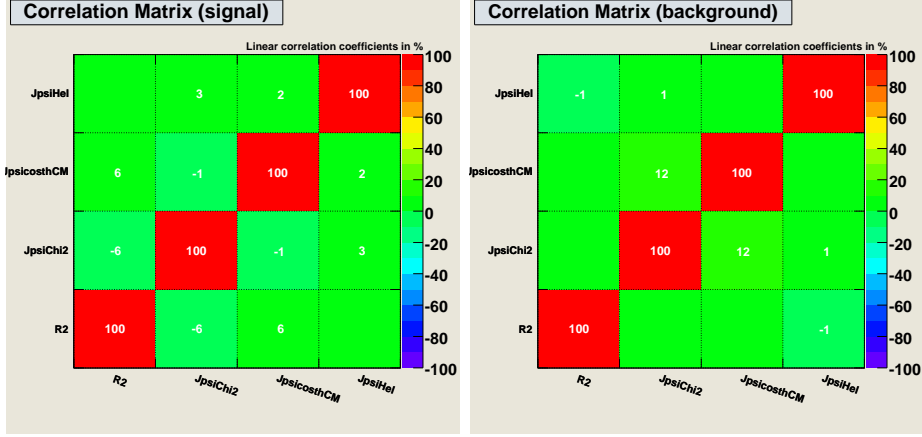
Figure 4.12: *Correlation matrix for signal and background for the sample with* $J/\psi \rightarrow \mu^+\mu^-$.

and B represent the number of signal and background events, in the window under the J/ψ mass peak. In the next section, there will be described the procedure in order to calculate S and B.

4.6.3 Calculation of $N_{S_{exp}}$ and $N_{B_{exp}}$

When MVA Toolkit runs, it gives by default a best values of the classifier (MLP in this case), normalized to a default number of 1000 events of signal (S) and 1000 events of background (B). But the ratio, or in general a relationship, between S and B depends strongly on the number of signal and background. So it is necessary to know exactly how many events we expect for signal and background. In this section it's explained how $N_{S_{exp}}$ and $N_{B_{exp}}$ have been calculated.

In this analysis $N_{S_{exp}}$ consists on the number of events which contain a true J/ψ, that means events where a J/ψ is actually well reconstructed and corresponding to the system against which an other charmonium state recoils. On the other side, $N_{B_{exp}}$ are those events where a J/ψ is reconstructed in a wrong way, i.e. from QED events.

N$_{S_{exp}}$

Looking at the distribution of the J/ψ mass in figures 4.13, the expected number of signal events $N_{S_{exp}}$ are those below the peak of the J/ψ mass, in the range .
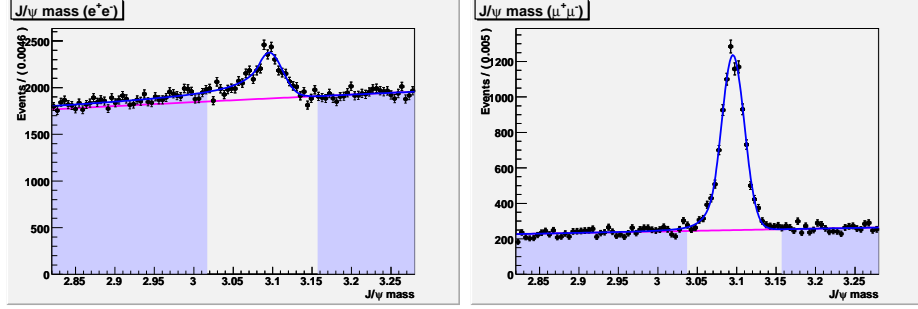
Figure 4.13: *Sidebands in the J/ψ mass distribution, for electrons and muons respectively. $N_{B_{exp}}$ is the result of the number of events fitted, under the linear fit (magenta), under the J/ψ resonance.*

It is calculated as in the following formula, in parallel for $J/\psi \rightarrow e^+e^-$ and $J/\psi \rightarrow \mu^+\mu^-$:

$$N_{S_{exp}} = \sigma(e^+e^- \rightarrow J/\psi\, c\bar{c})\mathcal{B}(c\bar{c} \rightarrow > 2charged)\ \mathcal{L}\ \epsilon_{sel}\ \mathcal{B}(J/\psi \rightarrow l^+l^-) \quad (4.4)$$

where $\sigma(e^+e^- \rightarrow J/\psi\, c\bar{c})\mathcal{B}(c\bar{c} \rightarrow > 2charged)$ is the product of the double charmonium production cross section times the branching fraction for final states with more than two charged tracks [28] , $\mathcal{L}$ is the integrated luminosity, ϵ_{sel} is the selection efficiency calculated on the signal MC and $\mathcal{B}(J/\psi \rightarrow l^+l^-)$ is the branching fraction for the J/ψ going to e^+e^- or $\mu^+\mu^-$ from PDG. In table 4.6 see the number of $N_{S_{exp}}$ for each resonance in the recoil system.

$N_{B_{exp}}$

In order to calculate the expected number of background events $N_{B_{exp}}$, the J/ψ mass distribution is fitted in the range 2.8 - 3.3 MeV/c^2. An unbinned fit was made using an extended PDF in Roofit corresponding to the sum of a linear function and a Crystal-Ball function. In figure 4.13 see the J/ψ mass distribution, for electronic and muonic decays respectively. The value $N_{B_{exp}}$ is the fitted number of events below the linear function in the peak range of the J/ψ mass.

For each resonance the results on $N_{S_{exp}}$ and $N_{B_{exp}}$ are summarized in the table 4.6: note that for the variable $N_{B_{exp}}$ there's no distinction among the four expected resonances in the recoil side, so only one results, for both electronic and muonic decay, have been obtained. This is correct, as the distribution of the background events in the recoil side is expected to be a 2nd order polynomial, without peaking background.

Function	Parameter	FinalValue	High Error	Low Error	GblCorr.
		$J/\psi \to e^+e^-$			
Linear function	$c_{1_{e^+e^-}}$	5.7059e+03	$\pm$ 4.04e+02		0.391402
	$c_{2_{e^+e^-}}$	-4.6164e+02	+0.00e+00	-1.06e+03	0.923193
	$N_{bkg_{e^+e^-}}$	1.8642e+05	+1.29e+03	-1.48e+03	0.956822
	$\alpha_{e^+e^-}$	7.3964e-01	+8.49e-02	-7.99e-02	0.876081
	$mean_{e^+e^-}$	3.0956e+00	+9.02e+04	-9.22e-04	0.467378
Crystal-Ball	$n_{e^+e^-}$	8.8461e-01	+5.05e-01	0.00e-01	0.983362
	$N_{sig_{e^+e^-}}$	8.4956e+03	+1.44e+03	-1.21e+03	0.981204
	$\sigma_{e^+e^-}$	1.6664e-02	+1.16e-03	-1.08e-03	0.592653
		$J/\psi \to \mu^+\mu^-$			
Linear function	$c_{1_{\mu^+\mu^-}}$	1.2073e+03	$\pm$ 8.98e+00		0.907000
	$c_{2_{\mu^+\mu^-}}$	-3.1731e+03	$\pm$ 3.42e+01		0.906989
	$N_{bkg_{\mu^+\mu^-}}$	2.2575e+04	$\pm$ 1.40e+03		0.927515
	$\alpha_{\mu^+\mu^-}$	1.6023e+00	$\pm$ 6.41e-01		0.997847
	$mean_{\mu^+\mu^-}$	3.0952e+00	+1.60e-04 $\mid$	-1.59e-04	0.191977
Crystal-Ball	$n_{\mu^+\mu^-}$	3.4148e+00	$\pm$ 7.90e+01		0.997674
	$N_{sig_{\mu^+\mu^-}}$	7.4788e+03	$\pm$ 1.33e+03		0.983955
	$\sigma_{\mu^+\mu^-}$	1.4496e-02	$\pm$ 2.37e-04		0.816090

Table 4.5: *Results of the binned fit with the extended PDF on the J/ψ mass.*

$J/\psi \to e^+e^-$

Recoil system	Produced events	Selected (e^+e^-)	ϵ_{sel} (e^+e^-)	$N_{S_{exp}}$ (e^+e^-)	$N_{B_{exp}}$ (e^+e^-)
$\eta_c(1S)$	17500	4699	26.6%	213 $\pm$ 34	
χ_{c0}	17500	5252	30.0%	141 $\pm$ 34	-
$\eta_c(2S)$	17500	4479	25.6%	191 $\pm$ 43	
$X(3940)$	87500	32724	37.4%	180 $\pm$ 46	
Total:			29.9%	725 $\pm$ 79	835 $\pm$ 263

$J/\psi \to \mu^+\mu^-$

Recoil system	Produced events	Selected $(\mu^+\mu^-)$	ϵ_{sel} $(\mu^+\mu^-)$	$N_{S_{exp}}$ $(\mu^+\mu^-)$	$N_{B_{exp}}$ $(\mu^+\mu^-)$
$\eta_c(1S)$	17500	5386	32.9%	228 $\pm$ 36	
χ_{c0}	17500	6050	36.9%	162 $\pm$ 39	-
$\eta_c(2S)$	17500	4999	29.7%	213 $\pm$ 48	
$X(3940)$	87500	32341	36.9%	182 $\pm$ 47	
Mean:			34.1 %	785 $\pm$ 86	440 $\pm$ 16

Table 4.6: *Summary of the masses (from PDG), the number of produced events in the montecarlo signal production, the number of rurviving events after the selection,the selecltion efficiency ϵ_{sel}, the expected signal events and expected background events for each recoil resonance, under the J/ψ mass resonance, before the cut on MLP.*

4.6.4 Optimization on significance

At the beginning of the "optimization" the cut value on MLP is varied so to find the point where the quantity $S/\sqrt{(S+B)}$ is maximized, taking into account an equivalent luminosity for signal and data. The optimization has been conducted by TMVA toolkit, as showed in figure 4.14 with the aim of obtaining the best set of cuts for the measurement.
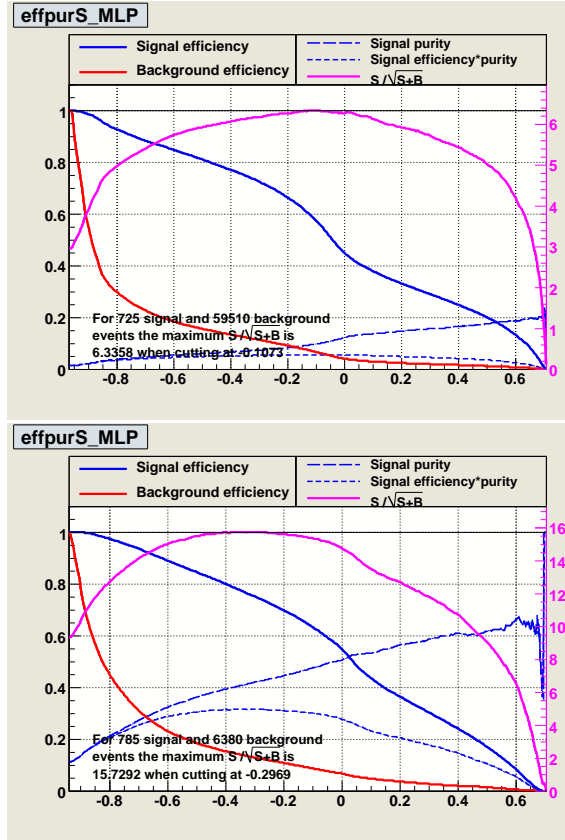
Figure 4.14: *The MLP effinciency, respectively for e^+e^- and $\mu^+\mu^-$ samples.*

Once obtained '$N_{S_{exp}}$ and $N_{B_{exp}}$ it is possible to cut on the MLP significance. In the plots 4.14 the significance of the MLP variable is the pink line, so the cut must be done in correspondence to maximum values of this lineshape, which are -0.11 for electronic decays and -0.30 for muonic decays. So the final cuts after this optimization are:

$$MLP > -0.11 \quad (e^+e^-)$$
$$MLP > -0.30 \quad (\mu^+\mu^-).$$

4.6.5   Summary on selection

Here have been summarized the cuts made for the channel $e^+e^- \rightarrow J/\psi\,c\bar{c}$:

- momentum $p*_{J/\psi} > 2.0\,\mathrm{GeV}/c$;

- number of charged tracks in the event is higher than 4;

- recoil mass M_{rec} between 2.0 GeV/c^2 and 4.3 GeV/c^2;

- $MLP > -0.11$ (e^+e^-) and $MLP > -0.30$ ($\mu^+\mu^-$);

The surviving event number after each cut is listed in table 4.7. After the total selection only 0.001% of the preselected data (skim + n-tuple production preselection) survive. In figure 4.15 the effect of the selection cuts on the J/ψ mass distribution, separated for e^+e^- and $\mu^+\mu^-$ sample respectively on the left and on the right. In particular, in 4.15(a) appear the distributions of the J/ψ mass *before* the final cut on MLP in the signal MC (on the top) and in the data (bottom). In 4.15(b) the same distributions *after* this cut. In the signal MC distributions, no evident changes are visible, as expected, while in the data distributions a clear removal of background is remarkable, with good results especially for the $\mu^+\mu^-$ channel.

Cut	Signal MC	Survival rate ϵ_{sig}	Data	Survival rate ϵ_{data}
Generated	105000	100%		
Preselection cuts	47133	44.9%	36174702	100.0%
$p*_{J/\psi} > 2.0\,\mathrm{GeV}/c$	47000	44.7%	21323724	58.9%
$NTRK > 4$	37082	%	1120515	3.10%
$2.0 < M_{rec} < 4.3\,\mathrm{GeV}/c^2$	35804	35.3 %	95835	0.26%
$MLP\ cut$	17239	16.4%	394	0.001%

Table 4.7: *Surviving events number in the event selection of $e^+e^- \rightarrow J/\psi\ c\bar{c}$ in both data and the signal MC sample. The "preselection cuts" row refers to the preselection done during the n-tuple production.*
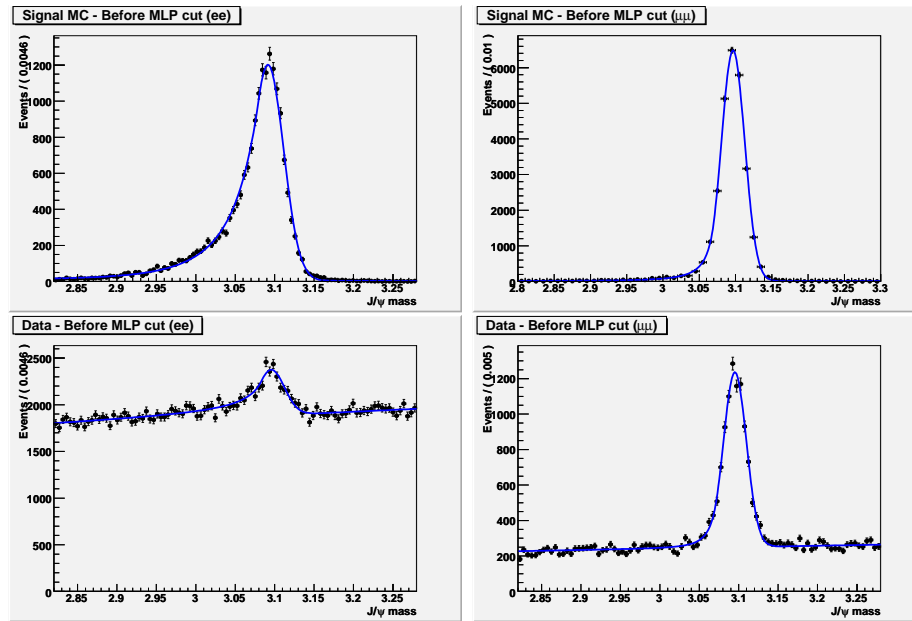
(a)
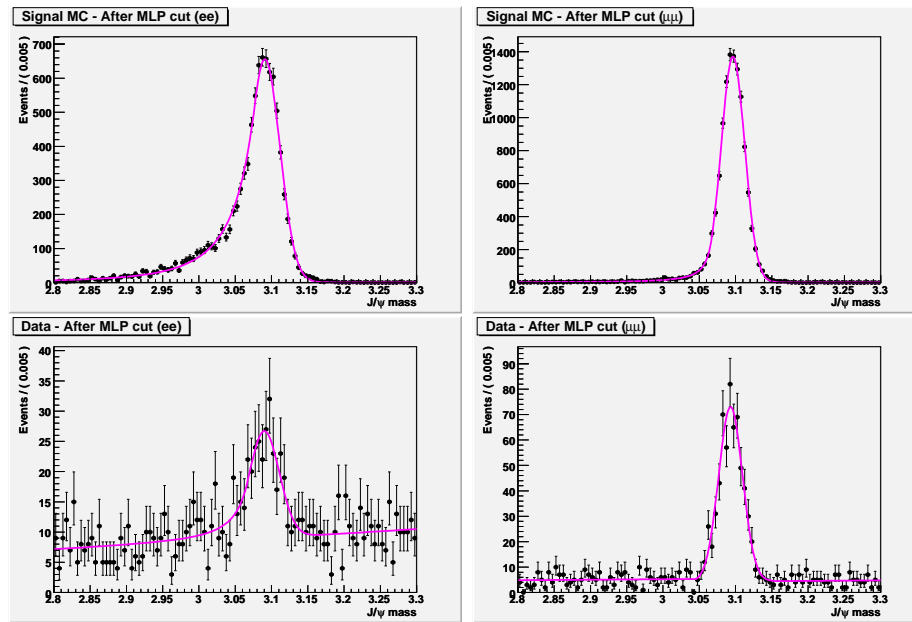
(b)

Figure 4.15: *Distribution of the mass of the J/ψ before (a) and after (b) the final cut based on MLP discriminant: e^+e^- decay on the left and $\mu^+\mu^-$ on the right.*

4.7   Fit to data

After the selection a ML fit will be applied to the mass distribution M_{rec} recoiling against the J/ψ. This study starts with a separated fit for signal MC (section 4.7.1) and background sidebands (section 4.7.2), then the global fit (background and signal embedded) on separated $J/\psi \to e^+e^-$ and $J/\psi \to \mu^+\mu^-$ samples. At the end the simultaneous fit to $J/\psi \to e^+e^-$ and $J/\psi \to \mu^+\mu^-$ channels (section 4.7.4).

Toy MC studies are performed in order to test the fit procedure. Pulls distributions for each measurable variable have been produced and then fitted with a Gaussian profile; it turns out that generally the means are compatible with zero and the widths are compatible with one, and therefore the fit is correct.

4.7.1   Fit and toys validation on the signal MC

In the region between 2.5 GeV/c^2 and 4.3 GeV/c^2, the M_{rec} distribution for the signal is composed by four resonances and the shape of each resonance is well described by a $Voigtian$, that is $Breit-Wigner$ function convoluted with a *single Gaussian* (see figure 4.17). In the first part of this section (in 4.7.1) there will be described a dedicated study to measure the detector resolution, then the fit and the validation using toy MC.

Resolution studies

An important point is to obtain the detector resolution for each resonance, so as to measure the natural widths of $\eta_c, \chi_{c0}, \eta_c(2S), X(3940)$.

In order to do that, a MC signal, generated with *zero width* for the resonances, has been produced.

Indeed, the original idea was to fit the signal MC with a Breit-Wigner convoluted with a Gaussian (Voigtian), where the Breit-Wigner would act as the natural width of the resonances and the Gaussian as the detector resolution. But by trying to fit the M_{rec} distribution (generated with zero width), it's clear that the single Gaussian lineshape does not model the detector resolution.

Actually, as it's possible to see in figure 4.16, the detector resolution can be fitted well by a Voigtian too, and the results of the fit are in table 4.8.

Take into account that the convolution of a Voigtian (with parameters Γ_{res} and σ_{res}) and a Breit-Wigner (with width Γ_N) results in a Voigtian as well, with parameters $\Gamma = \Gamma_{res} + \Gamma_N$ and σ_{res}. This can be proven using
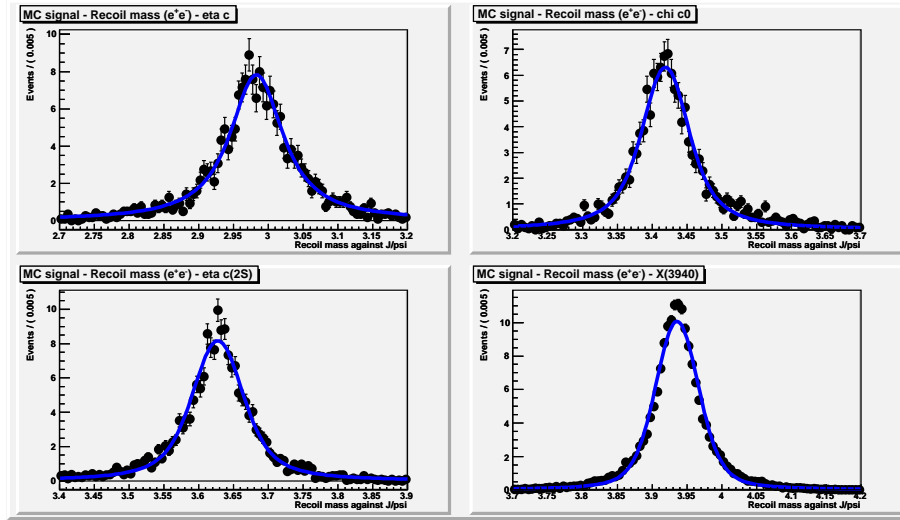
(a)
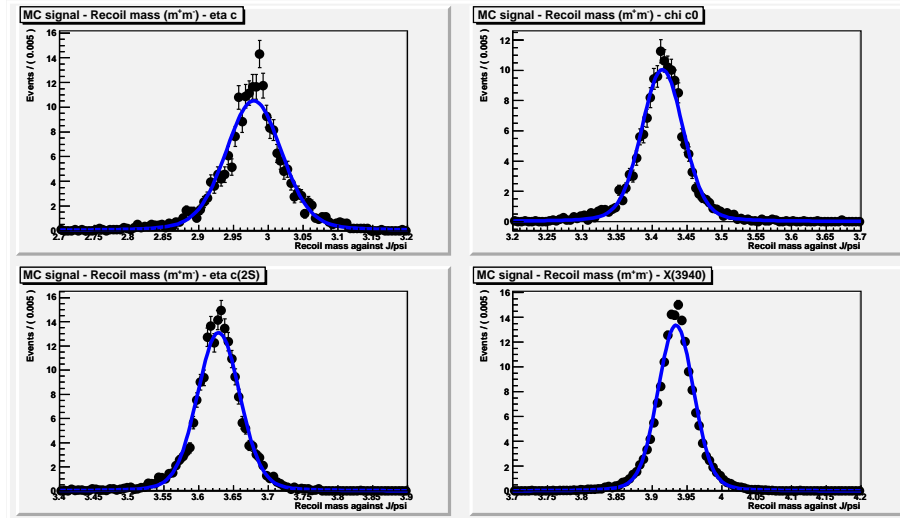
(b)

Figure 4.16: *Fit on the recoil mass for each resonance $(\eta_c, \chi_{c0}, \eta_c(2S), X(3940))$ in the signal MC produced with zero width, respectively for $J/\psi \to e^+e^-$ and $J/\psi \to \mu^+\mu^-$. Notice that in the X(3940) plots statistical error are smaller than in others because of the larger statistics available in the Montecarlo sample.*

$$J/\psi \to e^+ e^-$$

Particle	Mean (GeV/c^2)	Γ_{BW} (GeV/c^2)	σ_G
$\eta_c(1S)$	2.983 ± 0.004	0.087 ± 0.013	0.009 ± 0.014
χ_{c0}	3.419 ± 0.004	0.054 ± 0.013	0.020 ± 0.010
$\eta_c(2S)$	3.628 ± 0.004	0.051 ± 0.012	0.024 ± 0.008
$X(3940)$	3.936 ± 0.003	0.025 ± 0.008	0.025 ± 0.006

$$J/\psi \to \mu^+ \mu^-$$

Particle	Mean (GeV/c^2)	Γ_{BW} (GeV/c^2)	σ_G
$\eta_c(1S)$	2.980 ± 0.003	0.019 ± 0.008	0.036 ± 0.005
χ_{c0}	3.415 ± 0.003	0.012 ± 0.006	0.027 ± 0.004
$\eta_c(2S)$	3.629 ± 0.002	0.011 ± 0.005	0.028 ± 0.003
$X(3940)$	3.934 ± 0.002	0.090 ± 0.005	0.024 ± 0.003

Table 4.8: *Fit results of the recoil mass against J/ψ, in the signal MC sample generated with zero width.*

the convolution theorem and the associativity of the convolution operation ($f * (g * h) = (f * g) * h$).

So, the signal MC will be fitted by a Voigtian, after fixing the resolution parameters: so the natural width will be: $\Gamma_N = \Gamma - \Gamma_{res}$.

Fit on the signal MC

An unbinned maximum likelihood fit is performed and the number of the signal events, the mass and the width are floating parameters. The resolution's parameters are fixed to the values obtained after the resolution study (see table 4.8). In table 4.9 the results of the fit on the recoil mass against J/ψ.

$$J/\psi \to e^+ e^-$$

Particle	Mean (GeV/c^2)	Γ_{BW}	# events
$\eta_c(1S)$	2.984 ± 0.004	0.079 ± 0.008	203 ± 15
χ_{c0}	3.420 ± 0.004	0.046 ± 0.011	142 ± 15
$\eta_c(2S)$	3.632 ± 0.004	0.058 ± 0.011	205 ± 19
$X(3940)$	3.935 ± 0.004	0.053 ± 0.009	174 ± 15

$$J/\psi \to \mu^+ \mu^-$$

Particle	Mean (GeV/c^2)	Γ_{BW}	# events
$\eta_c(1S)$	2.980 ± 0.004	0.030 ± 0.006	225 ± 15
χ_{c0}	3.417 ± 0.003	0.016 ± 0.006	160 ± 14
$\eta_c(2S)$	3.635 ± 0.003	0.021 ± 0.006	216 ± 16
$X(3940)$	3.934 ± 0.004	0.045 ± 0.008	183 ± 14

Table 4.9: *Fit results of the recoil mass against J/ψ, in the signal MC.*
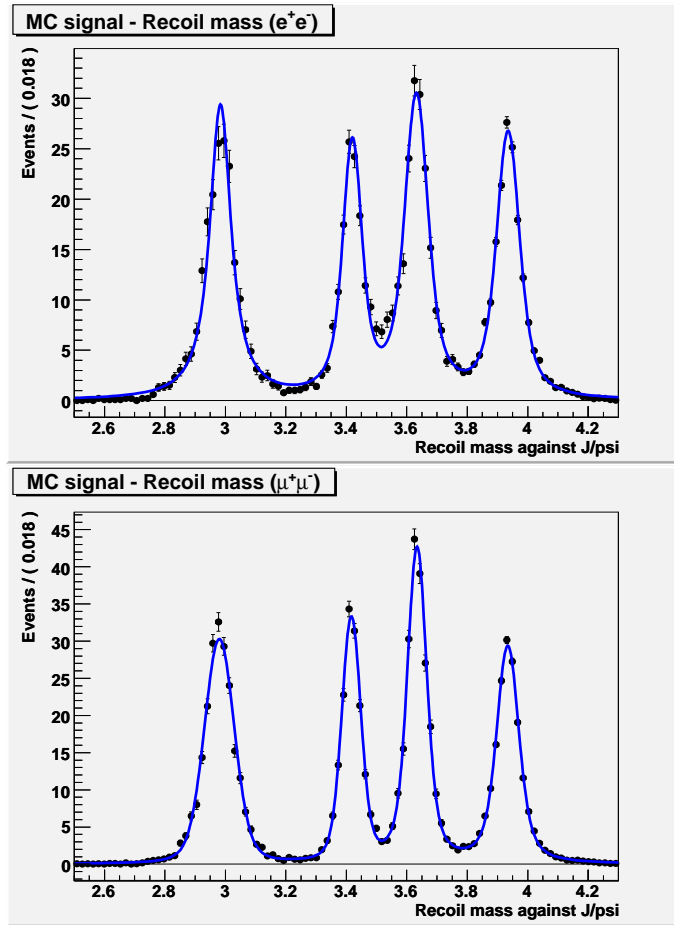
Figure 4.17: *Fit on the recoil mass distribution in the signal MC of the channel $e^+e^- \to J/\psi\, c\bar{c}$, respectively for $J/\psi \to e^+e^-$ and $J/\psi \to \mu^+\mu^-$.*

Validation of the signal fit

The generating and fitting PDF is the sum of the four extended PDFs, that means with floating number of events. The total expected number of signal events are 725 for the $J/\psi \rightarrow e^+e^-$ sample and 785 for the $J/\psi \rightarrow \mu^+\mu^-$ sample. One thousand esperiments have been generated with such number of events. Two toy MC studies have been done: for the $J/\psi \rightarrow e^+e^-$ and $J/\psi \rightarrow \mu^+\mu^-$ samples. In the following pages are shown the pulls of masses, widths and number of events, respectively for electronic and muonic channel. The first three figures (4.18, 4.19, 4.20) refer to the $J/\psi \rightarrow e^+e^-$ sample, instead figures 4.21, 4.22, 4.23 are those from $J/\psi \rightarrow \mu^+\mu^-$ sample.
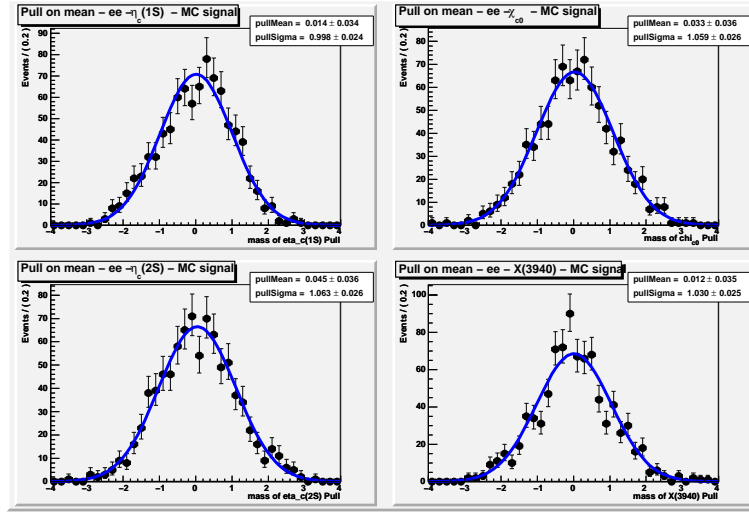
Figure 4.18: *Masses pulls for η_c, χ_{c0}, $\eta_c(2S)$ and $X(3940)$ resonances in the signal MC, rescaled to the expected number of events, in the $J/\psi \rightarrow e^+e^-$ sample.*
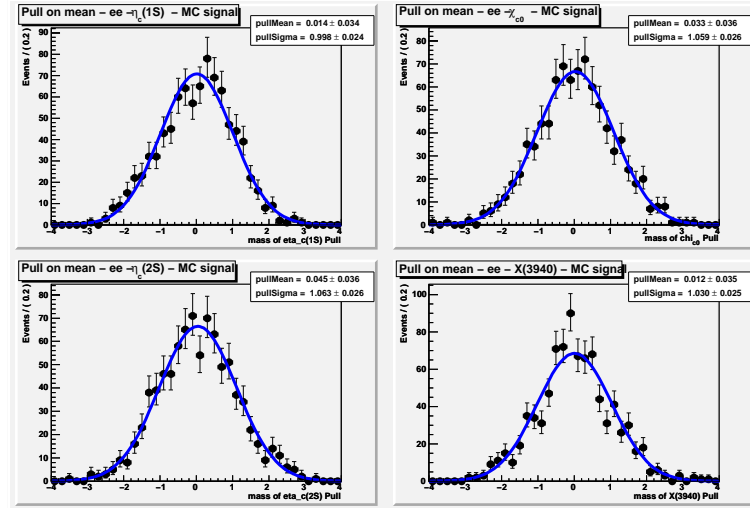
Figure 4.19: *Widths pulls for η_c, χ_{c0}, $\eta_c(2S)$ and $X(3940)$ resonances in the signal MC, rescaled to the expected number of events, in the $J/\psi \to e^+e^-$ sample.*
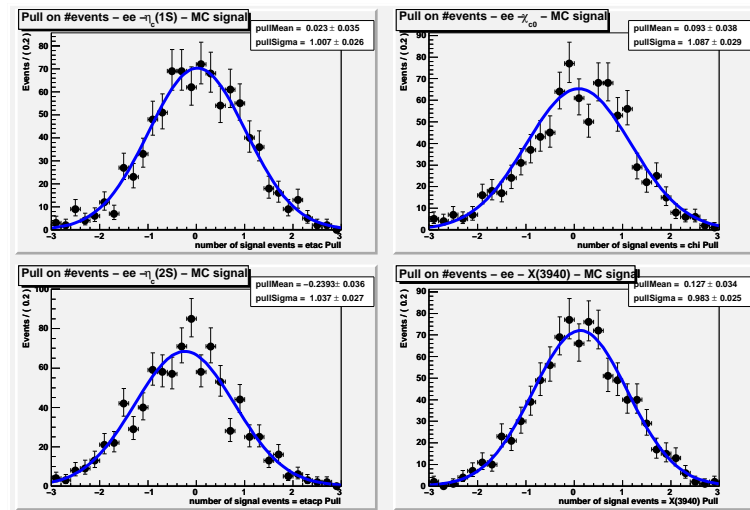
Figure 4.20: *Number of events pulls for η_c, χ_{c0}, $\eta_c(2S)$ and $X(3940)$ resonances in the signal MC in the $J/\psi \to e^+e^-$ sample.*
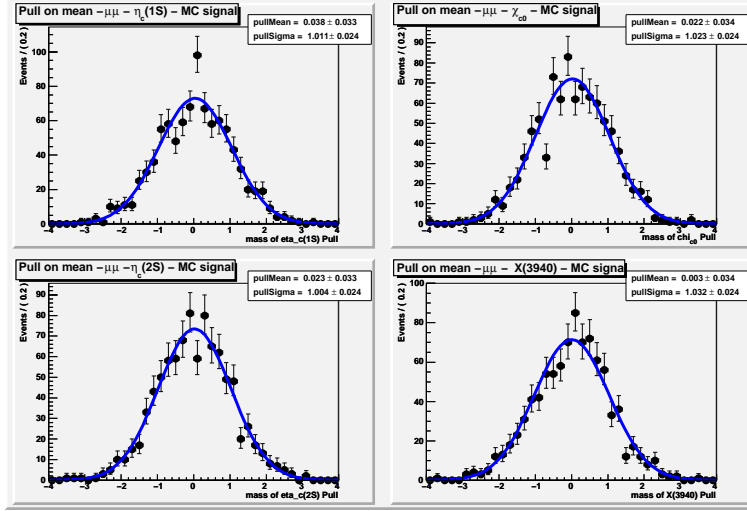
Figure 4.21: *Masses pulls for η_c, χ_{c0}, $\eta_c(2S)$ and $X(3940)$ resonances in the signal MC, rescaled to the expectd number of events, in the $J/\psi \to \mu^+\mu^-$ sample.*
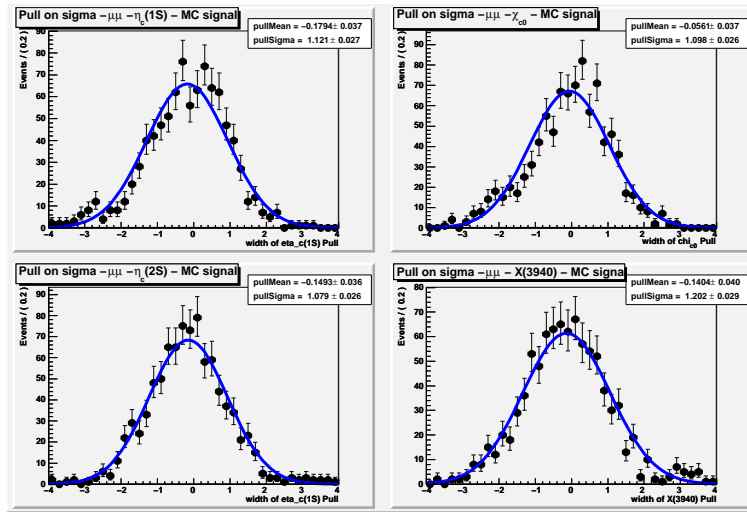
Figure 4.22: *Widths pulls for η_c, χ_{c0}, $\eta_c(2S)$ and $X(3940)$ resonances in the signal MC, rescaled to the expected number of events, in the $J/\psi \to \mu^+\mu^-$ sample.*
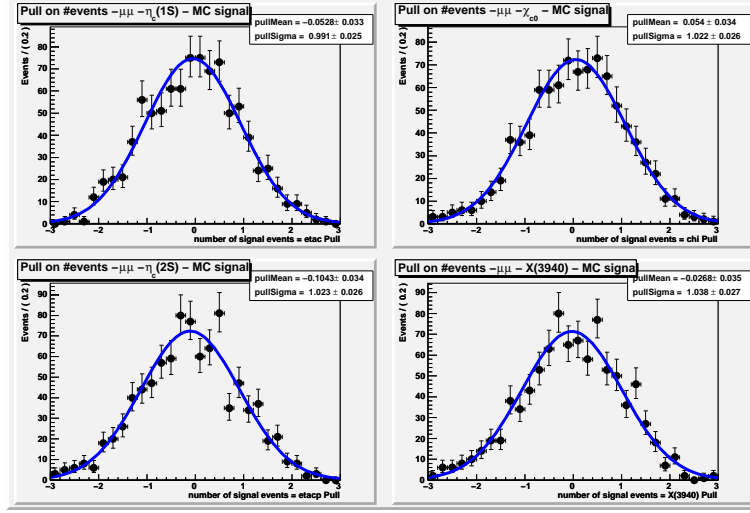
Figure 4.23: *Number of events pulls for η_c, χ_{c0}, $\eta_c(2S)$ and $X(3940)$ resonances in the signal MC in the $J/\psi \to \mu^+\mu^-$ sample.*

4.7.2   Fit and toys validation on the background

The background sample is composed by events of the data sidebands of the J/ψ mass distribution, i.e.

$$|m(\mu^+\mu^-) - 3.097 \,\text{GeV}/c^2| > 0.060 \,\text{GeV}/c^2, \quad \text{for } J/\psi \to \mu^+\mu^-$$

$$\begin{cases} (m(e^+e^-) - 3.097 \,\text{GeV}/c^2) > 0.060 \,\text{GeV}/c^2, \\ (m(e^+e^-) - 3.097 \,\text{GeV}/c^2) < -0.080 \,\text{GeV}/c^2, \end{cases} \quad \text{for } J/\psi \to e^+e^-$$

The background is fitted by a 2nd order polynomial (see figure 4.24). An unbinned maximum likelihood fit is performed, on this region, and the results of the fit appear in the table 4.10: for each sample (e^+e^-, $\mu^+\mu^-$ and together) appear the three parameters a_1 and a_2 which describe the polynomial, and the number of events. The values have been reported before (*Initial*) and after (*Final*) the fit.

Also in this case, a toy MC has been done, reproducing 1000 experiment with 835 events in the $J/\psi \to e^+e^-$ case and 440 events in the $J/\psi \to \mu^+\mu^-$ case. In figure 4.25 the pull of the number of events.
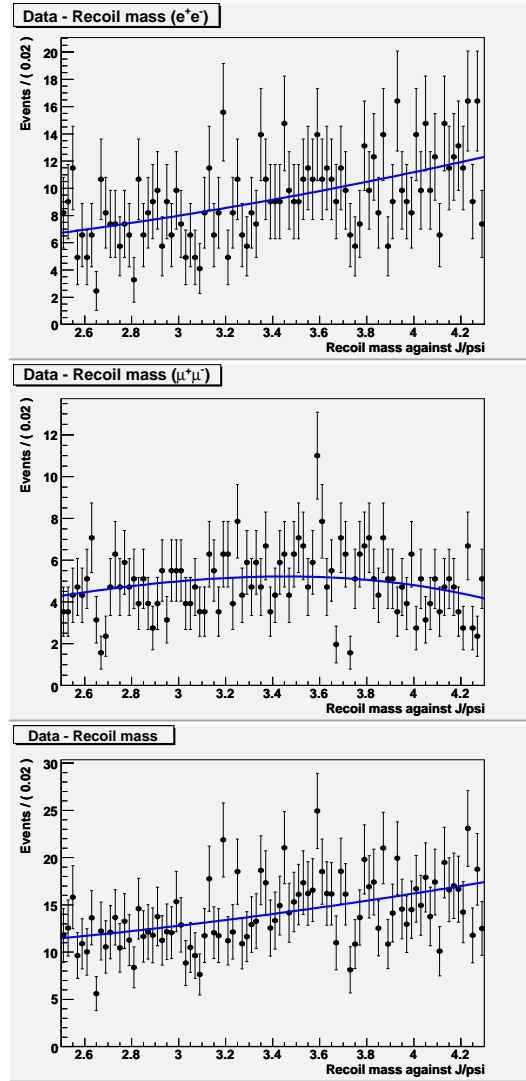
Figure 4.24: *Fit on the recoil mass distribution for the sidebands of the J/ψ, respectively for $J/\psi \rightarrow e^+e^-$, $J/\psi \rightarrow \mu^+\mu^-$ and together.*

Parameter	$J/\psi \rightarrow e^+e^-$		$J/\psi \rightarrow \mu^+\mu^-$		Total sample	
	Initial	Final	Initial	Final	Initial	Final
a_1	0.00	0.12 ± 0.36	0.00	4.99 ± 4.99	0.00	0.06 ± 0.00
a_2	1.00	-0.00 ± 0.03	0.00	-0.96 ± 0.86	0.00	0.00 ± 0.00
$Nevents$	835	834 ± 29	440	440 ± 21	1235	1274 ± 36

Table 4.10: *Fit results of the recoil mass against J/ψ, for the background.*
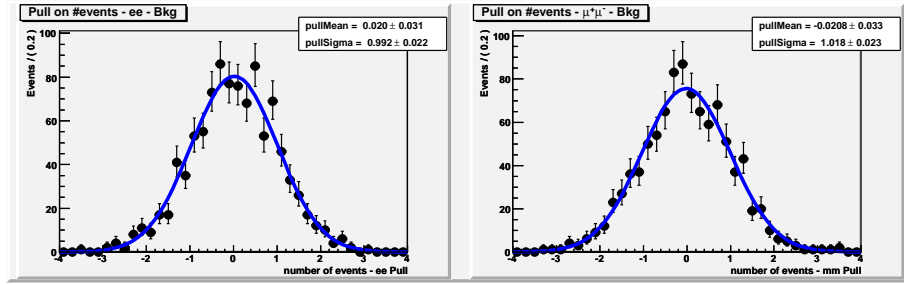
Figure 4.25: *Pulls on the number of events in the sidebands background, respectively for the $J/\psi \to e^+e^-$ and $J/\psi \to \mu^+\mu^-$ sample.*

4.7.3   Global fit with signal and background embedded

Once fitted separately signal and background, the aim of the fit procedure is to perform a global fit, which contain the background from the J/ψ sidebands, and the signal from the MC data have been scaled and summed; in this way it is possible to reproduce an expected distribution of the recoil mass distribution, once unblind the data. As visible in figure 4.27 the expected distribution of M_{rec} is in good shape, with a background pretty low, in particular if compared with the results from this previous analysis from *BABAR* [28], visible in figure 4.28, where the binning is the same but the statistics is lower (124 fb^{-1}).
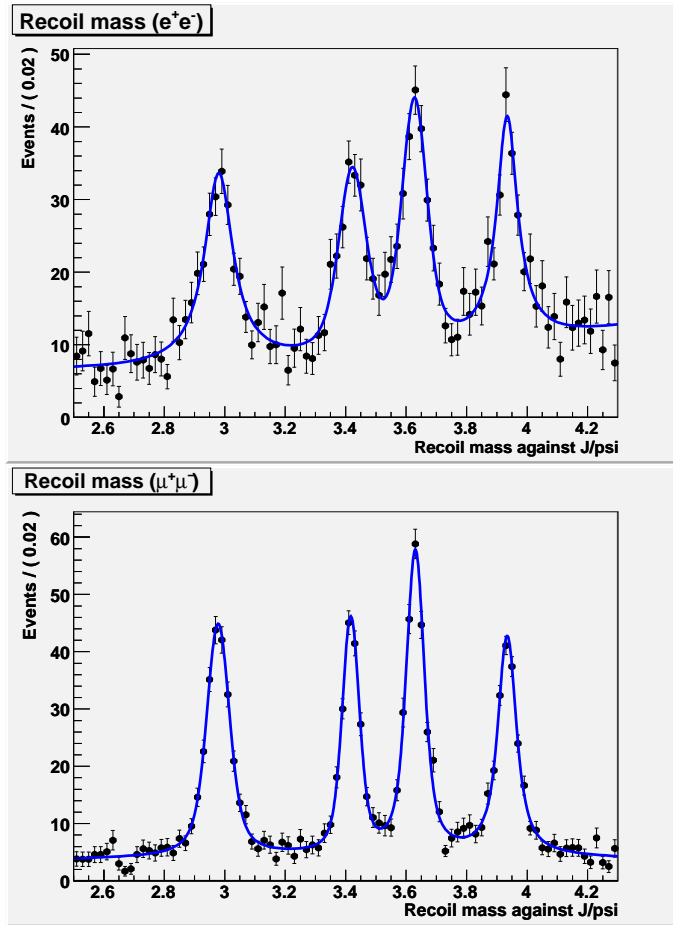
Figure 4.26: *Global fit on the recoil mass distribution for the channel $e^+e^- \rightarrow J/\psi\, c\bar{c}$, respectively for $J/\psi \rightarrow e^+e^-$ and $J/\psi \rightarrow \mu^+\mu^-$.*
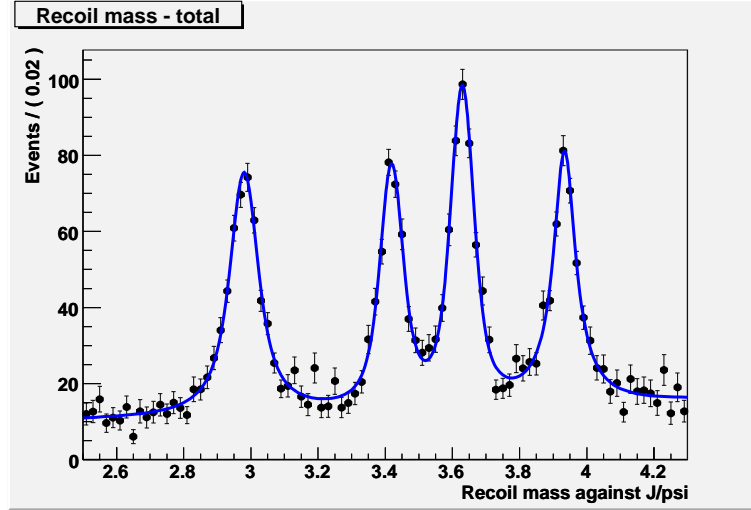
Figure 4.27: *Global fit on the recoil mass distribution for the channel $e^+e^- \to J/\psi\, c\bar{c}$.*
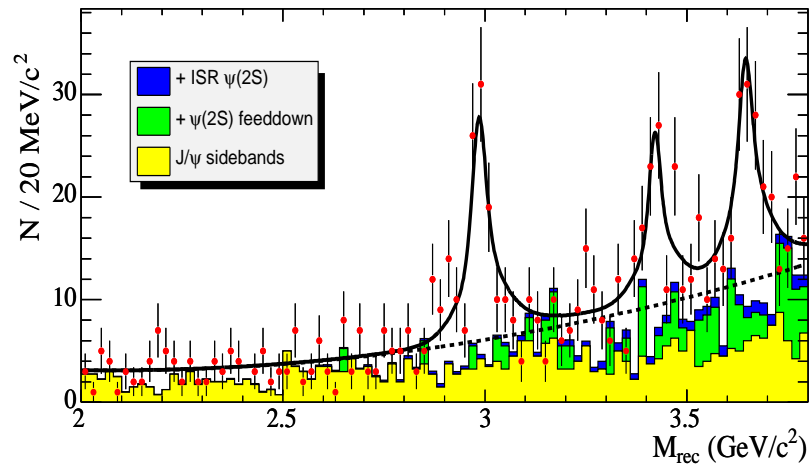
Figure 4.28: *M_{rec} distribution in the previous analysis in BaBar [28].*

Global fit validation

In order to validate the global fit, a "manual" toy MC has been carried out. The aim of this method was to make a more realistic toy MC, where the samples are not generated by a PDF (Probability Density Function) fitting a distribution, but they are taken directly from the data set available, by creating combinations between background and signal to produce various global distributions to be fitted.

Taking into account that to compose a *global sample* it's necessary to have 4 subsamples from signal, corresponding to the four resonances, and 1 sub-sample for background, the experiments of the toy MC have been produced with the following procedure (done separately for e^+e^- and $\mu^+\mu^-$ samples):

- the total MC signal have been splitted in sub-samples, with the exact number of events expected for each resonance, as shown in the table 4.11;

- 20 background samples have been created according to the expected number of events, taking events randomly from the existing sample. Notice that the original background dataset hasn't been splitted, being too small to allow more than one complete sample;

- the global dataset to fit has been composed randomly by one of each kind of dataset (four for the resonances plus one for the background);

- 100 experiments have been produced, both for $J/\psi \rightarrow e^+e^-$ and $J/\psi \rightarrow \mu^+\mu^-$;

- for each experiment the pull of the masses, widths and number of events have been calculated and plotted.

In the next page, the plots of the pulls of masses, widths and number of events, separately for e^+e^- and $\mu^+\mu^-$ sample. These distributions are fitted with gaussians centered in 0 and wide 1.

Sample	Available # events	# expected	# subsamples
$J/\psi \rightarrow e^+e^-$			
$\eta_c(1S)$	1537	213	7
χ_{c0}	2129	141	15
$\eta_c(2S)$	2300	191	12
$X(3940)$	10549	180	58
Background	1018	835	20
$J/\psi \rightarrow \mu^+\mu^-$			
$\eta_c(1S)$	2447	228	11
χ_{c0}	2867	162	18
$\eta_c(2S)$	3104	213	15
$X(3940)$	13707	182	75
Background	1120	440	20

Table 4.11: *Number of events available in the original dataset (after selection), number of the expected events and final number of subsample, for each resonance and background, in order to perform the manual toy MC.*
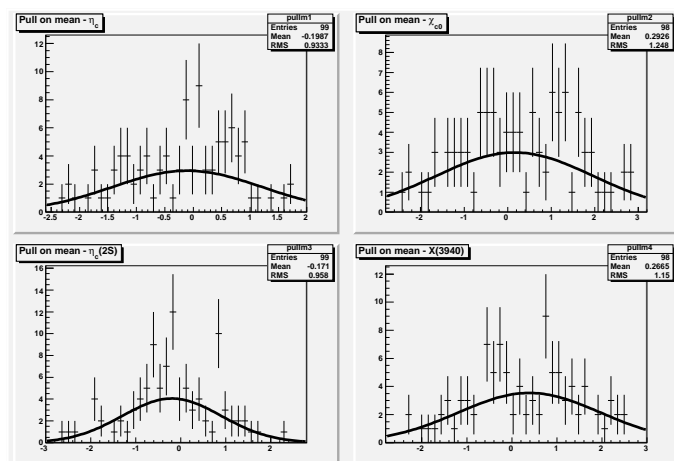
Figure 4.29: *Pulls of the masses resulting from the "manual" toy MC in the recoil mass distribution for the channel $e^+e^- \rightarrow J/\psi\, c\bar{c}$, $J/\psi \rightarrow e^+e^-$.*
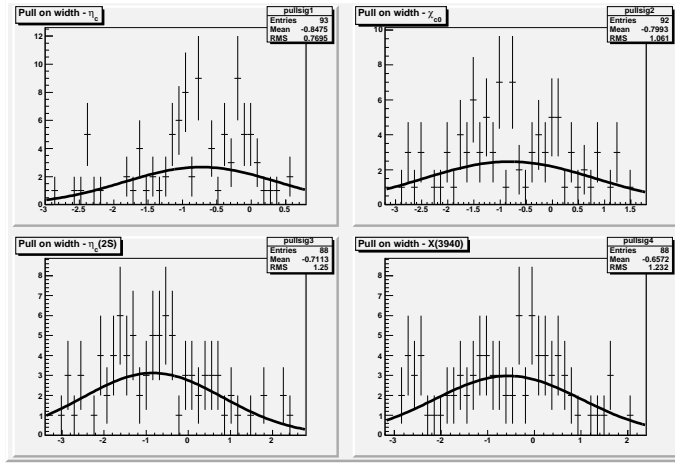
Figure 4.30: *Pulls of the masses resulting from the "manual" toy MC in the recoil mass distribution for the channel $e^+e^- \rightarrow J/\psi\,c\bar{c}$, $J/\psi \rightarrow e^+e^-$.*
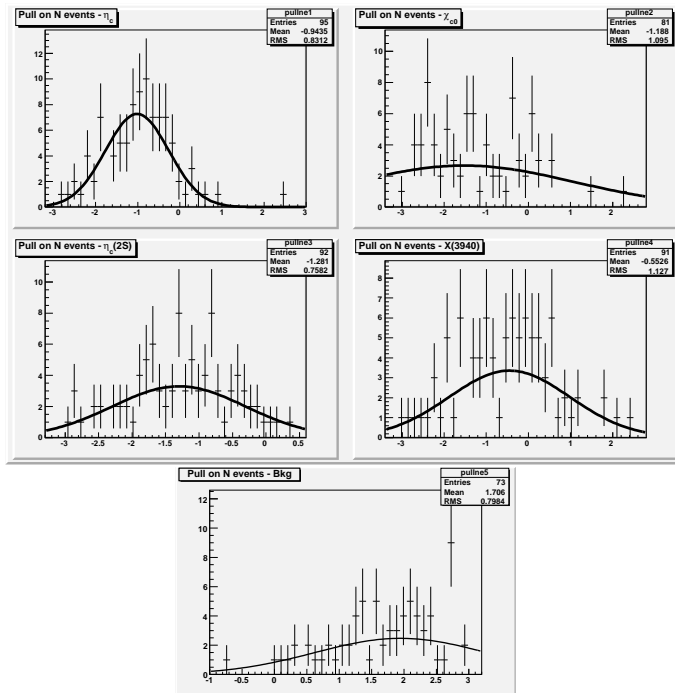
Figure 4.31: *Pulls of the widths in the recoil mass distribution for the channel $e^+e^- \rightarrow J/\psi\,c\bar{c}$, $J/\psi \rightarrow e^+e^-$.*
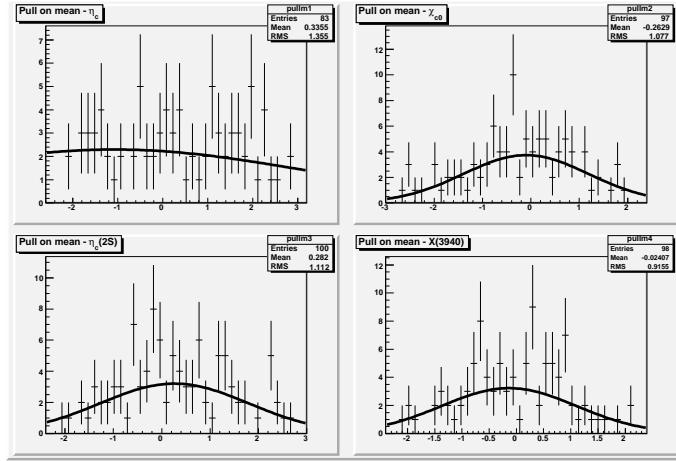
Figure 4.32: *Pulls of the masses resulting from the "manual" toy MC in the recoil mass distribution for the channel $e^+e^- \to J/\psi\, c\bar{c}$, $J/\psi \to \mu^+\mu^-$.*
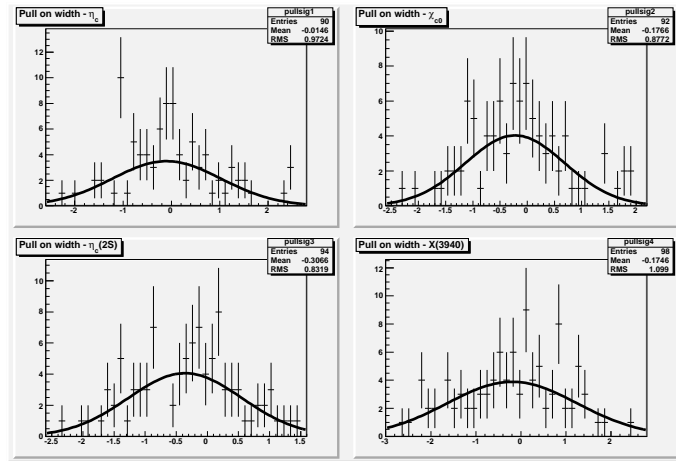
Figure 4.33: *Pulls of the masses resulting from the "manual" toy MC in the recoil mass distribution for the channel $e^+e^- \to J/\psi\, c\bar{c}$, $J/\psi \to \mu^+\mu^-$.*
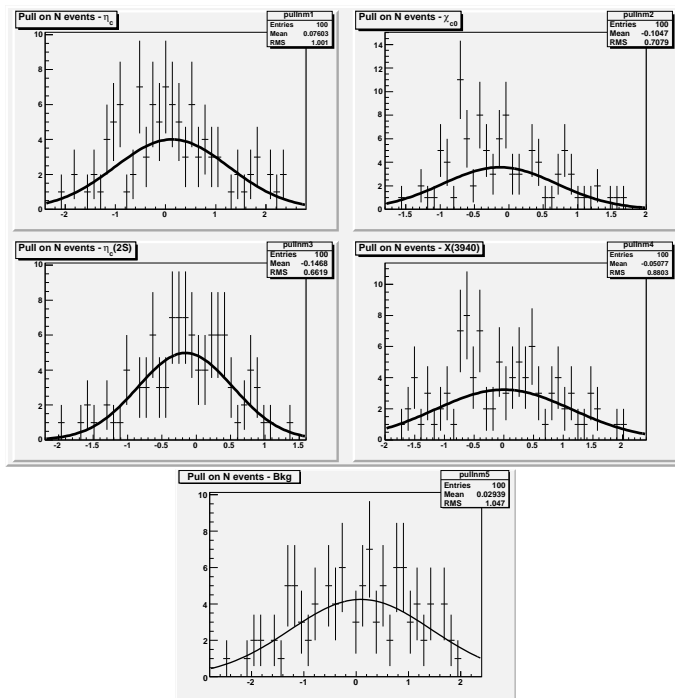
Figure 4.34: *Pulls of the widths in the recoil mass distribution for the channel* $e^+e^- \rightarrow J/\psi\, c\bar{c}$, $J/\psi \rightarrow \mu^+\mu^-$.

4.7.4   Simultaneous fit

A simultaneous fit is a powerful tool to build "simultaneous" PDFs that are defined in terms component PDFs that are identical in structure, but have different parameters.

In this case, we perform a simultaneous fit between e^+e^- and $\mu^+\mu^-$ sample. In the plot 4.35 there is the simultaneous fit on the total dataset (e^+e^- plus $\mu^+\mu^-$ channels). Table 4.12 summarizes the fitted parameters related to the figure 4.35.
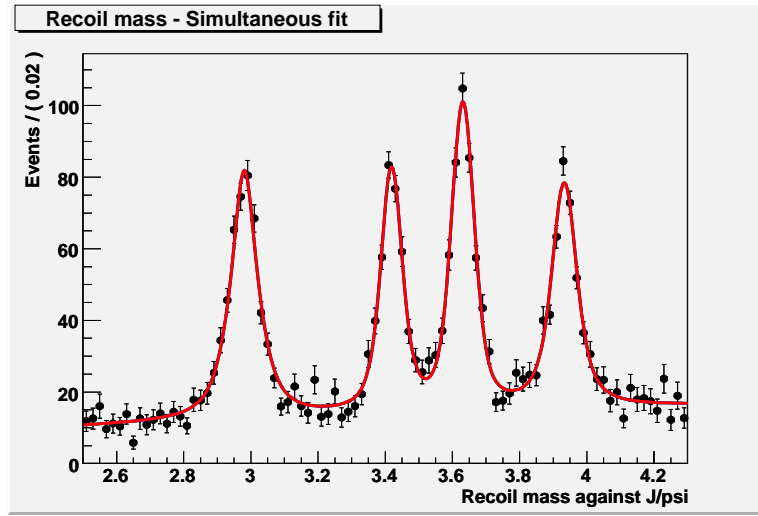
Figure 4.35: *Simultaneousfit on the recoil mass distribution.*

In the next pages plots of the pulls of masses, widths and number of events (separately for e^+e^- and $\mu^+\mu^-$ sample) are visible. The validation of the simultaneous fit is performed with the "manual" toy MC, as explained in section 4.7.3, performing 100 experiments.

Particle	Mean (GeV/c^2)	Γ_{BW}	# events (e^+e^-)	# events ($\mu^+\mu^-$)
$\eta_c(1S)$	2.980 ± 0.003	0.063 ± 0.009	183 ± 23	264 ± 22
χ_{c0}	3.419 ± 0.003	0.037 ± 0.009	145 ± 20	191 ± 19
$\eta_c(2S)$	3.631 ± 0.003	0.034 ± 0.008	185 ± 21	249 ± 21
$X(3940)$	3.933 ± 0.003	0.053 ± 0.011	170 ± 23	201 ± 21
background	-	-	876 ± 50	321 ± 37

Table 4.12: *Results of the simultaneous fit of the recoil mass against J/ψ, visible in Fig. 4.35.*
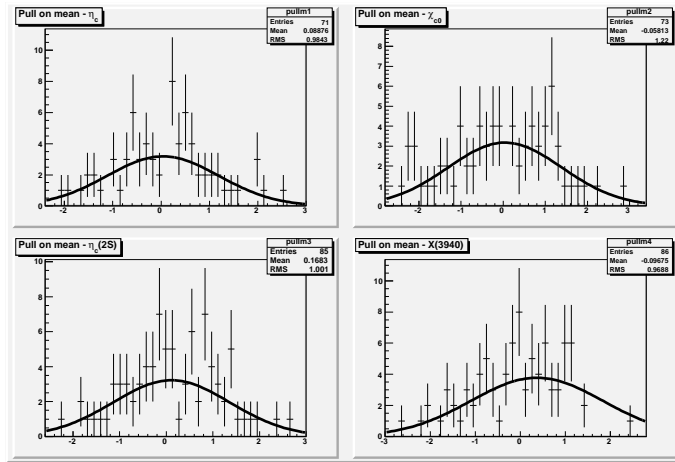
Figure 4.36: *Pulls of the masses resulting from the "manual" toy MC in the recoil mass distribution, from the simultaneous fit.*
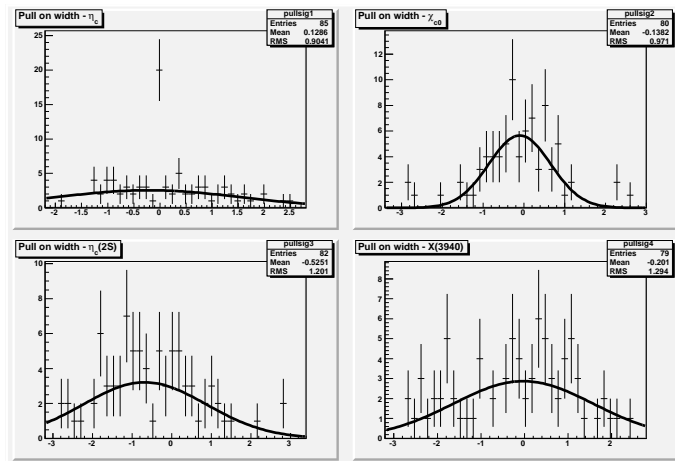
Figure 4.37: *Pulls of the masses resulting from the "manual" toy MC in the recoil mass distribution for the cha*
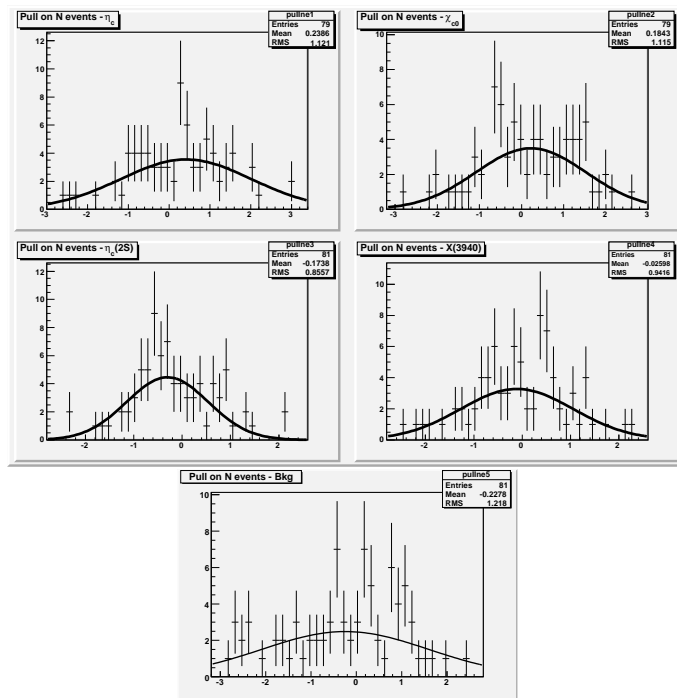
Figure 4.38: *Pulls of the widths in the recoil mass distribution for the channel* $e^+e^- \to J/\psi\, c\bar{c}$, $J/\psi \to e^+e^-$.
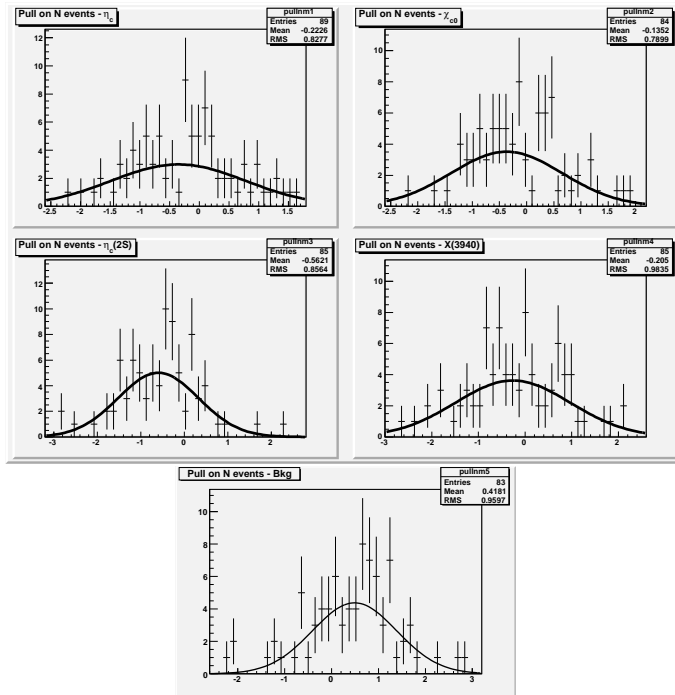
Figure 4.39: *Pulls of the widths in the recoil mass distribution for the channel $e^+e^- \rightarrow J/\psi\, c\bar{c}$, $J/\psi \rightarrow \mu^+\mu^-$.*

Chapter 5

Results

5.1 Unblind up to 3.8 GeV

After the good results of the fit validation performed in section 4.7.3 of the previous chapter, we are ready to unblind the data on the interested region. Anyway we first unblind the region of the mass recoiling against the J/ψ for the Run1-Run6 data taking in *BABAR* data in order to validate this analysis in the same region of the old one [28].
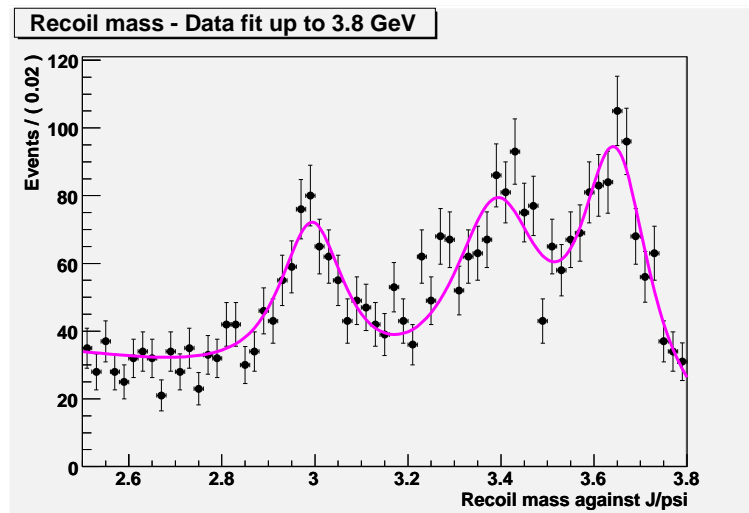
Figure 5.1:

111

5.2   Outlook

This analysis leaves many interesting possibilities to extend it, in particular the following ways:

- study, similarly to the channel $e^+e^- \to J/\psi \; c\bar{c}$, also the channel $e^+e^- \to \psi(2S) \; c\bar{c}$, for the Run1-Run6 periods; in the previous analysis [28], the authors already performed it only for Run1-Run4 data-taking;

- study the production of double charmonium production at $\Upsilon(2S)$ and $\Upsilon(3S)$ energies. *BABAR* experiment in the last period of data-taking collected a big amount of data off $\Upsilon(4S)$ resonance, in particular 30.2 fb^{-1} at the Y(3S), 14.5 fb^{-1} at $\Upsilon(2S)$ energy, and 5 fb^{-1} above $\Upsilon(4S)$ energy. With this remarkable amount of data becomes interesting to perform this analysis in order to know something more about the mechanism of double charmonium production, in fact to see what happens at different energies can tell which are the contributions to the cross section.

List of Figures

List of Tables

Bibliography

[1] J. J. Aubert *et al.* [E598 Collaboration], Phys. Rev. Lett. **33** (1974) 1404. 1

[2] J. E. Augustin *et al.* [SLAC-SP-017 Collaboration], Phys. Rev. Lett. **33** (1974) 1406. 1

[3] E. Eichten, K. Gottfried, T. Kinoshita, K. D. Lane and T. M. Yan, Phys. Rev. D **17** (1978) 3090 [Erratum-ibid. D **21** (1980) 313]. 1.1

[4] W. Kwong, J. L. Rosner and C. Quigg, Ann. Rev. Nucl. Part. Sci. **37** (1987) 325. 1.1

[5] C. Amsler *et al.* [Particle Data Group], Phys. Lett. B **667** (2008) 1. 1.1, 1, 1.5.2, 1.1, 5.2, 5.2

[6] R. Gupta, arXiv:hep-lat/9807028. 1.1

[7] N. Brambilla, *In the Proceedings of International Conference on Heavy Quarks and Leptons (HQL 06), Munich, Germany, 16-20 Oct 2006, pp 004* [arXiv:hep-ph/0702105]. (document)

[8] D. J. Gross and F. Wilczek, Phys. Rev. Lett. **30** (1973) 1343. 1.2

[9] H. D. Politzer, Phys. Rev. Lett. **30** (1973) 1346. 1.2

[10] E. E. Salpeter, arXiv:0811.1050 [physics.hist-ph]. 1.3

[11] H. Sonoda, arXiv:hep-th/0603151. 1.3

[12] N. Isgur and M. B. Wise, Phys. Lett. B **237** (1990) 527. 1.3

[13] M. Neubert, Phys. Rept. **245** (1994) 259 [arXiv:hep-ph/9306320]. 1.3

[14] G. T. Bodwin, E. Braaten and G. P. Lepage, Phys. Rev. D **51** (1995) 1125 [Erratum-ibid. D **55** (1997) 5853] [arXiv:hep-ph/9407339]. 1.3, 1.4.1, 2.1

[15] W. E. Caswell and G. P. Lepage, Phys. Lett. B **167** (1986) 437. 1.3, 1.4

[16] K. Abe *et al.*, Phys. Rev. Lett. **98** (2007) 082001 [arXiv:hep-ex/0507019]. (document), 1.5.1, 1.5.3, 2.4, 2.4.1

[17] C. Edwards *et al.*, Phys. Rev. Lett. **48** (1982) 70. 1.5.2

[18] S. K. Choi *et al.* [BELLE collaboration], Phys. Rev. Lett. **89** (2002) 102001 [Erratum-ibid. **89** (2002) 129901] [arXiv:hep-ex/0206002]. 1.5.2

[19] D. M. Asner *et al.* [CLEO Collaboration], Phys. Rev. Lett. **92** (2004) 142001 [arXiv:hep-ex/0312058]. 1.5.2

[20] B. Aubert *et al.* [BABAR Collaboration], Phys. Rev. Lett. **92** (2004) 142002 [arXiv:hep-ex/0311038]. 1.5.2

[21] J. L. Rosner *et al.* [CLEO Collaboration], Phys. Rev. Lett. **95** (2005) 102003 [arXiv:hep-ex/0505073]. 1.5.2

[22] P. A. Rapidis *et al.*, Phys. Rev. Lett. **39** (1977) 526 [Erratum-ibid. **39** (1977) 974]. 1.5.2

[23] P. Pakhlov *et al.* [Belle Collaboration], Phys. Rev. Lett. **100** (2008) 202001 [arXiv:0708.3812 [hep-ex]]. 1.5.3

[24] K. Abe *et al.* [Belle Collaboration], Phys. Rev. Lett. **94** (2005) 182002 [arXiv:hep-ex/0408126]. 1.5.3

[25] B. Aubert *et al.* [BaBar Collaboration], Phys. Rev. Lett. **101** (2008) 082001 [arXiv:0711.2047 [hep-ex]]. 1.5.3

[26] G. V. Pakhlova, arXiv:0810.4114 [hep-ex]. 1.5.3

[27] K. Abe *et al.* [Belle Collaboration], Phys. Rev. D **70** (2004) 071102 [arXiv:hep-ex/0407009]. 2.1, 2.3, 2.3, 5.2

[28] B. Aubert *et al.* [BABAR Collaboration], Phys. Rev. D **72** (2005) 031101 [arXiv:hep-ex/0506062]. (document), 2.1, 2.3, 2.3, 2.4, 4.6.3, 4.7.3, 4.28, 5.1, 5.2, 5.2, 5.2

[29] E. Braaten and J. Lee, Phys. Rev. D **67** (2003) 054007 [Erratum-ibid. D **72** (2005) 099901] [arXiv:hep-ph/0211085]. 2.1, 2.2, 1, 2.3, 2.3, 5.2

[30] J. P. Ma and Z. G. Si, Phys. Rev. D **70** (2004) 074007 [arXiv:hep-ph/0405111]. 2.1, 2.2.4

[31] V. V. Braguta, arXiv:0811.2640 [hep-ph]. 2.1, 2.2.4

[32] Y. J. Zhang, Y. j. Gao and K. T. Chao, Phys. Rev. Lett. **96** (2006) 092001 [arXiv:hep-ph/0506076]. 2.1, 3

[33] D. Ebert and A. P. Martynenko, Phys. Rev. D **74** (2006) 054008 [arXiv:hep-ph/0605230]. 2.1, 2.2.3, 2, 2.3, 2.3, 5.2

[34] D. Ebert, R. N. Faustov, V. O. Galkin and A. P. Martynenko, Phys. Rev. D **70** (2004) 014018 [Erratum-ibid. D **77** (2008) 079903] [arXiv:hep-ph/0404280]. 2.1

[35] A. P. Martynenko, Phys. Rev. D **72** (2005) 074022 [arXiv:hep-ph/0506324]. 2.1

[36] R. Ammar *et al.* [CLEO Collaboration], Phys. Rev. D **57** (1998) 1350 [arXiv:hep-ex/9707018]. 2.2

[37] G. T. Bodwin, J. Lee and E. Braaten, Phys. Rev. Lett. **90** (2003) 162001 [arXiv:hep-ph/0212181].
2.2, 2.5, 2.5

[38] G. T. Bodwin, J. Lee and E. Braaten, Phys. Rev. D **67** (2003) 054023 [Erratum-ibid. D **72** (2005) 099904] [arXiv:hep-ph/0212352]. 2.2, 2.5

[39] M. Gremm and A. Kapustin, Phys. Lett. B **407** (1997) 323 [arXiv:hep-ph/9701353]. 2.2.2

[40] V. V. Braguta, A. K. Likhoded and A. V. Luchinsky, Phys. Rev. D **72** (2005) 074019 [arXiv:hep-ph/0507275]. 2.2.4, 2.3, 2.3, 5.2

[41] G. P. Lepage and S. J. Brodsky, Phys. Rev. Lett. **43** (1979) 545 [Erratum-ibid. **43** (1979) 1625],
G. P. Lepage and S. J. Brodsky, Phys. Rev. D **22** (1980) 2157. 2.2.4

[42] Z. G. He, Y. Fan and K. T. Chao, Phys. Rev. D **75** (2007) 074011 [arXiv:hep-ph/0702239]. 2.2.4

[43] G. T. Bodwin, J. Lee and C. Yu, Phys. Rev. D **77** (2008) 094018 [arXiv:0710.0995 [hep-ph]]. 2.2.4

[44] E. S. Swanson, Phys. Rept. **429** (2006) 243 [arXiv:hep-ph/0601110]. 2.4.1

[45] *BABAR* Collaboration, B. Aubert *et al.* ,, Phys. Rev. D **69**, 071101 (2004); 3

[46] P. F. . Harrison and H. R. . Quinn [BABAR Collaboration], "The BaBar physics book: Physics at an asymmetric B factory," 3

[47] PEP-II Conceptual Design Report, SLAC-R-418 (1993). 3.1

[48] *BABAR* Collaboration, B. Aubert *et al.* , Nucl. Instrum. Methods Phys. Res., Sect. A**479**, 117 (2002).

[49] W. Kozanecki *et al.*, "Trickle-charge: A new operational mode for PEP-II," 3.1

[50] I. Adam *et al.* [BABAR-DIRC Collaboration], Nucl. Instrum. Meth. A **538** (2005) 281. 3.4

[51] D. Boutigny *et al.* [BABAR Collaboration], "BaBar technical design report", chapter 7 3.5

[52] M. Wilson , "The VtxCascade decay fitter", http://www.slac.stanford.edu/BFROOT/www/Physics/Tools/Vertex/cascade/VtxCas 4.2.2

[53] A. Hocker *et al.*, "TMVA: Toolkit for multivariate data analysis," [arXiv:physics/0703039]. 4.6.2, 4.6.2

[54] G. C. Fox and S. Wolfram, "Event Shapes In e^+e^- Annihilation," Nucl. Phys. B **149** (1979) 413 [Erratum-ibid. B **157** (1979) 543]. 4.6.2